

A HIGH-ORDER LOW-ORDER ALGORITHM WITH
EXPONENTIALLY-CONVERGENT MONTE CARLO FOR THERMAL
RADIATIVE TRANSFER PROBLEMS

A Dissertation

by

SIMON RAY BOLDING

Submitted to the Office of Graduate and Professional Studies of
Texas A&M University
in partial fulfillment of the requirements for the degree of

DOCTOR OF PHILOSOPHY

Chair of Committee,	Jim Morel
Committee Members,	Ryan McClarren
	Jean Ragusa
	Jean-Luc Guermond
Head of Department,	Yassin Hassan

May 2017

Major Subject: Nuclear Engineering

Copyright 2017 Simon Ray Bolding

ABSTRACT

We have implemented a new high-order low-order (HOLON) algorithm for solving thermal radiative transfer (TRT) problems. Within each discrete time step, fixed-point iterations are performed between a high-order (HO) exponentially-convergent Monte Carlo (ECMC) solver and a low-order (LO) system of equations. The LO system is based on spatial and angular moments of the transport equation and a linear-discontinuous finite-element (LDFE) spatial representation, producing equations similar to the standard S_2 equations. The LO solver is fully implicit in time and efficiently converges the non-linear temperature dependence with Newton's method. The HO solver provides a globally accurate solution for the angular intensity to a fixed-source, pure absorber transport problem. This global solution is used to compute consistency terms in the LO equations that require the HO and LO solutions to converge towards the same solution. The use of ECMC allows for the efficient reduction of statistical noise in the solution.

We investigated several extensions of this algorithm. A parametric closure of the LO system was used for the spatial variable, based on local relations computed with the HO solver. The spatial closure improves consistency between the two solvers compared to a standard LDFE spatial discretization of the LO system. The ECMC algorithm has been extended to integrate the angular intensity in time, with a consistent time closure of the LO radiation equations. The time closure increases accuracy in optically-thin problems compared to a backward Euler discretization. Finally, we have applied standard source iteration and Krylov procedures to iteratively solve the LO equations, with linear diffusion synthetic acceleration.

Herein, we present results for one-dimensional, gray test problems. Results

demonstrate several desirable properties of this algorithm: the HOLO method preserves the equilibrium diffusion limit, prevents violation of the maximum principle, and can provide high-fidelity MC solutions to the TRT equations with minimal statistical noise. We have compared results with an implicit Monte Carlo (IMC) code and compared the efficiency of ECMC to standard Monte Carlo in this HOLO algorithm. Our HOLO algorithm is more accurate and more efficient than standard IMC. The extent to which this is so is problem-dependent.

“To live is to suffer, to survive is to find some meaning in the suffering.”

–Friedrich Nietzsche

ACKNOWLEDGEMENTS

Starting with the obvious, I would like to express my gratitude to Dr. Jim Morel for your guidance and willingness to impart your transport wisdom on me over the last few years. In addition to being a prime source of knowledge, as an advisor you seem to find the appropriate balance between blind patience and hard-nosed motivation, where the focus is always exclusively on the problem under investigation. I would also like to thank Dr. McClarren and Dr. Ragusa for always willingly providing alternative view points and discussion on interesting topics, often unrelated to work and occasionally involving fine beverages. Overall, it has been a pleasure being part of this research group.

I would like to thank my parents for a great childhood and continued support, as well as for never pressuring me to get a real job or take over the farm...yet. And of course my friends at A&M deserve credit for the constant antics and shenanigans that help take the edge off of grad school. I must also acknowledge my friend Hank; I cannot imagine my life would have went down this academic path if we hadn't met. And finally, I would like to thank my (now) wife Madeline. I think it goes without much explanation, but you have always been easy-going through this process and made life pleasant.

CONTRIBUTORS AND FUNDING SOURCES

Contributors

This work was supported by a dissertation committee consisting of Professor Jim Morel, Ryan McClarren, and Jean Ragusa of the Nuclear Engineering Department and Jean-Luc Guermond of the Department of Mathematics.

Application of this algorithm to radiative transfer problems began under the guidance of Mathew Cleveland and Robert Lowrie while at Los Alamos National Laboratory. All other work conducted for the dissertation was completed by the student with guidance from his advisor Jim Morel.

Funding Sources

This graduate work was completed with financial and educational support from multiple sources. This research was supported with funding received from the DOE Office of Nuclear Energy's Nuclear Energy University Programs, the DOE National Nuclear Security Administration, under Award Number(s) DE-NA0002376, a scholarship from the American Nuclear Society, a scholarship from Texas A&M University, and under Los Alamos National Security, LLC, for the National Nuclear Security Administration of the U.S. Department of Energy under contract DE-AC52-06NA25396.

TABLE OF CONTENTS

	Page
ABSTRACT	ii
ACKNOWLEDGEMENTS	v
NOMENCLATURE	vi
TABLE OF CONTENTS	vii
LIST OF FIGURES	xi
LIST OF TABLES	xiii
1. INTRODUCTION	1
1.1 Dissertation Layout	3
1.2 Thermal Radiative Transfer Background	4
1.2.1 The Equations of Thermal Radiative Transfer	5
1.2.2 Derivation of 1D Grey Model	7
1.2.3 The Equilibrium Diffusion Limit	8
1.3 Previous Work	9
1.3.1 The Implicit Monte Carlo Method	10
1.3.2 Moment-Based Acceleration Methods	12
1.3.3 Residual Monte Carlo Methods	13
2. OVERVIEW OF THE HOLO ALGORITHM	15
3. THE MOMENT-BASED LOW-ORDER EQUATIONS	20
3.1 Forming the Space-Angle Moment Equations	20
3.1.1 LO Spatial Mesh and Finite-Element Spatial Moments	20
3.1.2 Definition of Angular Moments	23
3.1.3 Space-Angle Moments of the Radiation Transport Equation	23
3.1.4 The Angular Consistency Terms	24
3.1.5 The Exact Radiation Moment Equations	26
3.1.6 Material Energy Equations	27
3.2 Closing the LO Equations in Space and Angle	28
3.2.1 Angular Closure	28

3.2.2	LDFE Spatial Closure	29
3.2.3	Boundary Conditions	31
3.3	Newton's Method for LO Equations	31
3.4	Accuracy of LO Equations in the Equilibrium Diffusion Limit	33
3.5	Fixups for Negative Solutions with LDFE Closure	33
3.5.1	Balance Preserving Fixup	35
3.6	Spatial Closure Based on the HO Solution	36
3.6.1	Motivation	36
3.6.2	Choice of Spatial Closure	38
3.6.3	The Linear Doubly-Discontinuous Trial Space	39
3.6.4	Fixup for the Linear Doubly-Discontinuous Trial Space	41
4.	THE EXPONENTIALLY-CONVERGENT MONTE CARLO HIGH-ORDER SOLVER	43
4.1	Implementation of LDFE x - μ Trial Space	43
4.2	The ECMC Algorithm	45
4.2.1	Projection and Statistical Accuracy of ECMC	47
4.2.2	Adaptive Mesh Refinement	50
4.2.3	Negative Values for the Radiation Intensity	51
4.3	Systematic Sampling Algorithm for Residual Source	52
4.4	Continuous Weight Deposition Tallies	54
4.4.1	Face Tallies and Correction Near $\mu = 0$	56
4.5	ECMC Solution with Linear Doubly-Discontinuous FE Trial Space . .	57
5.	COMPUTATIONAL RESULTS	61
5.1	Metrics of Accuracy and Statistical Efficiency	61
5.2	Marshak Wave	64
5.3	Two Material Problem	67
5.4	Performance Comparison of IMC and HOLO-ECMC	70
5.5	Comparison of Different HO Solvers	72
5.6	Pre-heated Marshak Wave Problem and Adaptive Mesh Refinement .	73
5.7	Accuracy in the Equilibrium Diffusion Limit	74
5.8	Accuracy of HO Spatial Closure	76
5.8.1	Smooth Problem	77
5.8.2	Two Material Problem	81
5.9	Preservation of the Discrete Maximum Principle	82
6.	ACCELERATED ITERATIVE SOLUTION TO THE LO EQUATIONS .	87
6.1	Source Iteration Solution to the Linearized LO Equations	88
6.2	Linear Diffusion Synthetic Acceleration	89
6.2.1	The WLA-DSA Accelerated Source Iteration Algorithm	92

6.3	GMRES Solution to the LO Equations	93
6.4	Computational Results	95
7.	RESOLVING ISSUES WITH NEGATIVE INTENSITIES FOR ECMC . .	98
7.1	Calculating a Positive LDFE Representation	99
7.2	Artificial Source Method for Negativities in the HO Intensity	100
7.3	Computational Results	102
7.3.1	Analytic Fixed Source Problem	102
7.3.2	Radiative Transfer Problems	104
8.	RESIDUAL MONTE CARLO TREATMENT OF THE TIME VARIABLE	110
8.1	Modifications to the HO Solver	110
8.1.1	Step Doubly-Discontinuous Trial Space in Time	111
8.1.2	Residual Source Definition and Sampling	113
8.1.3	Importance Sampling on Interior of Time Step	115
8.1.4	Tracking and Tallying in Time	116
8.2	Closing the LO Equations in Time	118
8.2.1	Derivation of Time-Averaged Moment Equations	119
8.2.2	Parametric Time Closure	120
8.3	Computational Results	122
8.3.1	Near-Void Problem	122
8.3.2	Optically Thin Problem	126
8.3.3	Marshak Wave Problem	131
9.	CONCLUSIONS AND FUTURE WORK	134
9.1	Conclusions	134
9.2	Future Work	137
	REFERENCES	140
	APPENDIX A DERIVATIONS AND RELATIONS FOR THE LO SYSTEM	146
A.1	Useful Moment Relations for LO Equations	146
A.2	Hybrid Picard-Newton Method for the LO Equations	148
A.2.1	Damped Newton Iterations	151
	APPENDIX B DERIVATIONS FOR HIGH-ORDER SOLVER	153
B.1	Analytic Error Contribution for LDD Trial Space	153
B.2	Analytic Answer for Fixed Source Problem	154
	APPENDIX C DERIVATION OF THE WLA-DSA EQUATIONS	157

C.1	Forming a Continuous Diffusion Equation	157
C.1.1	Diffusion Boundary Conditions	159
C.2	Mapping Solution onto LD Unknowns	159

LIST OF FIGURES

FIGURE		Page
3.1	Illustration of linear finite element basis functions $b_{L,i}(x)$ and $b_{R,i}(x)$, for spatial element i	21
3.2	Linear-discontinuous trial space for half-range mean intensity and $\mu > 0$, in LO equations.	30
3.3	Linear doubly-discontinuous representation for mean intensity in LO equations.	40
5.1	Comparison of radiation temperatures for Marshak wave problem at $t = 5$ sh.	65
5.2	Comparison of radiation temperatures for two material problem. . .	69
5.3	Comparison of radiation temperatures for the pre-heated Marshak wave problem for 100 x cells at $t = 0.5$ sh.	75
5.4	Comparison of T_r for a problem in the equilibrium diffusion limit, with step and LDFE discretizations of the LO equations.	76
5.5	Comparison of solutions for smooth problem with different spatial closures.	79
5.6	Inaccuracies for HO spatial closure applied to solution of the two material problem.	82
5.7	T_r and T_m for maximum principle violation problem with IMC and $\Delta t = 0.001$ sh.	84
5.8	T_m for maximum principle violation problem with IMC for various time step sizes. The IMC solution does not preserve the discrete maximum principle.	84
5.9	T_m for maximum principle violation problem with HOLO method for various time step sizes. The HOLO solution preserves the discrete maximum principle.	85

7.1	LDFE projection of angular intensity $\tilde{I}(x, \mu)$ for the fixed-source problem.	105
7.2	Comparison of cell-averaged radiation temperatures for two material problem and various fixup methods.	108
7.3	Comparison of cell-averaged radiation temperatures for Marshak wave problem and various fixup methods.	109
8.1	Step doubly-discontinuous representation of t for the HO solution. . .	112
8.2	Comparison of radiation energy densities of IMC and HOLO method for the HO time closure and a BE discretization.	123
8.3	Comparison of radiation temperatures of IMC and the HOLO method for different time step sizes and numbers of batches, for the near-void problem.	125
8.4	Comparison of radiation energy densities for the HOLO method with different numbers of μ cells, for the near-void problem; $\Delta t = 0.001$ sh.	126
8.5	Comparison of radiation temperatures of IMC and the HOLO method for different time step sizes and numbers of batches, for optically thin problem.	127
8.6	Comparison of T_r^{n+1} for 30,000 histories per time step. The HOLO-TC result has insufficient histories to accurately estimate end of time step unknowns.	129
8.7	Comparison of HOLO-TC, HOLO-BE, and IMC methods for the Marshak Wave problem, with 10^6 histories per time step.	131

LIST OF TABLES

TABLE		Page
5.1	Comparison of sample statistics for the Marshak Wave problem. Simulation end time is $t = 5$ sh.	67
5.2	Material properties for two material problem.	67
5.3	Comparison of sample statistics for the two material problem for 200 x cells. Simulation end time is $t = 2$ sh.	70
5.4	Comparison of average CPU times per history and LO iteration counts for the Marshak Wave problem.	71
5.5	Average CPU times per history and LO iteration counts required for the two material problem.	71
5.6	Comparison of sample statistics for the Marshak Wave problem. Number of ECMC batches is indicated in parenthesis.	72
5.7	Comparison of sample standard deviations for the two material problem. Number of ECMC batches is indicated in parenthesis.	73
5.8	Comparison of sample statistics for the pre-heated marshak wave problem for 100 x cells. Number of ECMC batches is indicated in parenthesis.	74
5.9	Comparison of error metrics, reported as percentages, averaged over 20 simulations of smooth problem. The absolute standard deviation for each value is reported in parenthesis. Reference solution uses 500 cells.	80
5.10	Comparison of LO Newton iterations for HOLO solution to MP problem and different time step sizes. For $\Delta t = 10^{-5}$ sh, no damping was used; for all other cases a damping factor of 0.5 was used.	86
6.1	Scattering source iterations for the two material problem. Simulation end time is 1 sh.	97
6.2	Scattering source iterations for the modified, diffusive two material problem. Simulation end time is 2 sh.	97

6.3	Scattering source iterations for the equilibrium diffusion limit problem. Simulation end time is 3 sh.	97
7.1	Comparison of accuracy in cell-averaged $\phi(x)$ value for fixed source problem and various number of histories per batch.	104
7.2	Comparison of sample statistics for different HO fixup methods applied to the two material problem. Simulation end time is $t = 2$ sh. .	106
7.3	Comparison of sample statistics for different HO fixup methods and the Marshak wave problem. Simulation end time is $t = 5$ sh.	107
8.1	Comparison of accuracy and FOM for the end of time step radiation energy densities, of the last time step, for the optically thin problem and $\Delta t = 5 \times 10^{-4}$ sh. Simulation end time is $t = 0.003$ sh.	130
8.2	Comparison of accuracy and FOM for the end of time step radiation energy densities, of the last time step, for the optically thin problem and $\Delta t = 1 \times 10^{-4}$ sh. The reference results are all for 100 x cells. Simulation end time is $t = 0.003$ sh.	130
8.3	Comparison of sample statistics for the end of time step radiation energy densities, of the last time step, for the Marshak wave problem and maximum time step of 0.01 sh. Simulation end time is $t = 3.0$ sh.	132
8.4	Comparison of sample statistics using importance sampling on the interior of the time step, for the Marshak Wave problem. Simulation end time is $t = 1.0$ sh and max Δt is 0.01 sh.	133

1. INTRODUCTION

Accurate transient solutions to the thermal radiative transfer (TRT) equations are important for simulations in the high-energy, high-density physics regime, e.g., for inertial confinement fusion and astrophysics. Moment-based hybrid Monte Carlo (MC) methods have demonstrated great potential for accelerated solutions to TRT problems [1, 2, 3]. These nonlinear acceleration methods perform fixed-point iterations between a high-order (HO) transport equation and a low-order (LO) system. The LO system is obtained from the HO system by means of spatial and angular moments. The HO system provides closure terms to the LO system that make the LO system exactly reproduce the HO moments, upon nonlinear convergence. The LO system provides low-order source terms to the HO system that are expensive to iteratively converge, e.g., the photon emission and isotropic scattering sources. The two systems are synergistic in that the LO system with fixed closure terms can be fully solved much more efficiently than the HO system, and the HO system can accurately compute angular closure terms given fixed low-order source terms.

We have developed a new high-order low-order (HOLO) algorithm for solving TRT problems. This algorithm has several desirable properties, some of which improve on current computational methods: the HOLO method preserves the equilibrium diffusion limit, prevents violation of the maximum principle, and can provide high-fidelity MC solution to the TRT equations in an efficient manner. In particular, our HOLO method utilizes an exponentially-convergent Monte Carlo (ECMC) algorithm to solve the associated radiation transport equation. The ECMC method significantly decreases the statistical noise associated with MC transport calculations for TRT problems. In conjunction with the ECMC algorithm, we use a nonlinear

low-order (LO) system that is fully implicit in time and is solved with Newton's method. The lower-dimensional equations are derived directly from the TRT equations, formed such that the LO system can preserve the accuracy of the ECMC treatment of particle transport. The LO equations are formed with linear finite-element (FE) based spatial moments and angular moments over each half-range. A linear-discontinuous (LD) representation is used to discretize the temperature field. Two different spatial closures of the LO equations have been investigated: the standard LD FEM closure and a new parametric closure that is fully consistent with the HO equations. Our LO system and approach to enforcing consistency contrast from the formulations used in other moment-based acceleration methods, e.g., those in [1, 4, 5].

We have also investigated several extensions and improvements of this method. First, alternative, iterative solution methods to the LO equations were implemented, using typical source iteration methods with linear diffusion synthetic acceleration. The primary goal is to present a solution method for the LO equations that is more extendible to higher dimensions. Additionally, we have investigated methods to resolve issues when the optically thick mesh cells produce intensity gradients that are too difficult to resolve with the LDFE mesh representation. In the HO equations, we can add artificial sources that make the solution more easily representable by the chosen mesh resolution, without altering the zeroth moment of the transport equation, neglecting statistical noise. This approach was found to provide minimal improvement in some problems. Finally, higher accuracy treatment of the time variable in the transport equation was investigated. The ECMC algorithm was modified to include integration of the time variable; this includes the introduction of a step, doubly-discontinuous (SDD) trial space representation in time. A new parametric closure of the LO equations was derived to capture the time accuracy of the ECMC

simulations in the LO equations, with the same computational cost to solve as Backward Euler (BE) time-discretized LO equations. The main interest is in increasing accuracy in resolution of radiation wavefronts in optically thin regions, where a BE time discretization propagates radiation energy through space artificially fast.

The HOLO algorithm has been developed and implemented for a simplified model with one spatial dimension and frequency-integrated equations. Although not discussed here, the HOLO method approach developed in this work was also applied to 1D neutronics problems in [6]. Throughout this work, we compare our method to the implicit Monte Carlo (IMC) method [7], which is the standard MC transport solution method to the TRT equations. Results are given for several test problems to demonstrate the benefits of the HOLO method. We have also demonstrated the efficiency of ECMC over standard Monte Carlo as a HO solver in the HOLO algorithm.

1.1 Dissertation Layout

In the remainder of Chapter 1, a brief description of thermal radiative transfer and the simplified model used for this work are given, followed by a discussion of the standard Monte Carlo solution method and other related research. In Chapter 2, an overview of the outer HOLO algorithm and a description of how the HO and LO systems interact is given. Chapter 3 gives a detailed derivation of the LO moment equations, the closure of the system, and how they are solved. Chapter 4 details the ECMC algorithm and how it is applied to solve the HO transport problem. Then, Chapter 5 provides computational results to demonstrate desirable qualities of this method, with comparisons to IMC. Some of the results from Chapter 5 were previously published in [2].

The remaining chapters provide details on extensions made to the standard algorithm. Chapter 6 details a source iteration and Krylov solution method for the LO

equations, with a linear diffusion synthetic acceleration method. In Chapter 7 we investigate a potential approach for resolving issues with difficult to resolve solutions in the ECMC algorithm. For the majority of this work time-discretized equations are assumed, but in Chapter 8 a MC-based time treatment of radiation transport is investigated. Finally, Chapter 9 provides a summary, discussion, and potential future work for the method.

1.2 Thermal Radiative Transfer Background

Thermal radiative transfer (TRT) physics describe the time-dependent coupling between a photon radiation field and a high-temperature material, which is typically a plasma. The desired transient unknowns are the spatial energy-density distributions of the radiation and material. As photons transport through the medium, they interact through scattering and absorption by the material, depositing momentum and energy. The material is heated through absorption of photons and is cooled by emission of thermal x-ray photons into the radiation field. The emission process is a strongly nonlinear function of temperature [8]. Additionally, the material properties are typically a function of temperature, in particular the absorption cross section. The temperature-dependent material properties and absorption and re-emission physics lead to systems that require accurate modeling of photon transport through a mix of streaming and optically-thick, diffusive regions.

Accurate modeling of TRT physics becomes relevant in the high-energy, high-density physics regime. Radiative transfer is a dominant form of heat transfer in high-temperature systems, where the material temperature is $O(10^6)$ K or higher. Typical computational applications of TRT include simulation of inertial confinement fusion and astrophysics phenomena. In most applications where TRT is important, the fluid material is typically in motion and exchanges momentum with the radiation

field. In this work, we neglect motion of the material, which would require inclusion of hydrodynamics in our model [8]. However, our LO equations are well-suited for coupling to material motion via typical operator-splitting methods for radiation-hydrodynamic systems [9, 10].

1.2.1 The Equations of Thermal Radiative Transfer

First, the photon radiation field, with the appropriate units used throughout this work, is characterized. Photons transporting through a material are described by the particle position vector \mathbf{r} (cm), direction vector $\boldsymbol{\Omega}$ (str, i.e., steradians), time t (sh, where $1 \text{ sh} \equiv 10^{-8} \text{ s}$), and frequency ν (Hz). The primary radiation unknown is the angular intensity $I(\mathbf{r}, \boldsymbol{\Omega}, \nu, t)$ (jk cm $^{-2}$ s $^{-1}$ Hz $^{-1}$ str $^{-1}$), which represents a distribution function of energy contained in the radiation field, per unit of phase space. We use the energy unit jerks (jk), where $1 \text{ jk} = 10^9 \text{ joules}$. The intensity can be related to the volumetric density of photons $N(\mathbf{r}, \boldsymbol{\Omega}, \nu, t)$ (photons cm $^{-3}$ Hz $^{-1}$ str $^{-1}$) via the relation

$$I(\mathbf{r}, \boldsymbol{\Omega}, \nu, t) = ch\nu N(\mathbf{r}, \boldsymbol{\Omega}, \nu, t), \quad (1.1)$$

where $c = 299.792458 \text{ cm sh}^{-1}$ is the speed of light and $h = 4.13567 \times 10^{-18} \text{ keV Hz}^{-1}$ is Planck's constant. The angular intensity is a useful quantity because it is directly related to reaction rates.

The governing conservation equation for the radiation field is a transport equation given by [8, 11, 12]

$$\frac{1}{c} \frac{\partial I(\mathbf{r}, \boldsymbol{\Omega}, \nu, t)}{\partial t} + \boldsymbol{\Omega} \cdot \nabla I(\mathbf{r}, \boldsymbol{\Omega}, \nu, t) + \sigma_t(\mathbf{r}, \nu) I(\mathbf{r}, \boldsymbol{\Omega}, \nu, t) = \int_0^\infty \int_{4\pi} \sigma_s(\boldsymbol{\Omega}' \rightarrow \boldsymbol{\Omega}, \nu' \rightarrow \nu) \phi(\mathbf{r}', \nu', t) d\boldsymbol{\Omega}' d\nu' + \sigma_a(\mathbf{r}, \nu) B_\nu(\mathbf{r}, \nu, T), \quad (1.2)$$

where

$$B_\nu(\mathbf{r}, \nu, T) = \frac{2h\nu^3}{c^2} \frac{1}{e^{h\nu/T} - 1} \quad (1.3)$$

is the black-body Planckian emission spectrum at temperature T (keV) [8], and the macroscopic scattering, absorption, and total cross sections are σ_s , σ_a , and σ_t , respectively. The scattering source includes integration over all possible incoming angles $\boldsymbol{\Omega}'$ in differential solid angle $d\Omega'$. The absorption cross section σ_a is typically a strong function of temperature, i.e., $\sigma_a \equiv \sigma_a(T)$. Following standard notation, we report temperatures in units of keV as an effective energy, obtained by multiplying by the Boltzmann constant k_B [8]. Thus, all material temperatures are $T \equiv T_K k_B$, where k_B is the Boltzmann constant (keV K⁻¹) and T_K is the temperature in kelvin.

The material is characterized by the material internal energy as a function of position. The internal energy E is related to the material temperature T through an equation of state. In this work, a perfect gas equation of state is assumed [13], which produces the relation $\rho c_v T = E$, where ρ is the material mass density and c_v is the specific heat. Thus, we will use $T(\mathbf{r}, t)$ as the primary unknown to describe the material energy distribution. The material energy conservation equation is

$$\rho(\mathbf{r})c_v(\mathbf{r})\frac{\partial T(\mathbf{r}, t)}{\partial t} = \int_0^\infty \left(\int_{4\pi} \sigma_a I(\mathbf{r}, \boldsymbol{\Omega}, \nu, t) d\Omega - \sigma_a 4\pi B_\nu(\mathbf{r}, \nu, T) \right) d\nu \quad (1.4)$$

In derivation of the above equations, the conditions of local thermodynamic equilibrium were assumed, i.e., the emission source is described point-wise by the Planck function at the temperature at that position, and the material is well-described by the local temperature [8, 12]. The emission source is a non-linear function of temperature and is proportional to T^4 after integration over frequency.

1.2.2 Derivation of 1D Grey Model

At this point, we introduce the simplified equations that will be used in the remainder of this work. First, the solutions are assumed to only vary in one spatial dimension using Cartesian coordinates, referred to as the 1D slab geometry [11]. The position is described by a single coordinate x and the direction of particle travel is described by μ , which is the cosine of the angle between the particle direction and the positive x axis. The angular intensity is assumed symmetric in angle azimuthally about the x axis. To simplify the equations, the equations are integrated over all frequencies. We also assume that the material properties are independent of photon frequency, or equivalently we know the weighting spectrum of the frequency integrated cross sections. Finally, we assume physical scattering is isotropic in angle. With these assumptions, integration over the azimuthal angle and all frequencies, with algebraic manipulation, ultimately yields the 1D grey equations [12, 8]

$$\frac{1}{c} \frac{\partial I(x, \mu, t)}{\partial t} + \mu \frac{\partial I(x, \mu, t)}{\partial x} + \sigma_t I(x, \mu, t) = \frac{\sigma_s}{2} \phi(x, t) + \frac{1}{2} \sigma_a a c T^4(x, t) \quad (1.5)$$

$$\rho c_v \frac{\partial T(x, t)}{\partial t} = \sigma_a \phi(x, t) - \sigma_a a c T^4(x, t). \quad (1.6)$$

The equations have associated incident boundary conditions for the angular intensity:

$$I(0, \mu) = I^{inc,+}(\mu), \quad \mu > 0 \quad (1.7)$$

$$I(X, \mu) = I^{inc,-}(\mu), \quad \mu < 0, \quad (1.8)$$

for a spatial domain spanning $0 \leq x \leq X$. In the above equations the fundamental unknowns are the material temperature $T(x, t)$ and the grey angular intensity $I(x, \mu, t) = \int_0^\infty I(x, \mu, \nu, t) d\nu$. The mean radiation intensity $\phi(x, t) = \int_{-1}^1 I(x, \mu, t) d\mu$ is related to the radiation energy density E_r (jk cm⁻³ sh⁻¹) by the relation $E_r = \phi/c$.

The integral of $B_\nu(\mathbf{r}, \nu, T)$ over all frequencies and angles produced the grey Planckian emission source $\sigma_a acT^4$ [8] in Eq. (1.6), where $a = 0.01372 \text{ jk cm}^{-3} \text{ keV}^4$ is the radiation constant, which is proportional to the Stefan-Boltzmann constant. The term $\sigma_a \phi$ is the rate of energy absorption by the material, whereas the emission term represents losses to the material internal energy. We have developed our algorithm to produce efficient solutions to Eq. (1.5) and (1.6).

1.2.3 The Equilibrium Diffusion Limit

A critical aspect for any numerical solution to the thermal radiative transfer equations is preservation of the asymptotic, equilibrium-diffusion limit (EDL) [14, 15]. In the EDL, the material becomes optically thick and increasingly diffusive, as σ_a becomes large and ρc_v becomes small. The solution approaches equilibrium with $I(x, \mu) = \frac{1}{2} acT^4(x)$, where the distribution of the solution is well described by the material temperature [15]. The spatial scale length for diffusive solutions, the diffusion length, can be equal to an arbitrary number of mean-free-paths (MFPs), but transport discretization schemes are only guaranteed to converge in the limit as the number of MFPs per cells becomes small [14]. To achieve convergence with a small number of diffusion lengths per cell in diffusive problems, the transport discretization must preserve the EDL.

Discretization schemes of the transport equation that preserve the EDL correctly limit to the appropriate discretized diffusion equation in diffusive problems. Spatial discretizations that do not preserve the EDL can produce inaccurate solutions, even though the mesh size accurately resolves the diffusion length scale, with inaccuracies that are much greater than expected from truncation error. Such non-preserving methods require spatial mesh resolution on the order of a MFP [14]. The EDL regime is typical in applications of TRT, so discretizations must preserve this limit

to produce accurate solutions with reasonable mesh resolutions.

1.3 Previous Work

This section describes related work on Monte Carlo solution to the TRT equations, as well as some additional important properties that numerical solution to TRT equations must preserve. The Monte Carlo (MC) method [16] is a standard computational method in the field of radiation transport. It has been used to great success, providing high-accuracy solutions to particle transport problems described by the linear Boltzmann transport equation for many decades. The application of MC to the linear Boltzmann equation is well documented in literature [17, 16, 11]. The Monte Carlo method samples the underlying physics distributions to estimate the average behavior of a field of particles. This can provide highly-accurate results, in particular for treatment of the angular variable associated with particle transport problems. Detailed descriptions of MC simulation of particle tracking, sampling of interactions, etc. can be found in literature [17, 18, 16].

With respect to TRT problems, the temperature equation is almost always solved deterministically to produce a linear particle transport equation. Monte Carlo solution to this transport equation can introduce large statistical noise into the material temperature distribution, which is undesirable when coupling to other physics, e.g., in radiation hydrodynamics. To improve the efficiency of MC solutions, hybrid MC methods utilize a deterministic solution to accelerate the MC solution.

In the remainder of this section, we detail the standard method for MC solution to TRT equations, the implicit Monte Carlo (IMC) method, and then discuss related moment-based acceleration and other alternative hybrid solution methods. We also discuss the residual Monte Carlo (RMC) method, which is similar to the HO solver in our method.

1.3.1 *The Implicit Monte Carlo Method*

The IMC method [7, 18] is the standard approach for applying the MC method to TRT problems. The IMC method partially linearizes Eq. (1.5) & Eq. (1.6) over a discrete time step, with material properties evaluated at the previous-time-step temperature. Linearization of the system produces a linear transport equation that can be solved with MC simulation. The transport equation contains an approximate emission source and an effective scattering cross section representing absorption and reemission of photons over a time step. The transport equation is solved with MC simulation to advance the distribution of radiation to the end of the time step and determine the energy absorbed by the material over the time step. The energy absorption by the material is tallied over a discrete spatial mesh, computed with cell-averaged quantities. Integration of the time-variable is treated continuously for radiation variables over the time step via MC sampling, but the linearized Planckian source in the transport equation is based on a time-discrete approximation.

The IMC method has some notable limitations. In optically thick regions, or for large time steps, the effective scattering dominates interactions. In these diffusive regions IMC becomes computationally expensive. Acceleration methods typically attempt to improve efficiency by allowing particles to take discrete steps through optically-thick regions based on a spatially-discretized diffusion approximation [19, 20]. In IMC, temperature-dependent material properties, in particular cross sections, are evaluated at the previous-time step temperature. These lagged cross sections can produce inaccurate solutions but do not cause stability issues.

An important aspect for numerical simulation of TRT equations is preservation of the discrete maximum principle (MP). The MP states that the material temperature and mean intensity in the interior of the domain should be bounded by the solution

at the boundaries of the domain, in the absence of interior energy sources [21, 22]. The analytic solution to the TRT equations satisfies the MP [22], so we desire numerical approximations that preserve the MP in a discrete sense, for each time step. The BE time discretization of the TRT equations has been shown to preserve the MP [22]. For some problems, the IMC method can yield non-physical results that violate the MP if the time step size is too large or the cell size is too small [21]. The violation of the maximum principle results in the material temperature being artificially higher than the effective radiation temperature. The violation by IMC is caused by the approximate linearization of the end-of-time-step emission source; the emission source is not truly implicit in time. The linearized estimate of the emission source typically can not be iteratively improved due to the high computational cost of the MC transport. The work in [23] uses less-expensive MC iterations to produce an implicit system which prevents this from happening, but the method as currently formulated has slow iterative convergence in diffusive problems.

In IMC the material and radiation energy fields are discretized spatially to solve for cell-averaged values. Inaccurate spatial representation of the emission source over a cell can result in energy propagating through the domain artificially fast, yielding non-physical results that are often referred to as “teleportation error” [24]. The IMC method uses a fixup known as source tilting to mitigate this problem. Source tilting reconstructs a more accurate linear-discontinuous representation of the emission source within a cell based on the cell-averaged material temperatures in adjacent cells. This linear reconstruction is also necessary to preserve the asymptotic equilibrium diffusion limit (EDL), at least for a more general time step size and class of problems than for a piece-wise constant representation [25]. Recent work in IMC has incorporated a linear-discontinuous finite-element representation directly into the discretization of the material temperature equation [26].

1.3.2 *Moment-Based Acceleration Methods*

An alternative application of MC to the TRT equations is moment-based hybrid MC methods. Recent work has focused on so-called high-order low-order (HOLO) methods [4, 5, 1, 6, 2]. These methods involve fixed-point iterations between high-order (HO) MC solution of a transport equation and a deterministic LO system. The low-order (LO) operator is based on angular moments of the transport equation, formulated over a fixed spatial mesh. Physics operators that are time consuming for MC to resolve, e.g., absorption-reemission physics, are moved to the LO system. The reduced angular dimensionality of the system and Newton methods allow for non-linearities in the LO equations to be fully resolved efficiently [4, 5]. The high-order (HO) transport problem is defined by Eq. (1.5), with sources estimated from the previous LO solution. The HO transport equation can be solved via MC to produce a high-fidelity solution for the angular intensity. The MC estimate of the angular intensity is used to estimate consistency terms, present in the LO equations, that require the LO system to preserve the angular accuracy of the MC solution. These consistency terms are present in all spatial-regions of the problem, requiring statistical variance to be reduced sufficiently throughout the entire domain of the problem. The LO equations are typically based on nonlinear Diffusion Acceleration (NDA) [4, 5].

The LO system used in our method is similar to the hybrid-S₂ method developed in [27], which was applied to continuous energy neutronics problems. Angularly, the method integrates over half-ranges to form nonlinear functionals, which in our work are referred to as consistency terms. The primary difference is in the treatment of the spatial discretization; because a linear reconstruction of the emission source is needed for accurate solution to TRT problems, we cannot perform the same manipulations

as in [27] where only cell-averaged unknowns are determined. Additionally, the diamond-difference spatial discretization used is not accurate for TRT problems in the equilibrium diffusion limit [15].

1.3.3 *Residual Monte Carlo Methods*

Another area of related research is the application of residual Monte Carlo to TRT problems. The goal of these methods is to use MC simulation to solve a auxiliary continuous transport equation for the error in some estimate of the intensity. The error is then added to the estimate of the solution, which can produce an overall solution for the intensity that has less statistical noise than solution of the original transport equation would produce. The work in [1] used residual MC as a HO solver for 1D grey TRT problems. In [1], the residual is formed with a fixed estimate of the solution, based on the previous time intensity, such that only sources on the faces of cells must be sampled. This reduces the dimension of the phase-space to be sampled [1]. The RMC algorithm demonstrated impressive reduction in statistical variance for slowly varying solutions. However, a piecewise constant representation is used for the space-angle representation of the intensity, which does not preserve the EDL and can be inaccurate in angularly complex regions of the problem. In this work, we apply the exponentially convergence MC (ECMC) algorithm that was previously applied to simplified steady state neutronics problems [28].

Similar to RMC, a difference formulation has been applied to another algorithm known as the symbolic IMC method (SIMC), for the case of 1D frequency-dependent problems [29]. SIMC forms a standard FE solution to the material energy balance equation, and uses symbolic weights in the MC transport to solve for expansion coefficients. The difference formulation modifies the transport equation to solve for unknowns representing the deviation of the intensity from equilibrium with the

material energy. The difference formulation was also applied to a linear-discontinuous FE spatial representation of the emission source, demonstrating accuracy in the EDL [30]. The algorithms in [29] and [1] produced minimal statistical noise in slowly varying problems where the behavior of the system is near equilibrium.

2. OVERVIEW OF THE HOLO ALGORITHM

The HOLO algorithm is a nonlinear acceleration method. Fixed-point iterations are performed between a high-order (HO) transport equation and a low-order (LO) system formulated with angular moments and spatial moments on a fixed spatial mesh. With the exception of Chapter 8, we will derive and discuss our HOLO method using a backward Euler (BE) time discretization for simplicity. We have also assumed constant specific heats and cell-wise constant cross sections, although our method could easily be extended to a general material equation of state. The BE time-discretized equations are

$$\mu \frac{\partial I^{n+1}}{\partial x} + \left(\sigma_t^{n+1} + \frac{1}{c\Delta t} \right) I^{n+1} = \frac{\sigma_s}{2} \phi^{n+1} + \frac{1}{2} (\sigma_a a c T^4)^{n+1} + \frac{I^n}{c\Delta t} \quad (2.1)$$

$$\rho c_v \frac{T^{n+1} - T^n}{\Delta t} = \sigma_a^{n+1} \phi^{n+1} - \sigma_a a c (T^4)^{n+1}, \quad (2.2)$$

where Δt is the time step size, and the superscript n is used to indicate the n -th time step. Cross sections are evaluated implicitly, i.e., at the end of time step temperature ($\sigma_a^{n+1} \equiv \sigma_a(T^{n+1})$). It is noted that in IMC the time derivative in Eq. (1.5) is typically treated continuously using time-dependent MC over each time step, but with the temperature implicitly discretized. Our HO transport equation is discrete in time for simpler application of ECMC and to avoid difficulties in coupling to the fully-discrete LO solver. In chapter 8, time-dependent transport is included in the ECMC algorithm with consistent LO equations, similar to the IMC treatment of the time variable, improving accuracy in optically thin regions.

In the HOLO context, the LO solver models isotropic scattering and resolves the material temperature spatial distribution $T(x)$ at each time step. The LO equations

are formed via half-range angular and spatial moments of Eq. (2.1) and Eq. (2.2). The spatial moments are formed over a finite-element mesh using linear finite-element (FE) basis functions. The angular treatment in the LO equations has the same form as those used in the hybrid-S₂ method in [27], with consistency parameters that represent angularly-weighted averages of the intensity. In this work, consistency refers to how accurately the LO moments reproduce moments of the HO solution. The angular consistency parameters are analogous to a variable Eddington factor [31]. If the consistency parameters are exact, then the LO equations are exact, neglecting spatial discretization errors. This provides the potential for the LO equations to correctly reproduce the associated space-angle moments of the HO solution. These consistency parameters are lagged in each LO solve, estimated from the previous HO solution for $I^{n+1}(x, \mu)$, as explained below. For the initial LO solve for each time step, the parameters are calculated with $I^n(x, \mu)$ from the previous HO solve. The discrete LO equations always conserve total energy, independent of the accuracy of the consistency terms. Additionally, the implicit time discretization, with sufficient convergence of the nonlinear emission source, will ensure that the method will not exhibit maximum principle violations [22].

Our LO operator is different from the nonlinear diffusion acceleration (NDA) methods used by other HOLO methods [1, 5, 4]. In NDA methods, an ad hoc term is added to the LO equations to enforce consistency and estimated using a previous HO solution. In our method we simply algebraically manipulated space-angle moment equations to produce our consistency terms, and then introduce a spatial closure. This should produce more stability in optically-thick regions where NDA methods demonstrate stability issues, although a formal stability analysis has not been performed.

The directionality of the half-range integrals are convenient for closing the equa-

tions spatially with a discontinuous trial space. Spatially, the radiation moment equations are closed using either a linear-discontinuous (LD) closure or with a parametric relation derived from the HO solution. A linear-discontinuous finite-element (LDFE) representation of $T(x)$ and $T^4(x)$ are used to eliminate the remaining spatial unknowns. The LDFE spatial discretization correctly preserves the equilibrium diffusion limit, a critical aspect for TRT equations [15, 14]. Also, the LDFE representation of the emission source mitigates artificial propagation of radiation energy across a spatial cell.

The solution to the LO system is used to construct a LDFE spatial representation of the isotropic scattering and emission sources on the right hand side of Eq. (2.1). This defines a fixed-source, pure absorber transport problem for the HO operator, with an emission source that is truly implicit in time. This HO transport problem represents a characteristic method that uses MC to invert the continuous streaming plus removal operator with an LDFE representation of sources; the representation of sources is similar to the linear moments method discussed in [32]. We will solve this transport problem, which has the form of a steady-state transport equation, using the ECMC method. The output from ECMC is $\tilde{I}^{n+1}(x, \mu)$, a space-angle LDFE projection of the exact solution $I^{n+1}(x, \mu)$ to the described transport problem. Once computed, $\tilde{I}^{n+1}(x, \mu)$ is used to directly evaluate the necessary consistency parameters for the next LO solve. Since there is a global, functional representation of the angular intensity, LO parameters are estimated using quadrature and do not require additional tallies. The HO solution is not used to directly estimate a new temperature at the end of the time step; it is only used to estimate the angular consistency parameters for the LO equations, which eliminates typical operator splitting stability issues that require linearization of the emission source.

Sufficient MC histories must be performed to eliminate statistical noise in the

consistency terms that can contaminate the LO solution. Exponentially-convergent Monte Carlo (ECMC)[28, 6] provides an algorithm that can efficiently reduce statistical noise to the same order as the HOLO iteration error with significantly less particle histories than standard MC. Additionally, each particle history requires less computational cost in particle tracking than IMC because no scattering events occurs in the HO solver. In particular, ECMC is exceptionally efficient in time-dependent TRT problems because the projection of the intensity from the previous time step can be used as an accurate initial guess for the new end of time step intensity. Additionally, no particle histories are required in regions where the radiation and material energy field are in equilibrium, similar to [1]. However, implementation of ECMC is non-trivial, requiring a finite-element representation of the solution in all phase-space variables that are being sampled with MC. The fundamental transport of particles is the same as standard Monte Carlo transport codes, but the source will now contain positive and negative weight particles.

One HOLO fixed-point iteration k denotes the process of an ECMC solve of the HO problem to estimate LO parameters, based on the current LO estimate of sources, followed by a solution of the LO system for $T^{n+1}(x)$ and $\phi^{n+1}(x)$. The process of performing subsequential HO and LO solves, within a single time step, can be repeated to obtain increasingly accurate solutions if the HO solution has sufficiently low statistical noise. Thus, the HOLO algorithm, for the n -th time step, is

1. Perform a LO solve to produce an initial guess for $T^{n+1,0}(x)$ and $\phi^{n+1,0}(x)$, based on consistency terms estimated with \tilde{I}^n .
2. Solve the HO system for $\tilde{I}^{n+1,k+1/2}(x, \mu)$ with ECMC, based on the current LO estimate of the emission and scattering sources.

3. Compute LO consistency parameters with $\tilde{I}^{n+1,k+1/2}$.
4. Solve the LO system with HO consistency parameters to produce a new estimate of $\phi^{n+1,k+1}$ and $T^{n+1,k+1}$.
5. Optionally repeat 2 – 4 until desired convergence is achieved.
6. Store $\tilde{I}^n \leftarrow \tilde{I}^{n+1}$, and move to the next time step.

where the superscript k denotes the outer HOLO iteration¹. The consistency terms force the HO and LO solutions for $\phi^{n+1}(x)$ to be consistent to the order of the current HOLO iteration error, as long as the LDFE spatial representation can accurately represent $\phi(x)$ and $T(x)$.

¹Throughout this dissertation, the outer HOLO iteration index k is often suppressed for visual clarity. Where necessary, subscript “*HO*” and “*LO*” are also used to indicate terms from respective solvers explicitly.

3. THE MOMENT-BASED LOW-ORDER EQUATIONS

The LO equations are based on moments, i.e., integrals of the equations, to produce a lower-dimensional system. The equations incorporate extra parameters, referred to as consistency terms, that allow for the equations to preserve the accuracy (particularly in angle) of the HO solver, which is detailed in the next chapter. The formulation of the LO equations is similar to a discontinuous FE method. Weighted integrals of the equations are taken using weight functions that have local support. The equations are written with element-wise moments of $I(x, \mu)$ and $T(x)$ as unknowns. Leaving the solution in this form allows for use of information from a previous HO solution to eliminate auxiliary unknowns from the equations. This is different than a standard Galerkin or collocation FE method [33, 14, 34] where a functional form of the solution is directly assumed. The final equations will have a similar form to S_2 equations, but we have not used a collocation method in angle, which should limit ray effects [34, 11] in higher spatial dimensions.

The remainder of this chapter is structured as follows: the general moments will be derived and then the use of HO information to close the system in angle is discussed. We then detail two separate spatial closures: a standard linear-discontinuous finite-element (LDFE) closure [14] and the use of the HO solution to define an exact closure. Details on solving the equations are also given.

3.1 Forming the Space-Angle Moment Equations

3.1.1 *LO Spatial Mesh and Finite-Element Spatial Moments*

The LO equations are formulated over a FE mesh. The domain for the i -th spatial element (or cell) has support $x \in [x_{i-1/2}, x_{i+1/2}]$ with width $h_i = x_{i+1/2} - x_{i-1/2}$ and cell center $x_i = x_{i-1/2} + h_i/2$. There is a total of N_c elements, spanning the

spatial domain $0 \leq x \leq X$. For simplicity, this spatial mesh is fixed throughout the simulation. Mesh adaptation is only applied in the HO solver, where applicable.

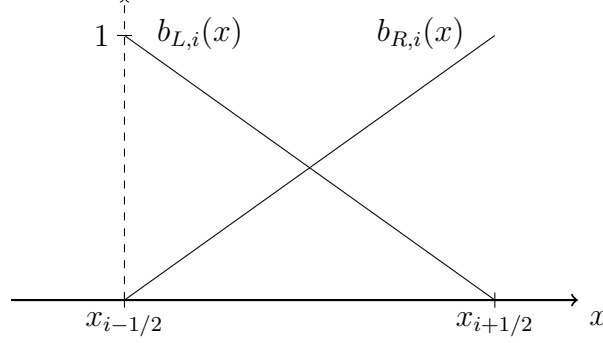


Figure 3.1: Illustration of linear finite element basis functions $b_{L,i}(x)$ and $b_{R,i}(x)$, for spatial element i .

The spatial moments are defined by integrals weighted with the standard linear finite element (FE) interpolatory basis functions. An illustration of the two linear FE basis functions for the i -th element (or cell) is given in Fig. 3.1. The left basis function is defined as

$$b_{L,i}(x) = \begin{cases} \frac{x_{i+1/2} - x}{h_i} & x_{i-1/2} \leq x \leq x_{i+1/2} \\ 0 & \text{elsewhere} \end{cases}, \quad (3.1)$$

corresponding to the node $x_{i-1/2}$. The right basis function is

$$b_{R,i}(x) = \begin{cases} \frac{x - x_{i-1/2}}{h_i} & x_{i-1/2} \leq x \leq x_{i+1/2} \\ 0 & \text{elsewhere} \end{cases}, \quad (3.2)$$

corresponding to the node $x_{i+1/2}$. With these definitions, a local linear approximation to a function f can be formulated as $f(x) \simeq f_{L,i}b_{L,i}(x) + f_{R,i}b_{R,i}(x)$, $x \in$

$[x_{i-1/2}, x_{i+1/2}]$.¹

The spatial moments are defined by integrals over the each element, using the two basis functions. We use $\langle \cdot \rangle$ to indicate weighted integration over a spatial element. The spatial moments are

$$\langle \cdot \rangle_{L,i} = \frac{2}{h_i} \int_{x_{i-1/2}}^{x_{i+1/2}} b_{L,i}(x)(\cdot)dx \quad (3.3)$$

and

$$\langle \cdot \rangle_{R,i} = \frac{2}{h_i} \int_{x_{i-1/2}}^{x_{i+1/2}} b_{R,i}(x)(\cdot)dx, \quad (3.4)$$

where the factor of $2/h_i$ is a normalization constant. In this notation $\langle \phi \rangle_{L,i}$ and $\langle \phi \rangle_{R,i}$ represent spatial moments of the intensity over cell i , as opposed to $\phi_{L,i}$ and $\phi_{R,i}$, which represent the interior value of the linear representation of $\phi(x)$ at $x_{i-1/2}$ and $x_{i+1/2}$ within the cell.

To simplify notation and discussion, we also define the slope and average moments over a spatial cell. The element-averaged scalar intensity is

$$\phi_i = \frac{1}{h_i} \int_{x_{i-1/2}}^{x_{i+1/2}} \phi(x)dx \quad (3.5)$$

and the average slope of the scalar intensity within the element is

$$\phi_{x,i} = \frac{6}{h_i} \int_{x_{i-1/2}}^{x_{i+1/2}} \left(\frac{x - x_i}{h_i} \right) \phi(x)dx. \quad (3.6)$$

The linear representation over a cell can be written as $\phi(x) = \phi_i + 2\phi_{x,i}(x - x_i)/h_i^2$, for $x \in (x_{i-1/2}, x_{i+1/2})$.

¹In literature the linear FE basis functions are formally defined with support over two adjacent elements. However, in our notation our functions only have non-zero support in element i . This accommodates our later definition of moments and discontinuous unknowns.

3.1.2 Definition of Angular Moments

To reduce the angular dimensionality, positive and negative half-range integrals of the angular intensity are taken. The angular integrals are denoted with a superscript as

$$(\cdot)^\pm = \pm \int_0^{\pm 1} (\cdot) d\mu \quad (3.7)$$

The half-range integrals of I are defined as $\phi^+(x) = \int_0^1 I(x, \mu) d\mu$ and $\phi^-(x) = \int_{-1}^0 I(x, \mu) d\mu$, respectively. Thus, in terms of half-range quantities, the mean intensity is $\phi = \phi^- + \phi^+$.

3.1.3 Space-Angle Moments of the Radiation Transport Equation

The LO radiation equations are formed by applying the space and angle moment operators to the transport equation and performing algebraic manipulation. We provide a detailed derivation of the L and $+$ radiation moment equation and state the final results for the other moment operators. The independent variables are often suppressed for some, or all, of the dependent variables for compactness.

First, the L moment operator is applied to the time-discretized transport equation, i.e., Eq. (2.1); application of integration by parts to the streaming term of the resulting equation yields

$$\begin{aligned} -\frac{2}{h_i} \mu I^{n+1}(x_{i-1/2}, \mu) + \frac{2}{h_i^2} \int_{x_{i-1/2}}^{x_{i+1/2}} \mu I^{n+1}(x, \mu) dx + \left(\sigma_{t,i}^{n+1} + \frac{1}{c\Delta t} \right) \langle I^{n+1}(x, \mu) \rangle_{L,i} \\ - \frac{\sigma_{s,i}}{2} \langle \phi^{n+1}(x) \rangle_{L,i} = \frac{1}{2} \langle \sigma_{a,i}^{n+1} acT^{n+1,4}(x) \rangle_{L,i} + \frac{1}{c\Delta t} \langle I^n(x, \mu) \rangle_{L,i}. \end{aligned} \quad (3.8)$$

Here, the cross sections have been assumed constant over a cell and evaluated with T^{n+1} . Now, the mean intensity in the scattering term is expanded in terms of half-range unknowns. The integral can be rewritten in terms of L and R moments by

noting that $b_{L,i}(x) + b_{R,i}(x) = 2/h_i$. These substitutions are made, independent variables are suppressed, and the resulting equation is multiplied by h_i to produce

$$-2\mu I_{i-1/2}^{n+1} + \langle \mu I^{n+1} \rangle_{L,i} + \langle \mu I^{n+1} \rangle_{R,i} + \left(\sigma_{t,i}^{n+1} + \frac{1}{c\Delta t} \right) h_i \langle I^{n+1} \rangle_{L,i} - \frac{\sigma_{s,i} h_i}{2} (\langle \phi \rangle_{L,i}^{n+1,+} + \langle \phi \rangle_{L,i}^{n+1,-}) = \frac{h_i}{2} \langle \sigma_a^{n+1} ac T^{n+1,4} \rangle_{L,i} + \frac{h_i}{c\Delta t} \langle I^n \rangle_{L,i}, \quad (3.9)$$

where $I_{i-1/2}(\mu) \equiv I(x_{i-1/2}, \mu)$. The resulting equation is integrated over the positive half range:

$$-2 \left(\mu I_{i-1/2}^{n+1} \right)^+ + \langle \mu I^{n+1} \rangle_{L,i}^+ + \langle \mu I^{n+1} \rangle_{R,i}^+ + \left(\sigma_{t,i}^{n+1} + \frac{1}{c\Delta t} \right) h_i \langle \phi \rangle_{L,i}^{n+1,+} - \frac{\sigma_{s,i} h_i}{2} (\langle \phi \rangle_{L,i}^{n+1,+} + \langle \phi \rangle_{L,i}^{n+1,-}) = \frac{h_i}{2} \langle \sigma_a^{n+1} ac T^{n+1,4} \rangle_{L,i} + \frac{h_i}{c\Delta t} \langle \phi \rangle_{L,i}^{n,+}. \quad (3.10)$$

3.1.4 The Angular Consistency Terms

Now, algebraic manipulations are performed on the streaming terms to produce face and volume averages of μ , weighted by the intensity. Each term in the streaming term of Eq. (3.10) is multiplied by a factor of unity, with the desired unknown appropriate to each term in the numerator and denominator, as in [27]. Temporarily dropping the time index for clarity, the manipulations applied to the streaming term are as follows:

$$\left\langle \mu \frac{\partial I}{\partial x} \right\rangle_L^+ = -\frac{2}{h_i} (\mu I_{i-1/2})^+ + \frac{1}{h_i} [\langle \mu I \rangle_{L,i}^+ + \langle \mu I \rangle_{R,i}^+] \quad (3.11)$$

$$= -\frac{2}{h_i} (\mu I_{i-1/2})^+ \frac{(I_{i-1/2})^+}{(I_{i-1/2})^+} + \frac{1}{h_i} \left[\langle \mu I \rangle_{L,i}^+ \frac{\langle I \rangle_{L,i}^+}{\langle I \rangle_{L,i}^+} + \langle \mu I \rangle_{R,i}^+ \frac{\langle I \rangle_{R,i}^+}{\langle I \rangle_{R,i}^+} \right] \quad (3.12)$$

$$= -\frac{2}{h_i} \left\{ \frac{(\mu I)_{i-1/2}^+}{\phi_{i-1/2}^+} \right\} \phi_{i-1/2}^+ + \frac{1}{h_i} \left[\left\{ \frac{\langle \mu I \rangle_{L,i}^+}{\langle \phi \rangle_{L,i}^+} \right\} \langle \phi \rangle_{L,i}^+ + \left\{ \frac{\langle \mu I \rangle_{R,i}^+}{\langle \phi \rangle_{R,i}^+} \right\} \langle \phi \rangle_{R,i}^+ \right] \quad (3.13)$$

The ratios in braces are what we will formally define as *angular consistency terms*. These nonlinear functionals are approximated by the HO solver, similar to the approach in [27]. The angular consistency term for the L and $+$ moments is defined as

$$\{\mu\}_{L,i}^{n+1,+} \equiv \frac{\langle \mu I^{n+1} \rangle_{L,i}^+}{\langle I^{n+1} \rangle_{L,i}^+} = \frac{\frac{2}{h_i} \int_0^1 \int_{x_{i-1/2}}^{x_{i+1/2}} \mu b_{L,i}(x) I^{n+1}(x, \mu) dx d\mu}{\frac{2}{h_i} \int_0^1 \int_{x_{i-1/2}}^{x_{i+1/2}} b_{L,i}(x) I^{n+1}(x, \mu) dx d\mu}. \quad (3.14)$$

The consistency terms on the face represent averaging at a point, with a similar definition as

$$\mu_{i+1/2}^+ \equiv \frac{(\mu I_{i+1/2})^+}{\phi_{i+1/2}^+} = \frac{\int_0^1 \mu I(x_{i+1/2}, \mu) d\mu}{\int_0^1 I(x_{i+1/2}, \mu) d\mu}. \quad (3.15)$$

There are analogous definitions for the R and $-$ moments, e.g.,

$$\{\mu\}_{R,i}^{n+1,-} \equiv \frac{\langle \mu I^{n+1} \rangle_{R,i}^-}{\langle I^{n+1} \rangle_{R,i}^-} = \frac{\frac{2}{h_i} \int_{-1}^0 \int_{x_{i-1/2}}^{x_{i+1/2}} \mu b_{R,i}(x) I^{n+1}(x, \mu) dx d\mu}{\frac{2}{h_i} \int_{-1}^0 \int_{x_{i-1/2}}^{x_{i+1/2}} b_{R,i}(x) I^{n+1}(x, \mu) dx d\mu}. \quad (3.16)$$

Substitution of Eq. (3.16) and (3.15) simplifies moments of the streaming term for the L and $+$ operators:

$$\left\langle \mu \frac{\partial I}{\partial x} \right\rangle_L^+ = -\frac{2}{h_i} \mu_{i-1/2}^+ I_{i-1/2}^+ + \frac{1}{h_i} \left[\{\mu\}_{L,i}^+ \langle \phi \rangle_{L,i}^+ + \{\mu\}_{R,i}^+ \langle \phi \rangle_{R,i}^+ \right] \quad (3.17)$$

It is noted that this expression does not contain a cross section in the denominator, such as in the variable Eddington factor approach [35], eliminating issues in a void where $\sigma_t = 0$.

3.1.5 The Exact Radiation Moment Equations

A final form of the moment equation resulting from application of the L moment and positive half-range integral is obtained by substitution of Eq. (3.17) into Eq. (3.10):

$$\begin{aligned} & -2\mu_{i-1/2}^{n+1,+} \phi_{i-1/2}^{n+1,+} + \{\mu\}_{L,i}^{n+1,+} \langle \phi \rangle_{L,i}^{n+1,+} + \{\mu\}_{R,i}^{n+1,+} \langle \phi \rangle_{R,i}^{n+1,+} + \left(\sigma_{t,i}^{n+1} + \frac{1}{c\Delta t} \right) h_i \langle \phi \rangle_{L,i}^{n+1,+} \\ & - \frac{\sigma_{s,i} h_i}{2} (\langle \phi \rangle_{L,i}^{n+1,+} + \langle \phi \rangle_{L,i}^{n+1,-}) = \frac{h_i}{2} \langle \sigma_a^{n+1} acT^{n+1,4} \rangle_{L,i} + \frac{h_i}{c\Delta t} \langle \phi \rangle_{L,i}^{n,+}, \quad (3.18) \end{aligned}$$

The other radiation moment equations are derived analogously. Pairwise application of the L and R basis moments with the $+$ and $-$ half-range integrals to Eq. (2.1) ultimately yields four moment equations per cell. The equation for the R and $+$ moment is

$$\begin{aligned} & 2\mu_{i+1/2}^{n+1,+} \phi_{i+1/2}^{n+1,+} - \{\mu\}_{L,i}^{n+1,+} \langle \phi \rangle_{L,i}^{n+1,+} - \{\mu\}_{R,i}^{n+1,+} \langle \phi \rangle_{R,i}^{n+1,+} + \left(\sigma_{t,i}^{n+1} + \frac{1}{c\Delta t} \right) h_i \langle \phi \rangle_{R,i}^{n+1,+} \\ & - \frac{\sigma_{s,i} h_i}{2} (\langle \phi \rangle_{R,i}^{n+1,+} + \langle \phi \rangle_{R,i}^{n+1,-}) = \frac{h_i}{2} \langle \sigma_a^{n+1} acT^{n+1,4} \rangle_{R,i} + \frac{h_i}{c\Delta t} \langle \phi \rangle_{R,i}^{n,+}, \quad (3.19) \end{aligned}$$

The equations for the negative half-range moment are identical to the above with the negative half-range integrals replacing the positive where applicable. Explicitly,

$$\begin{aligned} & -2\mu_{i-1/2}^{n+1,-} \phi_{i-1/2}^{n+1,-} + \{\mu\}_{L,i}^{n+1,-} \langle \phi \rangle_{L,i}^{n+1,-} + \{\mu\}_{R,i}^{n+1,-} \langle \phi \rangle_{R,i}^{n+1,-} + \left(\sigma_{t,i}^{n+1} + \frac{1}{c\Delta t} \right) h_i \langle \phi \rangle_{L,i}^{n+1,-} \\ & - \frac{\sigma_{s,i} h_i}{2} (\langle \phi \rangle_{L,i}^{n+1,+} + \langle \phi \rangle_{L,i}^{n+1,-}) = \frac{h_i}{2} \langle \sigma_a^{n+1} acT^{n+1,4} \rangle_{L,i} + \frac{h_i}{c\Delta t} \langle \phi \rangle_{L,i}^{n,-} \quad (3.20) \end{aligned}$$

and

$$2\mu_{i+1/2}^{n+1,-} \phi_{i+1/2}^{n+1,-} - \{\mu\}_{L,i}^{n+1,-} \langle \phi \rangle_{L,i}^{n+1,-} - \{\mu\}_{R,i}^{n+1,-} \langle \phi \rangle_{R,i}^{n+1,-} + \left(\sigma_{t,i}^{n+1} + \frac{1}{c\Delta t} \right) h_i \langle \phi \rangle_{R,i}^{n+1,-}$$

$$-\frac{\sigma_{s,i}h_i}{2}(\langle\phi\rangle_{R,i}^{n+1,+} + \langle\phi\rangle_{R,i}^{n+1,-}) = \frac{h_i}{2}\langle\sigma_a^{n+1}acT^{n+1,4}\rangle_{R,i} + \frac{h_i}{c\Delta t}\langle\phi\rangle_{R,i}^{n,-}, \quad (3.21)$$

Ultimately, the two half-ranges will be treated differently when the equations are closed spatially due to upwinding in direction.

3.1.6 Material Energy Equations

To derive the LO material energy equations, an approximation must be introduced to relate $T(x)$ and $T^4(x)$ within a cell. We represent $T(x)$ spatially with a LDFE trial space, i.e., $T(x) \simeq T_{L,i}b_{L,i}(x) + T_{R,i}b_{R,i}(x)$, $x \in (x_{i-1/2}, x_{i+1/2})$. This trial space will ensure preservation of the equilibrium diffusion limit and limit artificial propagation of energy across the system [24]. Similarly, the emission term is represented in the material and radiation equations with the LDFE interpolant $T^4(x) \simeq T_{L,i}^4b_{L,i}(x) + T_{R,i}^4b_{R,i}(x)$. The L and R spatial moments are taken of the material energy equations, and the LDFE representations for $T(x)$ and $\sigma_a acT^4(x)$ are used to simplify the spatial integrals. The final LO material energy equation resulting from application of the L moment is

$$\begin{aligned} \frac{\rho_i c_{v,i}}{\Delta t} \left[\left(\frac{2}{3}T_{L,i} + \frac{1}{3}T_{R,i} \right)^{n+1} - \left(\frac{2}{3}T_{L,i} + \frac{1}{3}T_{R,i} \right)^n \right] + \sigma_{a,i}^{n+1} (\langle\phi\rangle_{L,i}^+ + \langle\phi\rangle_{L,i}^-)^{n+1} \\ = \sigma_{a,i}^{n+1} ac \left(\frac{2}{3}T_{L,i}^4 + \frac{1}{3}T_{R,i}^4 \right)^{n+1}. \end{aligned} \quad (3.22)$$

The equation for the R moment is

$$\begin{aligned} \frac{\rho_i c_{v,i}}{\Delta t} \left[\left(\frac{1}{3}T_{L,i} + \frac{2}{3}T_{R,i} \right)^{n+1} - \left(\frac{1}{3}T_{L,i} + \frac{2}{3}T_{R,i} \right)^n \right] + \sigma_{a,i}^{n+1} (\langle\phi\rangle_{R,i}^+ + \langle\phi\rangle_{R,i}^-)^{n+1} \\ = \sigma_{a,i}^{n+1} ac \left(\frac{1}{3}T_{L,i}^4 + \frac{2}{3}T_{R,i}^4 \right)^{n+1}. \end{aligned} \quad (3.23)$$

Cross sections have been assumed constant over each element, evaluated at the average temperature within the element, i.e., $\sigma_{a,i}^{n+1} = \sigma_{a,i}([T_{L,i}^{n+1} + T_{R,i}^{n+1}]/2)$. Because the material energy balance equation only contains angularly integrated quantities, there is no need to take angular moments of the above equations.

3.2 Closing the LO Equations in Space and Angle

At this point, the LO equations have too many unknowns: the relation between the volume and face averaged quantities and the angular consistency parameters are not known a priori. The HO solution is used to eliminate the consistency parameters and other approximations are used to eliminate the extra spatial unknowns from the equations. The six desired degrees of freedom (DOF) over each cell i are the four moments $\langle \phi \rangle_{L,i}^+$, $\langle \phi \rangle_{R,i}^+$, $\langle \phi \rangle_{L,i}^-$, and $\langle \phi \rangle_{R,i}^-$ and the two spatial edge values $T_{L,i}$ and $T_{R,i}$. After closure, the four radiation and two material energy equations define a system of equations for the six DOF, coupled spatially through the streaming term.

Before introducing the additional closures, we emphasize that at this point the only spatial or angular approximations to the radiation moment equations are an LDFF representation for $T^4(x)$ and cell-averaged cross sections; these moment equations are exact with respect to the chosen time discretization and these approximations. The material energy equations, as well as the emission source, required an approximation of LDFF in space for $T(x)$ and $T^4(x)$. Some approximation is always necessary to relate T and T^4 .

3.2.1 Angular Closure

The angular consistency parameters (e.g., Eq. (3.16) and (3.15)) are not known a priori. A lagged estimate of I^{n+1} from the previous HO solve is used to estimate the angular consistency parameters. In the HOLO algorithm, the equations for LO unknowns at iteration $k + 1$ use consistency parameters computed using the latest

HO solution $\tilde{I}^{n+1,k+1/2}$ as an approximation for $I^{n+1}(x, \mu)$, e.g.,

$$\{\mu\}_{L,i}^{n+1,+} \simeq \frac{\langle \mu \tilde{I}_{HO}^{n+1,k+1/2} \rangle_{L,i}^+}{\langle \tilde{I}_{HO}^{n+1,k+1/2} \rangle_{L,i}^+} = \frac{\frac{2}{h_i} \int_0^1 \int_{x_{i-1/2}}^{x_{i+1/2}} \mu b_{L,i}(x) \tilde{I}_{HO}^{n+1,k+1/2}(x, \mu) dx d\mu}{\frac{2}{h_i} \int_0^1 \int_{x_{i-1/2}}^{x_{i+1/2}} b_{L,i}(x) \tilde{I}_{HO}^{n+1,k+1/2}(x, \mu) dx d\mu}. \quad (3.24)$$

We evaluate these terms using quadrature based on the LDFE functional representation $\tilde{I}_{HO}(x, \mu)$ provided by the HO solution.

3.2.2 LDFE Spatial Closure

After approximating the angular consistency terms in the time-discretized LO moment equations, a equation relating the spatial moments and outflow face values is needed to eliminate the final auxiliary unknowns, i.e., a spatial closure. We will eliminate the face terms to produce equations exclusively in terms of the desired moment unknowns. Several closures were investigated. The simplest closure is a linear-discontinuous (LD) spatial closure with the usual upwinding approximation [14]. A closure based on the HO solution is discussed in Sec. 3.6. Because there are no derivatives of T in Eq. (2.2), there is no need to define T on the faces in Eq. (3.22) and Eq. (3.23); only moments of ϕ appear in the material energy equations, thus they are fully defined at this point and require no additional spatial closure.

Now, the LDFE closure is applied to the radiation moment equations for the case of positive flow (i.e., Eq. (3.18) and (3.19)). The LD closure over for the i -th cell and positive μ is illustrated in Fig. 3.2. The face terms $\mu_{i-1/2}$ and $\phi_{i-1/2}$ are upwinded from the previous cell $i-1$ or from a boundary condition; the terms at $x_{i+1/2}$ are linearly extrapolated, computed using the L and R basis moments. The linear approximation $\phi^+(x) = b_{L,i}(x)\phi_{L,i}^+ + b_{R,i}(x)\phi_{R,i}^+$, for $x \in (x_{i-1/2}, x_{i+1/2}]$,

is substituted into the definition for the moments (i.e., Eq. (3.3) and (3.4)) and solved for the LD edge value $\phi_{i,R}^+$; The resulting outflow relation for positive flow is $\phi_{i+1/2}^+ \equiv \phi_{i,R}^+ = 2\langle\phi\rangle_{R,i}^+ - \langle\phi\rangle_{L,i}^+$; the LD closure for the negative half range produces $\phi_{i-1/2}^- = 2\langle\phi\rangle_{L,i}^- - \langle\phi\rangle_{R,i}^+$. The L moment and positive half-range equation with the LD closure and upwinding is

$$\begin{aligned}
& -2\mu_{i-1/2}^{n+1,+} \left(2\langle\phi\rangle_{R,i-1}^{n+1,+} - \langle\phi\rangle_{L,i-1}^{n+1,+} \right) + \{\mu\}_{L,i}^{n+1,+} \langle\phi\rangle_{L,i}^{n+1,+} + \{\mu\}_{R,i}^{n+1,+} \langle\phi\rangle_{R,i}^{n+1,+} \\
& + \left(\sigma_{t,i}^{n+1} + \frac{1}{c\Delta t} \right) h_i \langle\phi\rangle_{L,i}^{n+1,+} - \frac{\sigma_{s,i} h_i}{2} \left(\langle\phi\rangle_{L,i}^{n+1,+} + \langle\phi\rangle_{L,i}^{n+1,-} \right) \\
& = \frac{h_i}{2} \langle\sigma_a^{n+1} acT^{n+1,4}\rangle_{L,i} + \frac{h_i}{c\Delta t} \langle\phi\rangle_{L,i}^{n,+}. \quad (3.25)
\end{aligned}$$

Similar equations can be derived for the other directions and moments, fully defining the radiation equations. The closed equations are equivalent in numerical complexity to an LDFE discretization of the S_2 equations [14, 11], but with different quadrature points on the face and interior.

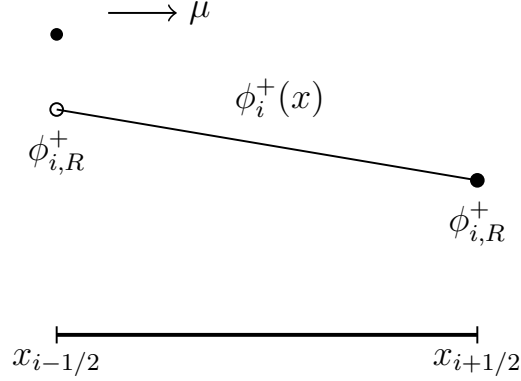


Figure 3.2: Linear-discontinuous trial space for half-range mean intensity and $\mu > 0$, in LO equations.

Note that we have chosen to leave $\mu_{i-1/2}^{n+1,+}$ as a value to be estimated from the HO solver, which is more conducive to the HO spatial closures described in Sec. 3.6. Alternatively, the spatial closure could be introduced before performing the algebraic manipulation to form consistency terms (e.g., into Eq. (3.11)). This would produce only volume-weighted consistency terms in the equations.

3.2.3 Boundary Conditions

For all spatial closures, the specified incident angular intensity is incorporated into the upwinding term of the appropriate radiation moment equation. At the left boundary, the upwinded current is known, so for that L moment equation

$$\mu_{1/2}^+ \phi_{1/2}^+ = \int_0^1 \mu I^{inc,+}(\mu) d\mu, \quad (3.26)$$

where $I^{inc,+}(\mu)$ is the specified incident angular intensity at the left boundary. For all results in this work, only isotropic incident intensities were considered. A similar expression is derived for the right boundary. For S_2 -equivalent LO solves, i.e., all consistency terms are $\pm 1/\sqrt{3}$, the half-range flux in the above equation is renormalized by multiplying the term in the moment equations by $2/\sqrt{3}$ to produce accurate solutions [34].

3.3 Newton's Method for LO Equations

Summation over all cells of the closed equations forms a global system of coupled equations. The equations are nonlinear due to the Planckian emission source and, for some problems, the temperature-dependent material properties. We have used a local, hybrid Picard-Newton method to solve the nonlinear system, based on a standard linearization of the Planckian source with cross sections evaluated at temperatures from the previous iteration, as described in [14]. A derivation of the LO

Picard-Newton equations is given in A.2.

The equations for each half-range are coupled together via scattering. In one spatial dimension, the scattering terms can be included in the discrete system matrix and directly inverted. We consider an alternative iterative solution method that could be more easily extended to higher spatial dimensions in Chapter 6. For the direct solution method, isotropic scattering, including effective scattering terms from the linearization, are included in the system matrix. The system matrix is an asymmetric, banded matrix with a band width of seven and is inverted directly. Newton iterations are repeated until $\phi^{n+1}(x)$ and $T^{n+1}(x)$ are converged to a desired relative tolerance. Convergence in the Newton iterations is calculated using the spatial L_2 norm of the change in $\phi^{n+1}(x)$ and $T^{n+1}(x)$, relative to the norm of each solution.

In certain problems, the nonlinearities of the system can lead to divergence of the Newton iterations. This is often the result of taking relatively large time steps for problems with large values of σ_a and small values of ρc_v . To prevent divergence, a damped Newton method [36] can be used, at the cost of increased numbers of iterations. For a damped Newton's method, the estimated change in the solution between iterations is multiplied by a factor $\xi \in (0, 1)$, where ξ is referred to as the damping factor. Sufficient reduction of the change in solutions between iterations will allow iterations to continue converging, by ensuring the solution remains within the domain of convergence. The details of modifying the Newton iterations in this work to include a damping factor are given in App. A.2.1. For simplicity, a fixed value of ξ was used for all iterations in problems where damping was found to be necessary.

3.4 Accuracy of LO Equations in the Equilibrium Diffusion Limit

In our LO scheme, the LO equations use an LDFE representation for the temperature. The radiation terms can also be closed with an LDFE closure. In the EDL limit, the MC HO solution will estimate angular consistency terms associated with an isotropic intensity, based on a spatially LD emission source. This produces LO equations that are equivalent to the S_2 equations, but with quadrature points defined by $\pm 1/2$. Because the spatial closure produces equations that are equivalent to an LDFE solution to the S_2 equations, we expect the equations to preserve the equilibrium diffusion limit; the LDFE discretization of the S_2 equations is known to preserve the EDL based on discrete asymptotic analysis [14].

3.5 Fixups for Negative Solutions with LDFE Closure

The linear-discontinuous (LD) closure with upwinding is not strictly positive. In particular, for optically thick cells with a steep intensity gradient, the linear representations for $\phi(x)$ and $T(x)$ can go below the floor temperature or negative. The floor temperature T_{\min} is defined as the initial temperature of the material and radiation in problems where boundary sources are applied at each of the boundaries. In such problems the radiation and material should continue to heat on the interior of the domain, and physically should not fall below the initial temperature. Negative values of intensity can propagate to adjacent cells. In thick regions of TRT problems, reasonably fine spatial cells can still be on the order of millions of mean free paths; negative values with an LD representation are unavoidable in practice for such cells and mesh refinement is of minimal use.

Typically, for a standard LDFE Galerkin spatial discretization, the equations are lumped to produce a discretization that is strongly resistant to negative values (for 1D) [14]. However, standard FE lumping procedures would introduce difficulties

in computing the consistency terms from the HO solution. Alternatively, we have derived a modified spatial closure that produces unknowns equivalent to those from a lumped LD method in 1D. The L and R moments are defined the same as before, preserving the average within a cell, but the relation between the moments and the outflow is modified. In the lumping-equivalent closure, the outflows are defined as

$$\phi_{i+1/2}^+ = \langle \phi \rangle_{i,R}^+ \quad (3.27)$$

$$\phi_{i-1/2}^- = \langle \phi \rangle_{i,L}^-. \quad (3.28)$$

The system is then fully defined with upwinding and the assumption of a linear relationship on interior of the element. This modified closure produces a linear representation that preserves zeroth moment, but the relation between the slope of the line and the first spatial moment has been modified. Because the basis functions $b_{R,i}(x)$ and $b_{L,i}(x)$ are strictly positive, the outflows tends to be positive. Strong sources and gradients can still lead to negativities at the edges of the LD representation. Details on the derivation of this relation are in Appendix A.1. The lumping closure was optionally applied in all cells or only in cells where negative intensities occur.

For simplicity, we also lump the emission source and temperature terms in the equations following the standard procedure [14]. For example, the lumped version of Eq. (3.22) is

$$\frac{\rho_i c_{v,i}}{\Delta t} (T_{L,i}^{n+1} - T_{L,i}^n) + \sigma_{a,i}^{n+1} (\langle \phi \rangle_{L,i}^+ + \langle \phi \rangle_{L,i}^-)^{n+1} = \sigma_{a,i}^{n+1} a c (T_{L,i}^{n+1})^4 \quad (3.29)$$

noting that no modification was made to the radiation moment term in this equation. It was found that lumping the temperature equations generally produced more

robustness than exclusively modifying the spatial closure, but it is not necessary for all problems.

3.5.1 Balance Preserving Fixup

We also investigated an alternative closure of the equations based on energy conservation and forcing the appropriate edge value to be the floor value. The equations within cells that produce a negativity are modified to ensure the edge intensities are not below the floor temperature, and energy balance is conserved. This fixup is applied in cells where a negative intensity is detected during a Newton iteration. For example, if $\phi_{R,i}^+$ is found to be negative, the modified equations (for the positive half range) in that cell are the balance equation, i.e.,

$$\begin{aligned}
& -\mu_{i-1/2}^{n+1,+} (2\langle\phi\rangle_{R,i-1}^{n+1,+} - \langle\phi\rangle_{L,i-1}^{n+1,+}) + \mu_{i+1/2}^{n+1,+} (2\langle\phi\rangle_{R,i}^{n+1,+} - \langle\phi\rangle_{L,i}^{n+1,+}) \\
& + \left(\sigma_{t,i}^{n+1} + \frac{1}{c\Delta t} \right) \frac{h_i}{2} (\langle\phi\rangle_{L,i}^{n+1,+} + \langle\phi\rangle_{R,i}^{n+1,+}) - \frac{\sigma_{s,i}h_i}{4} (\langle\phi\rangle_{L,i}^{n+1} + \langle\phi\rangle_{R,i}^{n+1}) \\
& = \frac{h_i}{4} \sigma_{a,i}^{n+1} ac (\langle T^{n+1,4} \rangle_{L,i} + \langle T^{n+1,4} \rangle_{R,i}) + \frac{h_i}{2c\Delta t} (\langle\phi\rangle_{L,i}^{n,+} + \langle\phi\rangle_{R,i}^{n,+}) \quad (3.30)
\end{aligned}$$

and the closure equation, i.e.,

$$2\langle\phi\rangle_{i,R}^+ - \langle\phi\rangle_{i,L}^+ = T_{\min}. \quad (3.31)$$

Because our solution method directly inverts the LO system, negative edge intensities must be detected, the fix-up applied locally to all elements and half-ranges where necessary, and then that Newton solve repeated. In practice, this flooring procedure was observed to produce positive answers, but was not as robust as the lumping closure in all cells. In general, as the time step size or problem nonlinearities were increased, this fixup led to the Newton solves diverging.

3.6 Spatial Closure Based on the HO Solution

This section describes an alternative spatial closure to the LO equations with a parametric relation determined with the HO solution. In addition to estimating the angular consistency terms, the HO intensity is used to estimate a relation between volume and face-averaged intensities to eliminate the face unknowns from the LO equations. The goal is to improve consistency compared to the LDFE discretization, although additional statistical noise is introduced through face-based tallies. In the remainder of this section, we motivate the HO spatial closure by manipulating a half-range balance equations to form a single unknown for each cell and half range. We will then discuss the forms of HO spatial closures investigated, based on modifications to standard spatial closures.

3.6.1 Motivation

Independent of angular accuracy and convergence of outer iterations, the LDFE closure of the LO equations will generally not produce the same moments as the LDFE projection of the HO solution. As an example of this difference, in the LO equations the linearly extrapolated outflow from one cell is defined as the inflow into the next cell through upwinding. For the HO solver, the linear, projected MC outflow from a spatial cell does not match the actual energy that flowed into a downstream cell via MC particles. Thus, we introduce additional unknowns at the face of cells to exactly capture the relation between moments and face values.

A half-range balance equation for $\mu > 0$ is formed by adding the exact L and R radiation moment equations given by Eq. (3.18) and (3.19), i.e.,

$$\mu_{i+1/2}^+ \phi_{i+1/2}^+ - \mu_{i-1/2}^+ \phi_{i-1/2}^+ + \sigma_{a,i} h_i \phi_i^+ = \frac{h_i}{2} q_i, \quad (3.32)$$

where q_i represents the cell-averaged emission source. In the HOLO algorithm, after estimating the consistency terms $\mu_{i\pm 1/2}^+$, unwinding the inflow term $\phi_{i-1/2}^+$, an additional equation is needed to eliminate the outflow $\phi_{i+1/2}^+$ to produce an equation for a single unknown ϕ_i^+ . Standard spatial discretizations techniques use a fixed approximation for all cells to eliminate the outflow in terms of other unknowns. Alternatively, the HO solution can be used to estimate a parametric relation between the other unknowns and the outflow, i.e.,

$$\phi_{i+1/2}^+ = f(\gamma_i^{+,HO}, \phi_i^+, \phi_{x,i}^+, \phi_{i-1/2}^+), \quad (3.33)$$

where $\gamma_i^{HO,+}$ is a local constant to be estimated with the HO solution and f is some function of some number of the input variables. The ECMC solution can provide all of the unknowns in the above equation, so the value of γ_i^{HO} can be determined directly.

If the problem were linear, or the nonlinear problem was fully converged, then application of this closure can ensure that the HO and LO equations produce the same moments, preserving the HO solution. To produce the same zeroth moment, the HO solution must also satisfy the local balance equation, e.g., Eq. (3.32). Then the LO equations and HO equations will have the same moments to satisfy both Eq. (3.33) and Eq. (3.32), upon nonlinear convergence of the outer HOLO iterations. To accurately reproduce the L and R basis moments, then the HO and LO solutions must also satisfy the first moment equation.

As TRT problems are non-linear (i.e., scattering or thermal emission are included in q), the moments will only be preserved upon non-linear convergence of the source. The nonlinearity introduces the possibility for stability issues, particularly with MC noise. However, we have already consistently formed angular consistency terms, so

the the spatial closure should be more stable than introducing auxiliary terms, such as in NDA methods [1, 4], but has a higher memory cost per spatial cell.

3.6.2 Choice of Spatial Closure

We will explore two different closure relations based on modifications to the standard LD closure: a scaled slope, i.e.,

$$\phi_{i\pm 1/2}^{\pm} = \phi_i^+ \pm \gamma_i^{\pm} \phi_{x,i}^+ \quad (3.34)$$

and a scaled average

$$\phi_{i\pm 1/2}^{\pm} = \gamma_i^{\pm} \phi_i^+ \pm \phi_{x,i}^+, \quad (3.35)$$

where a value of $\gamma_i = 1$ produces the standard linear discontinuous expressions for the extrapolated outflows. Our LO system is formulated in terms of L and R moments, rather than the average and slope. Thus, Eq. (3.34) and (3.35) are expressed in terms of the L and R unknowns, using the relations given in App. A.1. In terms of these moments, the scaled-slope closure is

$$\phi_{i+1/2}^+ = \left(\frac{1 - 3\gamma_i^+}{2} \right) \langle \phi \rangle_{L,i}^+ + \left(\frac{1 + 3\gamma_i^+}{2} \right) \langle \phi \rangle_{R,i}^+ \quad (3.36)$$

$$\phi_{i-1/2}^- = \left(\frac{1 + 3\gamma_i^-}{2} \right) \langle \phi \rangle_{L,i}^- + \left(\frac{1 - 3\gamma_i^-}{2} \right) \langle \phi \rangle_{R,i}^- \quad (3.37)$$

and the scaled-average relation is

$$\phi_{i+1/2}^+ = \left(\frac{\gamma_i^+ - 3}{2} \right) \langle \phi \rangle_{L,i}^+ + \left(\frac{\gamma_i^+ + 3}{2} \right) \langle \phi \rangle_{R,i}^+ \quad (3.38)$$

$$\phi_{i-1/2}^- = \left(\frac{\gamma_i^- + 3}{2} \right) \langle \phi \rangle_{L,i}^- + \left(\frac{\gamma_i^- - 3}{2} \right) \langle \phi \rangle_{R,i}^-. \quad (3.39)$$

The HO solution is used to estimate γ_i . The MC solution must be modified to

tally the MC estimated intensity on faces. For example, for $\mu > 0$, the LO equations for moments at $k + 1$ use closure parameters evaluated at $k + 1/2$ as

$$\gamma_i^{+,k+1} = \frac{\phi_{i+1/2}^{+,k+1/2} - \phi_i^{+,k+1/2}}{\phi_{x,i}^{+,k+1/2}}, \quad (3.40)$$

for the scaled-slope closure. For this closure, as the slope goes to zero this expression becomes undefined. In cells where the slope is $O(10^{-13}\psi_i)$, we use $\gamma_i = 1$. The main benefit of the scaled-slope closure is it allows for values of γ that are equivalent to other closures, as discussed in App. A.1: $\gamma_i = 0$ produces a step closure [15], which has a zero slope over the cell, and $\gamma_i = 1/3$ produces a lumping-equivalent closure.

3.6.3 The Linear Doubly-Discontinuous Trial Space

Because of the temperature unknowns and the HO scattering source representation, a representation on the interior of the cell for the temperature and intensity is needed for construction of sources in the HO solver. Thus, we introduce a linear doubly discontinuous (LDD) trial space for the half-range intensities, which is depicted in Fig. 3.3. The linear relation on the interior of the cell preserves the L and R moments of the solution, and the outflow from the cell is some parametric (i.e., non linear) extrapolation of those moments. The temperature is still represented with a linear interpolant of T^4 and T . This trial space has an extra unknown in the radiation equations for each cell and direction, which is eliminated from the system with the HO spatial closure. The ECMC algorithm is modified to also include a LDD trial space which allows for estimation of the solution at faces, as discussed later in Sec 4.5.

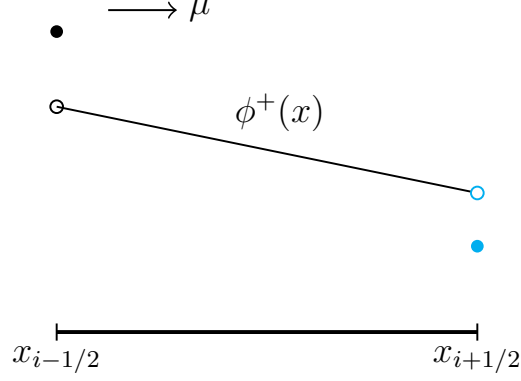


Figure 3.3: Linear doubly-discontinuous representation for mean intensity in LO equations.

To solve the LO equations, Eq. (3.36) or (3.38) is substituted locally for the appropriate outflow face term in each LO moment equation. There is a spatial closure parameter for each half-range, for each cell. The γ_i^\pm are estimated from the previous HO solution. For the initial LO solve within each time step, the outflow is assumed continuous, using the standard upwinding and LD closure. As an example, the positive half-range and L moment equation (i.e., Eq. (3.18)), for the scaled-slope closure, becomes

$$\begin{aligned}
& -2\mu_{i-1/2}^{n+1,+} \left[\left(\frac{1-3\gamma_{i-1}^{HO,+}}{2} \right) \langle \phi \rangle_{L,i-1}^+ + \left(\frac{1+3\gamma_{i-1}^{HO,+}}{2} \right) \langle \phi \rangle_{R,i-1}^+ \right] \\
& \quad + \{\mu\}_{L,i}^{n+1,+} \langle \phi \rangle_{L,i}^{n+1,+} + \{\mu\}_{R,i}^{n+1,+} \langle \phi \rangle_{R,i}^{n+1,+} \\
& \quad + \left(\sigma_{t,i}^{n+1} + \frac{1}{c\Delta t} \right) h_i \langle \phi \rangle_{L,i}^{n+1,+} - \frac{\sigma_{s,i} h_i}{2} (\langle \phi \rangle_{L,i}^{n+1,+} + \langle \phi \rangle_{L,i}^{n+1,-}) \\
& \quad = \frac{h_i}{2} \langle \sigma_a^{n+1} acT^{n+1,4} \rangle_{L,i} + \frac{h_i}{c\Delta t} \langle \phi \rangle_{L,i}^{n,+}, \quad (3.41)
\end{aligned}$$

and the R moment equation becomes

$$\begin{aligned}
& 2\mu_{i+1/2}^{n+1,+} \left[\left(\frac{1 - 3\gamma_i^{HO,+}}{2} \right) \langle \phi \rangle_{L,i}^+ + \left(\frac{1 + 3\gamma_i^{HO,+}}{2} \right) \langle \phi \rangle_{R,i}^+ \right] \\
& - \{\mu\}_{L,i}^{n+1,+} \langle \phi \rangle_{L,i}^{n+1,+} - \{\mu\}_{R,i}^{n+1,+} \langle \phi \rangle_{R,i}^{n+1,+} + \left(\sigma_{t,i}^{n+1} + \frac{1}{c\Delta t} \right) h_i \langle \phi \rangle_{R,i}^{n+1,+} \\
& - \frac{\sigma_{s,i} h_i}{2} (\langle \phi \rangle_{R,i}^{n+1,+} + \langle \phi \rangle_{R,i}^{n+1,-}) = \frac{h_i}{2} \langle \sigma_a^{n+1} a c T^{n+1,4} \rangle_{R,i} + \frac{h_i}{c\Delta t} \langle \phi \rangle_{R,i}^{n,+}. \quad (3.42)
\end{aligned}$$

These equations contain only the original desired radiation moment and LD temperature unknowns. During the Newton solve, once new half-range intensities are determined, the temperatures are updated using the same material energy equations as for the LD closure, i.e., Eq. (3.22) and Eq. (3.23).

Because the outflow from one cell is upwinded into the next cell, energy conservation by the LO equations is preserved. The closed equations have the same numerical complexity as the LDFE LO equations, but with an increased storage on the coarse mesh for the γ_i^\pm values. The linear representation for the interior solutions and emission source approaches the LD closure in the equilibrium diffusion limit, as long as the HO spatial closure is estimated with sufficient statistical accuracy.

3.6.4 Fixup for the Linear Doubly-Discontinuous Trial Space

The doubly discontinuous trial space presents an additional difficulty for resolving negative intensities because the outflow is now unhinged from the linear relationship. In the case of strong gradients, the interior representation and outflow can be driven negative. In such cases, we apply the lumping-equivalent relation from App. A.1 to define the linear representation. For example, the lumped emission source is

$$T = \langle T \rangle_{L,i}^4 b_{L,i}(x) + \langle T \rangle_{R,i}^4 b_{R,i}(x), \quad x \in (x_{i-1/2}, x_{i+1/2}) \quad (3.43)$$

where $T_{L,i} \equiv \langle T \rangle_{L,i}$ and $T_{L,i} \equiv \langle T \rangle_{L,i}$ for the lumping closure. There are analogous relations for $T(x)$ and $\phi^\pm(x)$ over the interior of each cell. These expressions are positive as long as the moments are positive. If the lagged, MC spatial closure produces an outflow from a cell that is negative, then these moments could become negative. It is important to note that the spatial closure will still have the same relation between the moments and the outflow; the lumping relation only affects the linear representation that the moments correspond to. For example in the L moment of the material energy (Eq. (3.22)), the lumped representation changes $2/3T_{L,i} + 1/3T_{R,i}$ to $T_{L,i}$, but no modifications are made to the absorption term $\sigma_{a,i}\langle\phi\rangle_{L,i}$; no modifications are made to the radiation terms in the radiation moment equations.

4. THE EXPONENTIALLY-CONVERGENT MONTE CARLO HIGH-ORDER SOLVER

The time-discretized transport equation to be solved by the HO solver is

$$\mu \frac{\partial I^{n+1,k+1/2}}{\partial x} + \left(\sigma_t^k + \frac{1}{c\Delta t} \right) I^{n+1,k+1/2} = \frac{\sigma_s}{2} \phi^{n+1,k} + \frac{1}{2} (\sigma_a^k acT^4)^{n+1,k} + \frac{\tilde{I}^n}{c\Delta t} \quad (4.1)$$

where the superscript k represents the outer HOLO iteration index. Here, $k + 1/2$ denotes the HO solve within outer HOLO iteration k , whereas k and $k + 1$ represent successive LO solves. The sources at k in Eq. (4.1) are estimated by the previous LO solution. Temperature-dependent cross sections are evaluated at $T^{n+1,k}$. As all sources on the right side of the equation are known, this defines a fixed-source, pure absorber transport problem. The above transport equation has the same form as a steady-state neutronics problem. We will solve this transport problem using the ECMC method.

Exponentially-convergent Monte Carlo (ECMC)[28, 6] provides an iterative algorithm that can efficiently reduce statistical noise to acceptable levels with significantly less particle histories than standard MC. In the remainder of this chapter, an overview of the ECMC solution method applied in this work is given. First, the LDFF trial space used by the ECMC algorithm is detailed. Then, the ECMC algorithm is developed, followed by more specific sampling and tracking details.

4.1 Implementation of LDFF x - μ Trial Space

To form the algorithm, a trial-space representation for the intensity is necessary. The ECMC solver uses a finite element representation in space and angle. On the interior of the cell with the i -th spatial index and j -th angular index, the linear

representation is defined as

$$\tilde{I}(x, \mu) = I_{a,ij} + \frac{2}{h_i} I_{x,ij} (x - x_i) + \frac{2}{h_j} I_{\mu,ij} (\mu - \mu_j), \quad (x, \mu) \in \mathcal{D}_{ij}, \quad (4.2)$$

where $\mathcal{D}_{ij} : x_{i-1/2} \leq x \leq x_{i+1/2} \times \mu_{j-1/2} \leq \mu \leq \mu_{j+1/2}$ is a rectangular cell in space and angle. The spatial cell width is h_i , the angular width is h_j , the center of the cell is (x_i, μ_j) , and

$$I_{a,ij} = \frac{1}{h_i h_j} \iint_{\mathcal{D}_{ij}} I(x, \mu) dx d\mu \quad (4.3)$$

$$I_{x,ij} = \frac{6}{h_i h_j} \iint_{\mathcal{D}_{ij}} \left(\frac{x - x_i}{h_i} \right) I(x, \mu) dx d\mu \quad (4.4)$$

$$I_{\mu,ij} = \frac{6}{h_i h_j} \iint_{\mathcal{D}_{ij}} \left(\frac{\mu - \mu_j}{h_j} \right) I(x, \mu) dx d\mu, \quad (4.5)$$

where I_a is the cell-averaged intensity, and I_μ and I_x define the first moment in μ and x of the intensity, respectively. The streaming term requires definition of $I(x, \mu)$ on faces. Standard upwinding in space is used to define $I(\mu)$ on incoming faces, e.g., for an unrefined mesh,

$$\tilde{I}_{ij}(x_{i-1/2}, \mu) = \begin{cases} I_{a,i-1,j} + I_{x,i-1,j} + \frac{2}{h_j} I_{\mu,i-1,j} (\mu - \mu_j) & 0 \leq \mu_{j-1/2} \leq \mu \leq \mu_{j+1/2} \\ I_{a,ij} - I_{x,ij} + \frac{2}{h_j} I_{\mu,ij} (\mu - \mu_j) & \mu_{j-1/2} \leq \mu \leq \mu_{j+1/2} \leq 0 \end{cases} \quad (4.6)$$

and

$$\tilde{I}_{ij}(x_{i+1/2}, \mu) = \begin{cases} I_{a,ij} + I_{x,ij} + \frac{2}{h_j} I_{\mu,ij} (\mu - \mu_j) & 0 \leq \mu_{j-1/2} \leq \mu \leq \mu_{j+1/2} \\ I_{a,i+1,j} - I_{x,i+1,j} + \frac{2}{h_j} I_{\mu,i+1,j} (\mu - \mu_j) & \mu_{j-1/2} \leq \mu \leq \mu_{j+1/2} \leq 0 \end{cases}, \quad (4.7)$$

for all i and j on the interior of the domain. For all simulations in this work, boundary conditions are provided as a specified isotropic intensity. Thus, the value of $I_{1j}(x_1/2, \mu)$ is a constant, for all j .

4.2 The ECMC Algorithm

The ECMC method is an iterative residual MC method. In operator notation, Eq. (4.1) can be written as

$$\mathbf{L}^k I^{n+1,k+1/2} = q^k \quad (4.8)$$

where $I^{n+1,k+1/2}$ is the transport solution of the angular intensity based on the k -th LO estimate of q^k . The linear operator \mathbf{L}^k is the *continuous* streaming plus removal operator, given by the left-hand side of Eq. (4.1), i.e.,

$$\mathbf{L}^k(\cdot) = \left[\mu \frac{\partial}{\partial x} + \left(\sigma_t^k + \frac{1}{c\Delta t} \right) \right] (\cdot) \quad (4.9)$$

We will use superscript (m) to indicated the m -th inner HO iteration. The LDFE representation of the m -th approximate solution to Eq. (4.8) is denoted $\tilde{I}^{n+1,(m)}(x, \mu)$. The associated residual is defined as $r^{(m)} = q - \mathbf{L}^k \tilde{I}^{n+1,(m)}$. Explicitly, the residual at iteration m is

$$\begin{aligned} r^{(m),k+1/2} = & \frac{\sigma_s}{2} \phi^{n+1,k} + \frac{1}{2} (\sigma_a a c T^4)^{n+1,k} + \frac{\tilde{I}^n}{c\Delta t} \\ & - \left(\mu \frac{\partial \tilde{I}^{n+1,k+1/2}}{\partial x} + \left(\sigma_t^k + \frac{1}{c\Delta t} \right) \tilde{I}^{n+1,k+1/2} \right)^{(m)} \end{aligned} \quad (4.10)$$

where the k terms have a LDFE representation in space on the coarsest mesh and are not recalculated at any point during the HO solve. The spatial derivative in the streaming term produces δ -functions due to the discontinuities in the trial space. The LDFE functional form of \tilde{I}^n is defined from the final HO solution of the previous time

step. The HOLO iteration indices are suppressed for the remainder of this chapter because the LO-estimated q^k and \mathbf{L}^k *remain constant for the entire HO solve*.

Addition of $\mathbf{L}I^{n+1} - q = 0$ to the Eq. (4.10), i.e., the residual equation, and manipulation of the result yields the error equation

$$\mathbf{L}(I^{n+1} - \tilde{I}^{n+1,(m)}) = \mathbf{L}\epsilon^{(m)} = r^{(m)} \quad (4.11)$$

where I^{n+1} is the exact solution¹ to the problem defined by Eq. (4.1) and $\epsilon^{(m)}$ is the true error in the approximate solution $\tilde{I}^{n+1,(m)}$. In the above equation, the incoming error is treated with a vacuum boundary condition. The residual source incorporates the incident intensity at boundaries through the face source. The \mathbf{L} operator in the above equation is inverted with the MC method, which statistically estimates an LDFE projection of the error in $\tilde{I}^{n+1,(m)}$, i.e.,

$$\tilde{\epsilon}^{(m)} = \mathbf{L}^{-1}r^{(m)} \quad (4.12)$$

where \mathbf{L}^{-1} is the Monte Carlo inversion of the streaming and removal operator. This inversion is strictly a standard Monte Carlo simulation; particle histories are tracked and the mean behavior estimated as in standard solutions to a Boltzmann transport equation [16, 17], although the source is complicated and produces both positive and negative statistical weights; sampling of the source is detailed in Sec. 4.3. It is noted that the exact error in $\tilde{I}^{n+1,(m)}$ (with respect to Eq. (4.1)) is being estimated with MC; tallies produce an integral projection of the error onto a LDFE space-angle trial space. Volumetric flux tallies over each space-angle element are required to estimate $\tilde{\epsilon}^{(m)}$, as detailed in Sec. 4.4. The space-angle moments of the error, preserved with

¹For clarity, in this chapter the exact solution is the exact solution to the transport problem defined by Eq. (4.1), not to the continuous equations that are trying to be solved.

the representation $\tilde{\epsilon}^{(m)}$, can be added to the moments of $\tilde{I}^{n+1}(m)$ to produce a more accurate solution.

The ECMC algorithm iterates on this process as follows:

1. Initialize the guess for $\tilde{I}^{n+1,(0)}$ to \tilde{I}^n or the projection of \tilde{I}^{n+1} from the latest HO solve
2. Compute $r^{(m)}$.
3. Perform a MC simulation to obtain $\tilde{\epsilon}^{(m)} = \mathbf{L}^{-1}r^{(m)}$ with a batch of N_b particle histories.
4. Compute a new estimate of the intensity $\tilde{I}^{n+1,(m+1)} = \tilde{I}^{n+1,(m)} + \tilde{\epsilon}^{(m)}$
5. Repeat steps 2 – 4 until desired convergence criteria is achieved.

Exponential convergence is obtained if the error ϵ is reduced each batch. With each batch, a better estimate of the solution is being used to compute the new residual, decreasing the magnitude of the MC residual source at each iteration m , relative to the solution I^{n+1} . The initial guess for the angular intensity $I^{n+1,(0)}$ is computed based on the previous solution for \tilde{I}^n . This is a critical step in the algorithm; it significantly reduces the required number of particles per time step because the intensity does not change drastically between time steps in optically-thick regions.

4.2.1 Projection and Statistical Accuracy of ECMC

Here, we emphasize the solution $\tilde{I}^{n+1,(m)}$ represents the LDFE projection of the exact Monte Carlo solution to the transport problem defined by Eq. (4.1). The discretization error is in q , i.e., the LD spatial representation of the emission and scattering source and the LDFE space-angle projection $\tilde{I}^n(x, \mu)$. The projection of the intensity is in general far more accurate than a standard finite element solution,

e.g., a S_N collocation method in angle. In typical IMC calculations, the average energy deposition within a cell is a projection that is computed with a standard path-length volumetric flux tally; the zeroth moment of the LDFF projection of ϵ is computed using an equivalent tally, preserving the zeroth moment of the true error.

To see why the true error is being estimated, it is important to note that \mathbf{L} in Eq. (4.11) is the continuous operator. The MC inverse \mathbf{L}^{-1} is a statistical solution method for an integral equation. The solution to this integral equation can be shown to provide the analytic inverse of the operator \mathbf{L} [16, 37]. Applying L^{-1} to Eq (4.11) and adding the result to the previous solution yields the desired moments of the exact solution:

$$\tilde{I}^{n+1,(m+1)} = \tilde{I}^{n+1,(m)} + \tilde{\epsilon}^{(m)} \quad (4.13)$$

$$\simeq \tilde{I}^{n+1,(m)} + \mathbf{L}^{-1} \left(q - \mathbf{L} \tilde{I}^{n+1,(m)} \right) \quad (4.14)$$

$$\simeq \mathbf{L}^{-1} q \quad (4.15)$$

where the above expression is equal in the limit of an infinite number of histories, within a single batch.

A MC batch provides a standard MC transport estimate of moments of the error. Each batch estimate of the moments of ϵ has a statistical uncertainty that, with sufficient sampling, is governed by the standard $1/\sqrt{N}$ convergence rate [16], for a particular source $r^{(m)}$, where N is the number of histories performed. If the statistical estimate of the projection $\tilde{\epsilon}$ is not sufficiently accurate, then the iterations would diverge. It is noted that there is statistical correlation across batches because $I^{n+1,(m+1)}$ and $\epsilon^{(m)}$ are correlated through $I^{n+1,(m)}$ and the MC source $r^{(m)}$. A general proof of exponential convergence for related adaptive MC transport methods is given in [38].

Because the intensity is saved between time steps, there is correlation that can not be easily measured. However, within a batch, the statistical uncertainty in moments of $\epsilon^{(m)}$ can be estimated with the sample variance of histories, using the standard sample-variance of MC mean estimators [16]. This provides a statistical estimate of moments of the solution estimated in that batch that asymptotically obey the central limit theorem [16], conditioned on the previous solution $I^{n+1,(m)}$. However, care must be taken with these statistical estimates, as they do not have the usual MC interpretation of confidence intervals because of correlations. Explicitly, if a particular simulation is repeated with independent sets of random numbers, the sample means will not (on average) correctly reproduce the confidence interval that the sample variance from the original simulation estimated. Additionally, the number of histories within each batch are likely too low for the central limit theorem to truly apply, as they do not sample the full solution space sufficiently [17].

Even for a fixed-source problem, the solution produced by the ECMC method only preserves global energy balance to the order of the magnitude of the residual. At the end of any batch, the continuous equation satisfied by the solution is

$$\frac{\partial \tilde{I}^{n+1}(x, \mu)}{\partial x} + \sigma_t \tilde{I}^{n+1} = q - r(x, \mu). \quad (4.16)$$

Integration of the residual over x and μ will generally produce a non-zero zeroth moment over each cell, due to the δ -function face sources and slope of the solution within a cell. Thus, integration over the domain will not produce the desired balance relation that would result if there was a zero residual. The magnitude of the zeroth moment of the residual provides some measure of how well balance is being preserved. However, it is noted that all of the energy created within a batch, through positive and negative weight particles, is being conserved correctly; all weight is

either absorbed or leaked from the system.

4.2.2 Adaptive Mesh Refinement

Because the exact angular intensity does not in general lie within the LDFE trial space, the iterative estimate of the error will eventually stagnate once the error cannot be sufficiently represented by a given FE mesh. An adaptive h -refinement algorithm has been implemented that can be used to allow the system to continue converging towards the exact solution [28, 6]. For TRT problems where absorption-reemission physics dominate, the diffusive and slowly varying regions of the problem require a less refined angular mesh to capture the solution than typical neutronics problems. However, greater spatial resolution is needed due to steep spatial gradients. Once error stagnation has occurred (and mesh refinement has reached a maximum level), additional histories can be performed with a fixed residual source to estimate the remaining error in the current solution. Although the remaining error will converge statistically at a standard $1/\sqrt{N}$ convergence rate, the remaining error will be much smaller than for a standard MC simulation, producing a much more efficient solution method overall.

Detailed equations for performing projections between meshes and computing the residual source on the refined meshes can be found in [28]. At the end of the ECMC batch, refinement is performed in space-angle cells based on a jump indicator. The jump indicator is the magnitude of the different between $I(x, \mu)$ in adjacent cells, averaged over each edge. The value of the largest jump, out of the four edges within a cell, is used as the indicator for that cell; alternatively, the error could directly be used as an indicator. Based on this indicator, a preset fraction of cells are refined based on the indicator. The refinement of a cell is chosen to be symmetric, with each space-angle cell divided into four equal-sized cells and only one refinement level

difference between adjacent cells is allowed, except for cells that share an edge across $\mu = 0$. The solution for $\tilde{I}^{n+1}(x, \mu)$ of the batch is projected onto the finer mesh for the next batch. Because the dimensionality of the sample space has increased, we increase the number of histories per batch such that the ratio of the number of histories to total cells is approximately constant for all meshes. At the end of the last HO solve in a time step, \tilde{I}^{n+1} is projected back onto the original, coarsest mesh and stored as \tilde{I}^n for the next time step.

4.2.3 *Negative Values for the Radiation Intensity*

For the HO solver, in cells with a steep gradient, the LDFE trial space can result in negative values of $\tilde{I}^{n+1}(x, \mu)$, similar to in the LO equations. In general, in such cells where the trial space cannot accurately represent the solution, error stagnation will rapidly occur. More sophisticated methods for resolving negative values are investigated in Chapter 7. However, because the residual formulation in ECMC allows for negative weight particles to occur, it is not strictly necessary to treat these cells specially during each MC batch. Instead, two simple fixups can be applied: unphysical angular consistency terms can be modified, or the LDFE projection of the intensity can be modified to be strictly positive at the end of the MC batch. To modify angular consistency terms, we determine if consistency terms lie in the appropriate half space at the end of the HO solve, an indication that the intensity was negative within that spatial cell. If any terms are non-physical, then they are replaced with the corresponding S_2 -equivalent value, i.e., $\mu^\pm = \pm 1/\sqrt{3}$. For the second fixup, we scale the slopes of the solution to produce a positive representation, as detailed in Sec. 7.1.

4.3 Systematic Sampling Algorithm for Residual Source

The LDFFE representation given by Eqs. (4.2), (4.6), and (4.7) is substituted into Eq. (4.10) and evaluated to produce the residual source for each ECMC batch. The MC source $r^{(m)}(x, \mu)$ in Eq. (4.12) consists of volumetric sources and face sources that are sampled. The face sources result from the spatial derivative applied to the discontinuities in the trial space, including a discontinuity at the boundaries for incoming directions [28]. The source can also produce positive and negative weight particles. The probability distribution function (PDF) for sampling particle coordinates is formed by dividing $r^{(m)}(x, \mu)$ by $\|r^{(m)}(x, \mu)\|_1$, i.e., the L_1 norm over space and angle of the residual. Particle coordinates (in x and μ) are sampled from the strictly positive PDF; then, if the residual is negative at the sampled coordinates, the weight of the particle history is negative. With the statistical weights of each particles normalized to unity, then the tallies must be multiplied by $\|r^{(m)}\|_1$ to produce the correct magnitude for moments of error. More details on specific equations for evaluating integrals of the residual for steady-state neutronics problems can be found in [28].

As a method to improve statistical efficiency within a batch, a modified version of the systematic sampling method [16] (a form of stratified sampling) was implemented for determining the number of histories sampled from each space-angle cell. In the systematic sampling algorithm, the number of particle histories sampled in each space-angle cell is predetermined and proportional to the integral of the PDF over that cell. The goal is to effectively distribute particle histories to regions of importance, but to sample a preset, minimum number of histories N_{\min} in less probable regions; this is to limit bad statistics in low probability cells (this is primarily important for adaptively refined meshes). However, there is no need to sample his-

tories from regions in thermal equilibrium, where the probability of a particle being born is on the order of roundoff. In most of the simulations performed for this work $N_{\min} = 1$; this choice is made to keep the total number of histories per time step constant throughout the simulation for comparison to IMC.

The unmodified probability of a particle being born in cell ij is

$$p_{ij} = \frac{\|r^{(m)}\|_{1,ij}}{\|r^{(m)}\|_1} \quad (4.17)$$

where $\|r\|_{1,ij}$ is the L_1 norm over cell ij , including the upwind face and interior volumetric source. Thus, the number of particles in cell ij is

$$N_{ij} = \begin{cases} \lfloor (N_b p_{ij}) \rfloor & N_b p_{ij} > N_{\min} \\ 0 & p_{ij} < O(\epsilon_{prec}) \\ N_{\min} & \text{else} \end{cases} \quad (4.18)$$

where N_{\min} is the minimum number of histories in significant cells, N_b is the total number of histories sampled that batch, and ϵ_{prec} is on the order of double precision. Particle weights must be adjusted to account for the difference between the number sampled from a particular cell and the original probability of that element being sampled. This rounding requires some additional histories needing to be sampled, or removed, to reach a specific number of histories. These modifications are made to the most probable cell

The algorithm for sampling each of the N_{ij} starting histories, from each ij element, is

1. Sample random number $\eta \sim U(0, 1)$

(a) If $\eta < \|r_{\text{face}}^{(m)}\|_{1,ij} / \|r^{(m)}\|_{1,ij}$:

- Sample (x, μ) from $\bar{r}_{ij,\text{face}}$ face source with rejection sampling

(b) Else:

- Sample (x, μ) from $\bar{r}_{ij,\text{int}}$ volumetric source using rejection sampling

2. Set particle weight to $p_{ij}N_b/N_{ij}$

where $\bar{r}_{i,\text{face}}$ and $\bar{r}_{i,\text{int}}$ are the upwind face and interior residual in cell ij .

The residual gives a good indication of where histories are most likely to contribute to the error, particularly in optically thick cells where particles do not transport long distances. Systematic sampling is a variance reduction technique that reduces the variance of the function, i.e., the residual, being sampled [16]. Thus, we expect variance to be reduced by more efficiently sampling the residual in optically thick cells. In thin cells, where particles transport farther, this sampling procedure does not guarantee less variance overall.

4.4 Continuous Weight Deposition Tallies

During a MC batch, moments of the error are tallied. The necessary moments of the error are defined analogously to Eq.'s (4.3)–(4.5). The tallies are evaluated by weighting the particle density with the appropriate basis function and integrating along the history path through the cell. The LDFE representation results in local tallies where only particles entering a particular cell contribute to that cell's estimators. For the cell average, the n -th particle that enters the cell ij makes the contribution, or *score*,

$$\epsilon_{a,ij}^n = \frac{1}{h_i h_j} \int_{s_o^n}^{s_f^n} w^n(x, \mu) ds, \quad (4.19)$$

where s_o^n and s_f^n are the beginning and end of the n -th particle track in the cell and $w(x, \mu)$ is the weight of the error particle in the MC simulation.

As in [5], because we are solving a pure absorber problem with Monte Carlo, we will allow particles to stream without absorption to reduce statistical variance in the tallies. The weight of particles is reduced deterministically along the path as they stream, with no need to sample a path length. Histories are allowed to stream in this manner for 6 mean free paths (MFP) before switching to analog path length sampling; this limits the tracking of very small weight histories. The choice of 6 MFP allows particles to continuously deposit weight until they reach 0.25% of their original weight. Path lengths are tracked in terms of MFP, so there is no need to re-sample at material interfaces.

Weight is attenuated exponentially, i.e., $w(x, \mu) \propto \exp(-\sigma_t^{\text{eff}}|x/\mu|)$, where for the time-discretized equations $\sigma_t^{\text{eff}} = \sigma_t + 1/(c\Delta t)$. Substitution of the weight representation into Eq. (4.19) produces the result

$$\epsilon_{a,ij}^n = \frac{w(x_0, \mu)}{\sigma_t^{\text{eff}} h_i h_j} \left(1 - e^{-\sigma_t^{\text{eff}} s^n}\right). \quad (4.20)$$

Here, $w(x_0, \mu)$ is statistical weight of the particle at the start of the path and s^n is the length of the track. The contribution of a particle track to ϵ_x is given by

$$\epsilon_{x,ij}^n = \frac{w(x_0, \mu)}{h_i^2 h_j \sigma_t^{\text{eff}}} \left[x_0 - x_f e^{-\sigma_t^{\text{eff}} s^n} + \left(\frac{\mu}{\sigma_t^{\text{eff}}} - x_i \right) \left(1 - e^{-\sigma_t^{\text{eff}} s^n}\right) \right], \quad (4.21)$$

where x_0 and x_f are the beginning and ending x coordinates of the n -th path. The contribution to the first moment in μ is

$$\epsilon_{\mu,ij}^n = \frac{w(x_0, \mu)}{h_j^2 h_i \sigma_t^{\text{eff}}} (\mu - \mu_j) \left(1 - e^{-\sigma_t^{\text{eff}} s^n}\right), \quad (4.22)$$

where the particle x -direction cosine μ does not change, because it is a pure-absorber simulation. The unbiased estimators for the moments of the error, e.g., $\hat{\epsilon}_{a,ij}$, are

simply the average score from all histories:

$$\hat{\epsilon}_{a,ij}^{(m)} = \frac{1}{N_b} \sum_{n=1}^{N_b} \epsilon_{a,ij}^n \quad (4.23)$$

where N_b is the number of particle histories performed within that batch.

4.4.1 Face Tallies and Correction Near $\mu = 0$

Face-averaged estimators of $\epsilon(x, \mu)$ are required to compute the outflow for estimating the spatial closure discussed in Sec. 3.6. The standard face-based tallies [16, 39] are used. Tallies are weighted by the appropriate basis functions to compute a linear FE projection in μ at each face. The tally score, for the angular-averaged error $\epsilon_{a,i}$ is defined as

$$\hat{\epsilon}_{a,i\pm 1/2,j} = \frac{1}{N} \sum_{m=1}^{N_{i\pm 1/2,j}} \frac{w_m(x_{i\pm 1/2}, \mu)}{h_\mu |\mu|}, \quad (4.24)$$

where N is the number of histories performed and $N_{i\pm 1/2,j}$ is the number of histories that crossed the surface $i \pm 1/2$, in the j angular element. For the first moment, the tally is

$$\hat{\epsilon}_{\mu,i\pm 1/2,j} = \frac{1}{N} \sum_{m=1}^{N_{i\pm 1/2,j}} 6 \left(\frac{\mu - \mu_j}{h_\mu} \right) \frac{w_m(x_{i\pm 1/2}, \mu)}{|\mu| h_\mu}. \quad (4.25)$$

For positive and negative directions, solutions are only tallied on the $x_{i+1/2}$ and $x_{i-1/2}$ faces, respectively. Particles are only tallied after leaving a cell, and, as discussed in Section 4.5, particles born on a surface do not contribute to the tally of that surface.

Near $\mu = 0$, particles can contribute large scores to the zeroth angular moment that lead to large and unbounded variances [39]. To avoid large variances, we have applied the standard fixup [17, 39]. For $|\mu|$ below some small value μ_{cut} , particles contribute the expected score over the range $(0, |\mu_{cut}|)$ for an approximate isotropic

particle density. Thus, scores in this range have no variance, but are biased for non-isotropic intensities. For all results in this work $\mu_{cut} = 0.01$. Assuming an isotropic particle density I_0 , the average of $1/\mu$, for positive μ , is

$$\overline{1/\mu} = \frac{\int_0^{\mu_{cut}} \frac{1}{\mu} I_0 d\mu}{\int_0^{\mu_{cut}} I_0 d\mu} = \frac{2}{\mu_{cut}}. \quad (4.26)$$

For negative μ , $\overline{1/\mu} = -2/\mu_{cut}$. All particles in the range $(0, |\mu_{cut}|)$ contribute the expected score by evaluating the appropriate estimator at $\pm\mu = \pm 2/\mu_{cut}$. It is noted that the first angular moment would be well behaved, but it is inconsistent to only modify the zeroth moment in the I_μ estimators. Additionally, assuming an isotropic intensity near $\mu = 0$ helps to limit the first μ moment, where the LD trial space often cannot resolve the solution anyway.

4.5 ECMC Solution with Linear Doubly-Discontinuous FE Trial Space

In this section, the treatment of the spatial variable for the ECMC method is extended to a linear, doubly-discontinuous (LDD) trial space. This extension is necessary for computing the HO spatial closure for the LO equations discussed in Sec. 3.6. To incorporate a projection of the MC solution at faces, a second discontinuity is introduced into the trial space. A projection of the intensity that is separate from the linearly-extrapolated outflows allows for an angular LD projection of the MC solution at faces. This solution is incorporated into the LO solution through the HO spatial closure of the LO equations. Additionally, the independent solution at faces allows for face-averaged consistency terms (e.g., Eq. (3.15)) to be directly evaluated.

The LDD trial space is demonstrated for the x variable in Fig. 3.3. For the HO solver, the LDD trial space is the same as the LDFE space-angle trial space, except

for an extra discontinuity in space at the outflow face. The solution at faces is linear in angle over the angular width of each x - μ cell. The LDD representation for cell ij is

$$\tilde{I}_{ij}(x, \mu) = \begin{cases} I_{a,i-1/2,j} + \frac{2}{h_j} I_{\mu,i-1/2,j} (\mu - \mu_j) & x = x_{i-1/2} \\ I_{a,ij} + \frac{2}{h_i} I_{x,ij} (x - x_i) + \frac{2}{h_j} I_{\mu,ij} (\mu - \mu_j) & x_{i-1/2} < x < x_{i+1/2} \\ I_{a,i+1/2,j} + \frac{2}{h_j} I_{\mu,i+1/2,j} (\mu - \mu_j) & x = x_{i+1/2} \end{cases}, \quad (4.27)$$

for $\mu_{j-1/2} \leq \mu \leq \mu_{j+1/2}$. The face-tallied quantities $I_{a,i\pm 1/2}$ and $I_{\mu,i\pm 1/2}$ are shared between adjacent cells, so the expression is the same for positive and negative μ . The linear representation at faces preserves all angular moments of the intensity needed for the spatial closure and face-averaged consistency terms.

The residual source and process of estimating moments of the error on the interior of space-angle cells is unchanged. The process of estimating the solution on the outgoing face requires tallying the error when particles leave a cell, using the face-averaged tallies discussed in Section 4.4.1. Face-averaged consistency terms are directly evaluated using $\tilde{I}(x_{i+1/2}, \mu)$ evaluated at the face of each coarse mesh cell. Particularly near $\mu = 0$, the linear representation in μ can be driven negative. In such cells, we scale the slope in μ so that the solution is positive.

The inclusion of the outflow discontinuity in space has a minimal effect on the treatment of the residual source. Applying L to the LDD intensity given by Eq. (4.27), results in two δ functions at each interior face. For *positive flow*, at a face $x_{i+1/2}$, the face portion of the residual is defined as

$$r_{\text{face}}(x_{i+1/2}) = -\mu \frac{\partial \tilde{I}^{(m)}}{\partial x} \Big|_{x=x_{i+1/2}} \quad (4.28)$$

$$= r_{\text{face}}(x_{i+1/2}^-) \delta^-(x - x_{i+1/2}) + r_{\text{face}}(x_{i+1/2}^+) \delta^+(x - x_{i+1/2}) \quad (4.29)$$

where

$$r_{\text{face}}(x_{i+1/2}^-) = -\mu \left(\tilde{I}^{(m)}(x_{i+1/2}, \mu) - \tilde{I}^{(m)}(x_{i+1/2}^-, \mu) \right) \quad (4.30)$$

$$r_{\text{face}}(x_{i+1/2}^+) = -\mu \left(\tilde{I}^{(m)}(x_{i+1/2}^+, \mu) - \tilde{I}^{(m)}(x_{i+1/2}, \mu) \right). \quad (4.31)$$

Here, $I^{(m)}(x_{i+1/2}, \mu)$ is the face-estimated solution at $x_{i+1/2}$ and $I^{(m)}(x_{i+1/2}^+)$ and $I^{(m)}(x_{i+1/2}^-)$ are the LDFE solution *extrapolated* to $x_{i+1/2}$ from the x cell $i+1$ and cell i , respectively; all three terms are linear in μ over $\mu_{j-1/2} \leq \mu \leq \mu_{j+1/2}$. Particles sampled from the two δ -functions have the same starting location. The only difference is, for positive μ , only the particles sampled from $r_{\text{face}}(x_{i+1/2}^-)$ will contribute to the face tally at $x_{i+1/2}$; the opposite is true for negative μ .

To reduce variance, we do not sample the two δ functions independently. Instead, the two δ -functions are combined into a single face source in each element², and particles do *not* score at the face from which they are sampled. To account for the un-tallied error, we add the analytic contribution to $\epsilon_{i+1/2}$ from $r_{\text{face}}(x_{i+1/2}^-)$, at the end of each batch. This analytic contribution to the error at faces is derived in Sec. B.1. The update for $I(x_{i+1/2}, \mu)$ becomes

$$\tilde{I}^{(m+1)}(x_{i+1/2}, \mu) = \tilde{I}^{(m)}(x_{i+1/2}^-, \mu) + \epsilon^{(m)}(x_{i+1/2}, \mu) \quad \mu > 0 \quad (4.32)$$

$$\tilde{I}^{(m+1)}(x_{i+1/2}, \mu) = \tilde{I}^{(m)}(x_{i+1/2}^+, \mu) + \epsilon^{(m)}(x_{i+1/2}, \mu) \quad \mu < 0 \quad (4.33)$$

This result has the serendipitous effect that the estimation of the solution on a face depends only on the previous interior solutions $\tilde{I}^{(m)}(x_{i+1/2}^-, \mu)$ and $\tilde{I}^{(m)}(x_{i+1/2}^+, \mu)$ and not the previous face value $\tilde{I}^{(m)}(x_{i+1/2}, \mu)$. This has an additional benefit that the face values can be estimated at any chosen batch, in particular cells. For this work,

²The combination of the two δ -functions produces the same residual source as the original LD trial-space residual.

the solution is estimated in all cells with the LDD trial space.

5. COMPUTATIONAL RESULTS

In this chapter, we compare results of the time-discretized HOLO method to IMC with a source tilting algorithm for two test problems [40]. Also, we briefly compare performance in Section 5.4. For all IMC results, no local, discrete diffusion acceleration methods for effective scattering (e.g., those in [19, 20]) were applied. Additionally, we demonstrate the efficiency advantage of ECMC in our HOLO algorithm by comparing the results to the same HOLO algorithm with the ECMC algorithm replaced with a standard Monte Carlo (SMC) simulation. Finally, we present results that demonstrate preservation of the equilibrium diffusion limit and the discrete maximum principle by the HOLO algorithm. Some of the results in this section were published previously in [2].

5.1 Metrics of Accuracy and Statistical Efficiency

Several different metrics were used to quantify results throughout this chapter as appropriate. A measure of variance in cell-averaged mean intensities was calculated to provide a quantitative measure of the statistical accuracy of different solution methods. To form the sample standard deviations, N_{sim} independent simulations for each particular result were performed, using unique random number generator seeds. Unless otherwise indicated, $N_{sim} = 20$. The sample variance of a particular cell-averaged $\phi(x)$ is

$$S_i^2 = \frac{1}{N_{sim} - 1} \sum_{l=1}^{N_{sim}} \left(\overline{\phi}_i - \phi_i^{(l)} \right)^2, \quad (5.1)$$

where $\phi_i^{(l)}$ is the cell-averaged scalar intensity for cell i from the (l) -th of N_{sim} independent simulations and $\overline{\phi}_i$ is the corresponding sample mean from the N_{sim} simulations. To provide a normalized, spatially-integrated result, we form a norm over

cells as

$$\|s\|_{a,rel} = \left(\frac{\sum_{i=1}^{N_c} S_i^2}{\sum_{i=1}^{N_c} \phi_i^2} \right)^{1/2}, \quad (5.2)$$

where N_c is the number of spatial cells.

We will also form a figure of merit (FOM) to demonstrate how statistical accuracy scales with the number of histories performed. Our FOM is defined as

$$\text{FOM} = \frac{1}{N_{\text{tot}} \|s\|_{a,rel}^2} \quad (5.3)$$

where N_{tot} is the total number of histories performed over the simulation. A larger value of the FOM indicates that the method produced less variance in the solution per history performed, for a given problem. This form of the FOM is typically chosen because the variance is expected to reduce inversely proportional to N_{tot} , so for standard MC simulations the FOM becomes, on average, independent of N_{tot} [16]. The FOM is not necessarily expected to be independent of N_{tot} for IMC or our HOLO method due to correlation of the solution between time steps; additionally, ECMC has correlations between batches.

The consistency between HO and LO solutions and the accuracy as compared to a reference solution were computed for some simulations. The consistency for the (l) -th particular simulation is measured with the relative L_2 norm of the difference between the projected HO and LO solutions, i.e.,

$$\|\phi_{HO} - \phi_{LO}\|_{2,rel}^{(l)} = \frac{\sqrt{\int_0^X \left(\phi_{HO}^{n+1,(l)}(x) - \phi_{LO}^{n+1,(l)}(x) \right)^2 dx}}{\sqrt{\int_0^X \left(\phi_{LO}^{n+1,(l)}(x) \right)^2 dx}} \quad (5.4)$$

where $\phi_{LO}(x)$ and $\phi_{HO}(x)$ are the LDFF representations in space of the intensity from the HO and LO solvers, from the end of the last time step. The error between a reference solution, e.g., a fine mesh solution, and the l -th simulation is computed as

$$\|e\|_{2,rel}^{(l)} = \frac{\|\phi_{LO}^{n+1,(l)}(x) - \phi_{LO}^{n+1,ref}(x)\|_2}{\|\phi_{LO}^{n+1,ref}(x)\|_2} \quad (5.5)$$

All L_2 norms were computed using quadrature over the finest spatial mesh. An integrated measure of the error in cell-averaged mean intensities on the mesh of the l -th simulation, with $N_c^{(l)}$ spatial cells, is computed as

$$\|e\|_{a,rel}^{(l)} = \left(\frac{\sum_{i=1}^{N_c^{(l)}} \left(\phi_i^{n+1,(l)} - \phi_i^{n+1,ref} \right)^2}{\sum_{i=1}^{N_c^{(l)}} \left(\phi_i^{n+1,ref} \right)^2} \right)^{1/2}, \quad (5.6)$$

where $\phi_i^{n+1,ref}$ is computed by spatially averaging the reference solution over the i -th coarse spatial cell, with the assumption of uniform mesh spacing.

Because the method is stochastic, it is necessary to approximately estimate the average error of each metric. The sample mean of each of the above norms is estimated based on N_{sim} independent simulations; the sample standard deviation for the *sample mean of each quantity* is also reported, e.g.,

$$s \left(\|e\|_{2,rel}^{(l)} \right) = \frac{1}{\sqrt{N_{sim}}} \left[\frac{1}{N_{sim} - 1} \sum_{l=1}^{N_{sim}} \left(\|e\|_{2,rel}^{(l)} - \|e\|_{2,rel} \right)^2 \right]^{1/2}, \quad (5.7)$$

where

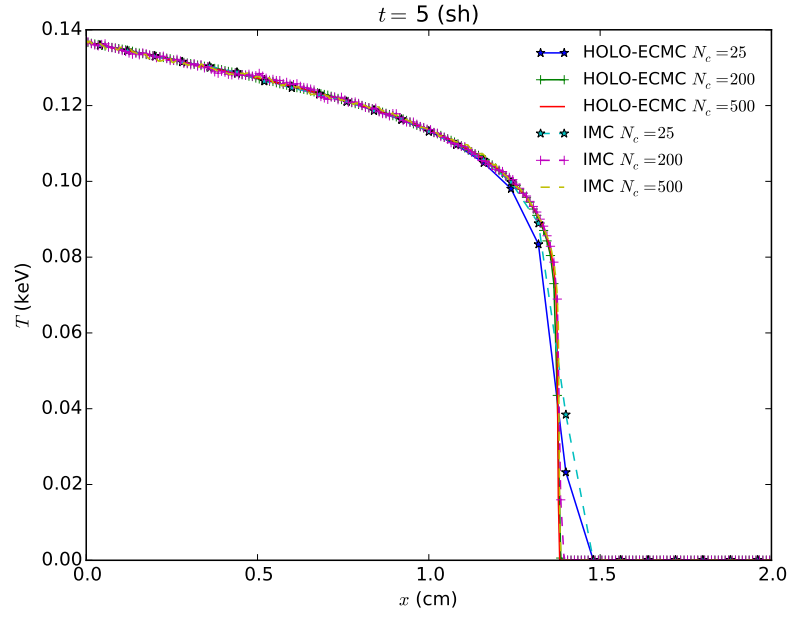
$$\|e\|_{2,rel} = \frac{1}{N_{sim}} \sum_{l=1}^{N_{sim}} \|e\|_{2,rel}^{(l)} \quad (5.8)$$

is the corresponding sample mean.

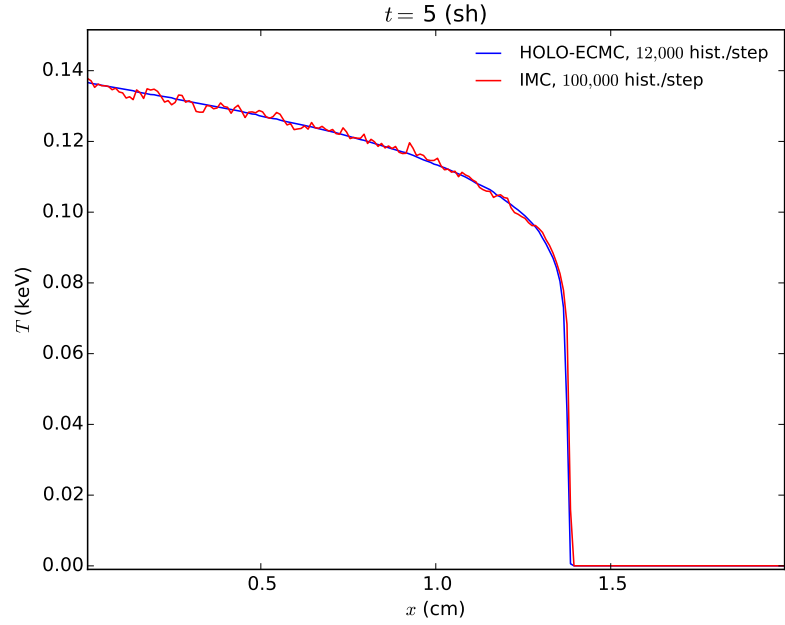
5.2 Marshak Wave

For the first problem, the radiation and material energies are initially in equilibrium at 2.5×10^{-5} keV. An isotropic incident intensity of 0.150 keV is applied at $x = 0$; the incident intensity on the right boundary is 2.5×10^{-5} keV. The material properties are $\rho = 1$ g cm $^{-3}$ and $c_v = 0.013784$ jks/keV-g. The absorption cross section varies as $\sigma(T) = 0.001 \rho T^{-3}$ (cm $^{-1}$), for T in keV. The simulation was advanced until $t = 5$ sh (1 sh $\equiv 10^{-8}$ s) with a fixed time step size of 0.001 sh. For comparison purposes, we have not used adaptive mesh refinement, only performed one HOLO iteration per time step, and use a fixed 3 HO batches with equal number of histories per batch. A relative tolerance of 10^{-6} for the change in $\phi(x)$ and $T(x)$ was used for the LO newton solver for all results. Radiation energy distributions are plotted as an effective temperature given by $T_r = (\phi/(ac))^{0.25}$. The effective temperature represents the temperature of the material, if the material and temperature were in equilibrium. Cell-averaged quantities are plotted. For this problem, when negative values for $\phi^{n+1,\pm}(x)$ were detected, the lumping-equivalent discretization was used within those cells and that Newton step was repeated. Non-physical angular consistency terms were replaced with S $_2$ -equivalent terms. For reference, the fixup in Sec. 3.5 that strictly enforces the floor temperature and preserves half-range balance produced similar accuracy and stably converged for this problem.

Figure 5.1a on page 65 depicts the cell-averaged radiation temperatures for the IMC and HOLO method with ECMC, for various number of spatial mesh cells N_c ; we have used HOLO-ECMC to denote our algorithm because later results will use different HO solvers. For all IMC calculations, $n = 10^5$ histories per time step were used. For the HOLO method, we have used 4 equal-sized cells in μ for the finite-element angular mesh used by the ECMC solver. The spatial grid is the same for



(a) Convergence of IMC and HOLO-ECMC solutions.



(b) Comparison of solutions for 200 spatial cells.

Figure 5.1: Comparison of radiation temperatures for Marshak wave problem at $t = 5$ sh.

the HO and LO solvers. For the cases of $N_c = 25$ and $N_c = 200$, 4,000 histories per batch (12,000 per time step) were used. For $N_c = 500$, 16,000 histories per time step were used due to the increased number of space-angle cells that need to be sampled. The IMC and HOLO solutions agree as the mesh is converged. There is similar agreement in the location of the wavefront due to the linear shape of the emission source over a cell. The cells nearest the wavefront required use of the lumping-equivalent discretization of the radiation and S_2 equivalent terms during the LO solve, resulting in strictly positive cell-averaged quantities.

A comparison of the solutions for the case of 200 cells is given in Figure 5.1b. For the IMC solution 10^5 histories per time step were simulated; for the HOLO method only 4,000 histories per batch (12,000 per time step) were simulated. There is significant statistical noise in the IMC solution compared to the HOLO solution. The HOLO solution visually demonstrates no statistical noise. Because the ECMC solve is only determining the change over the time step, the statistical noise in the result is small relative to the magnitude of I^{n+1} . Also, the source sampling only places particles in cells where the residual is large. No particles are sampled in the equilibrium region out front of the wave. Only a few angular cells are necessary to accurately reproduce the mean intensity for this problem.

Comparisons of $\|s\|_{a,rel}$ and the FOM for IMC and the HOLO method are given in Table 5.1, for different numbers of histories per time step. The FOM results are normalized to the value for IMC with $n = 12,000$. The HOLO method demonstrates less variance for the same numbers of histories, producing FOM values that are two orders of magnitude greater than for IMC. Where as the FOM remains relatively constant for IMC, as n is increased the FOM improves for the HOLO method. This is a result of each batch producing more statistically accurate estimates of the error ϵ , which results in an increased convergence rate of ϵ overall.

Table 5.1: Comparison of sample statistics for the Marshak Wave problem. Simulation end time is $t = 5$ sh.

	$\ s\ _{a,rel}$		FOM	
hists./step	IMC	HOLO-ECMC	IMC	HOLO-ECMC
12,000	3.40%	0.28%	1	145
100,000	1.22%	0.057%	0.93	422

5.3 Two Material Problem

This problem consists of an optically thin (left) and an optically thick (right) material region, with temperature-independent cross sections. The material properties are given in Table 5.2. Initially the radiation and material energies are in equilibrium at a temperature of 0.05 keV. An isotropic incident intensity of 0.500 keV is applied at $x = 0$ at $t = 0$; the isotropic incident intensity on the right boundary is 0.05 keV. The simulation end time is 5 sh. For all HOLO simulations, we have used 8 equal-sized mesh cells in μ . As for the Marshak problem, the cells nearest the wavefront required use of the lumping-equivalent discretization and S_2 -equivalent angular consistency terms during the LO solve.

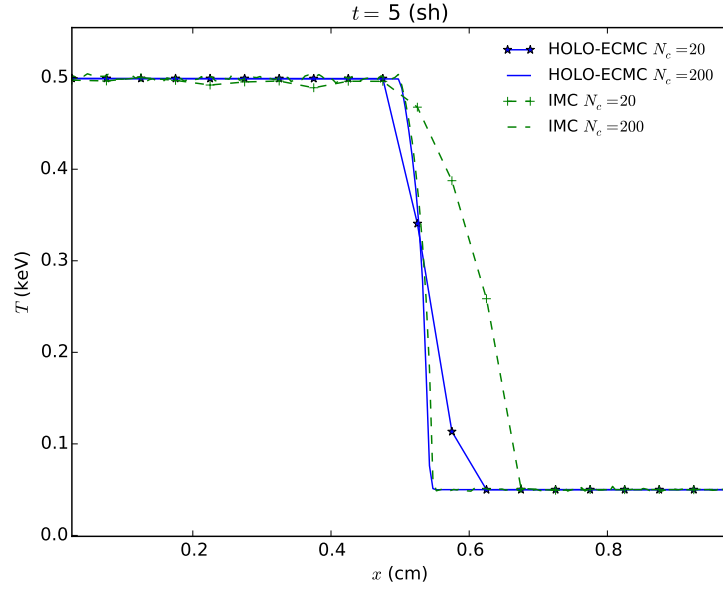
Table 5.2: Material properties for two material problem.

	$x \in [0, 0.5)$ cm	$x \in [0.5, 1.0]$ cm
σ_a (cm ⁻¹)	0.2	2000
ρ (g cm ⁻³)	0.01	10.0
c_v (jks/keV-g)	0.1	0.1

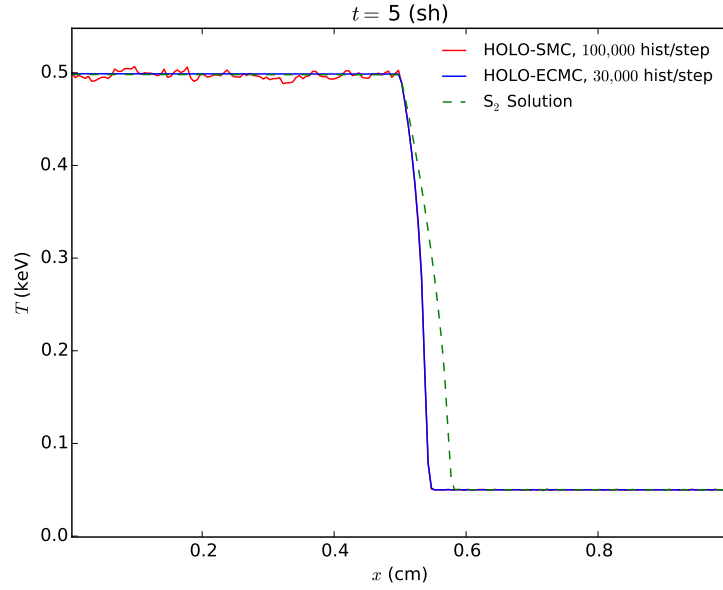
Fig. 5.2a depicts the HOLO and IMC radiation temperatures at the end of the simulation. The IMC and HOLO results show good agreement over the finer mesh. On the coarse mesh ($N_c = 20$), the LDFE representation of T^4 in the HOLO method predicts the location of the wavefront more accurately than the IMC method with source tilting.

The results in Fig. 5.2b demonstrate the benefit of ECMC as a HO solver compared to standard MC. The HOLO algorithm with the ECMC HO solver (HOLO-ECMC) results are for running 3 batches of 10,000 histories, per time step. The solution for the HOLO method with a standard MC solver as the HO solver (HOLO-SMC) with standard source sampling uses 10^5 histories per time step. The HOLO-SMC solution demonstrates significant statistical noise. This noise is introduced into the LO solver by bad statistics in computing the consistency terms. Also plotted is an S_2 solution obtained with consistency terms that are equivalent to S_2 and no HO correction. The S_2 solution results in an artificially fast wavefront, as expected, demonstrating the necessity of HO correction in this problem.

Table 5.3 gives the FOM and $\|s\|_{a,rel}$ for IMC and the HOLO-ECMC method. The FOM values are normalized to the value for IMC with $n = 30,000$. The end time was reduced to 2 sh for these results to reduce computational times. The reduction in variance by the HOLO method over IMC is substantial. The improvement of the FOM for the HOLO method compared to IMC is greater than for the Marshak wave problem. This improvement is because the wave moves much slower in right region of this problem, due to the large, constant cross section. Also, in the optically thin region of the problem the solution quickly comes to equilibrium. Thus, the ECMC algorithm has to estimate a very small change in the intensity over a time step.



(a) Comparison of IMC and HOLO-ECMC.



(b) Comparison of SMC and ECMC HO solvers.

Figure 5.2: Comparison of radiation temperatures for two material problem.

Table 5.3: Comparison of sample statistics for the two material problem for 200 x cells. Simulation end time is $t = 2$ sh.

	$\ s\ _{a,rel}$		s_{\max}	
hists./step	IMC	HOLO-ECMC	IMC	HOLO-ECMC
30,000	3.63%	0.01%	1	104,000
100,000	1.96%	0.003%	1.03	360,000

5.4 Performance Comparison of IMC and HOLO-ECMC

We have measured the total CPU time for simulations to provide a simplified measure of the computational cost. These results compare how computational times change for the two different problems and how the methods scale with time step size and particle histories. Absolute comparisons in the computational cost of the two methods cannot be made, because the methods are implemented in different code infrastructures. Additionally, the HOLO method fully resolves non-linearities at each time step, whereas IMC is using a single linearized step with lagged cross sections. Simulations were performed on the same processor, using a single CPU core. Reported times are the average of 10 runs and all results used 200 x cells, $\Delta t = 0.001$ sh, and an end time of $t = 2$ sh.

The average simulation time per history performed for the Marshak wave problem is given in Table 5.4. The average time per history is computed by dividing the total simulation time by the total number of histories performed (e.g., the time of the LO solves is included for the HOLO method). Results are given for different numbers of histories per time step, as well as a case with an increased time step size. The table also includes the number of LO iterations performed per LO solve for the HOLO method, averaged over all time steps; there are two LO solves per time step. The

same results are reported for the two material problem in Table 5.5.

The HOLO method does not scale with the number of histories due to the fixed cost of the LO solver. The cost of the LO solver is more significant at the lower history counts compared to the case of 10^5 histories, for both problems. There is a slight increase in the number of newton iterations as the time step is increased, but the average cost per history is not significantly increased. Similar to the results in [5], as the time step size is increased to 0.005 sh, the IMC method increases in cost per time step, due to an increase in effective scattering events, particularly for the two material problem. Because the cross sections in the two material problem do not have a T^{-3} behavior, the cost of the effective scattering cross section in IMC is more apparent, resulting in longer simulation times.

Table 5.4: Comparison of average CPU times per history and LO iteration counts for the Marshak Wave problem.

hists./step	$\Delta t(sh)$	IMC ($\mu s/hist.$)	HOLO ($\mu s/hist$)	Newton iters./LO solve
100,000	0.001	10	5.3	3.8
12,000	0.001	9.7	8.1	4.1
12,000	0.005	19	9.4	6.2

Table 5.5: Average CPU times per history and LO iteration counts required for the two material problem.

hists./step	$\Delta t(sh)$	IMC ($\mu s/hist.$)	HOLO ($\mu s/hist$)	Newton iters./LO Solve
100,000	0.001	17	3.5	4.9
30,000	0.001	18	6.9	5.0
30,000	0.005	59	7.4	7.6

5.5 Comparison of Different HO Solvers

In this section we compare the results of our HOLO algorithm with different HO solvers for the test problems in Section 5.2 and 5.3. We compare standard MC (SMC) as a HO solver to the HOLO algorithm with ECMC using both three batches and a single batch, per time step. The use of a single batch is similar to the approach in [1]. Results are tabulated for 200 x cells, using the same total number of histories per time step, divided evenly among the batches.

Tables 5.6 and 5.7 depict the results for the Marshak wave and two material problems. The number of batches for each ECMC case is indicated in parenthesis. The FOM values are normalized to the reference IMC result for the corresponding problem. For HOLO-SMC there is minimal reduction in variance compared to IMC in the Marshak wave problem, and the two material problem actually demonstrates worse variance. Sufficient histories are not performed to accurately estimate consistency terms throughout the problem. For ECMC, a single batch produces less variance than the case of three equal batches. This indicates that if the solution cannot be resolved with the trial space (i.e., the intensity is driven negative), a single large batch may be more accurate. It is noted that these results only estimate statistical variance and do not strictly account for accuracy.

Table 5.6: Comparison of sample statistics for the Marshak Wave problem. Number of ECMC batches is indicated in parenthesis.

hists./step	$\ s\ _{a,rel}$			FOM		
	SMC	ECMC (1)	ECMC (3)	SMC	ECMC (1)	ECMC (3)
12,000	2.77%	0.10%	0.28%	1.50	1280	145
100,000	0.98%	0.03%	0.06%	1.43	1270	422

Table 5.7: Comparison of sample standard deviations for the two material problem. Number of ECMC batches is indicated in parenthesis.

	$\ s\ _{a,rel}$			FOM		
hists./step	SMC	ECMC (1)	ECMC (3)	SMC	ECMC (1)	ECMC (3)
30,000	5.35%	0.002953%	0.011%	0.46	1.51×10^6	1.04×10^4
100,000	2.85%	0.001474%	0.0033%	0.49	1.80×10^6	3.59×10^4

5.6 Pre-heated Marshak Wave Problem and Adaptive Mesh Refinement

Finally, to demonstrate the potential of ECMC with adaptive space-angle mesh refinement, we compare results for a modified Marshak wave problem. The problem parameters are chosen such that the LDFE trial space can accurately represent the solution (i.e., the intensity is slowly varying in space). Mesh refinement is of minimal use in the previous problems due to most of the unresolvable error existing at the wavefronts, caused by the large cross sections. The modified problem has the same material properties and left boundary source as the Marshak wave problem in Section 5.2. However, the initial equilibrium temperature and right boundary condition are raised to 0.03 keV. The higher initial temperature reduces the initial cross section and increases the strength of the emission source within cells. The LDFE mesh can now sufficiently resolve the solution and lumping is not required by the LO solution. The simulation end time is 0.5 sh with a constant time step of $\Delta t = 0.001$ sh.

The result from HOLO-ECMC with three batches and IMC are compared in Fig. 5.3. It was found that 100 x cells was sufficient to resolve the solution spatially. There is slightly more noise in IMC past the wavefront due to the increased emission source. Additionally, the cross section is thin enough that some photon energy is able to reach the right boundary, in front of the wavefront.

A comparison of the variances for this problem, for the various HO solvers, is given in Table 5.8. The FOM values are normalized to the case of HOLO-SMC with 12,000 histories per time step. The final row of the table is for an ECMC simulation with adaptive mesh refinement (AMR); the AMR case used a total of nine batches, with a refinement occurring at the end of the third and sixth batches, for every time step. The initial number of histories was adjusted so that the average number of histories per time step is near 100,000; on average 99,881 histories per time step were used. All ECMC meshes used 4 equally-spaced μ cells initially. The improvement in variance by ECMC compared to SMC is not as significant as for other problems. The FOM is highest for the case of ECMC with adaptive refinement. When the solution can be resolved, the adaptive algorithm allows for a higher convergence rate of statistical variance. It is noted that the consistency terms and LO solution are still computed over the fixed, coarser mesh. However, in general, the refined mesh can produce higher accuracy in consistency terms that is not being measured by the FOM.

Table 5.8: Comparison of sample statistics for the pre-heated marshak wave problem for 100 x cells. Number of ECMC batches is indicated in parenthesis.

hists./step	$\ s\ _{a,rel}$			FOM		
	SMC	ECMC (1)	ECMC (3)	SMC	ECMC (1)	ECMC (3)
12,000	0.86%	0.13%	0.24%	1	41	13
100,000	0.16%	0.042%	0.08%	3.32	52	15
99,881 (AMR)	—	0.038%		—	61	

5.7 Accuracy in the Equilibrium Diffusion Limit

As discussed in Sec. 3.4, we must ensure our method preserves the equilibrium diffusion limit (EDL). We have produced an EDL test problem by adjusting material properties to produce a strongly diffusive domain. This EDL problem has constant

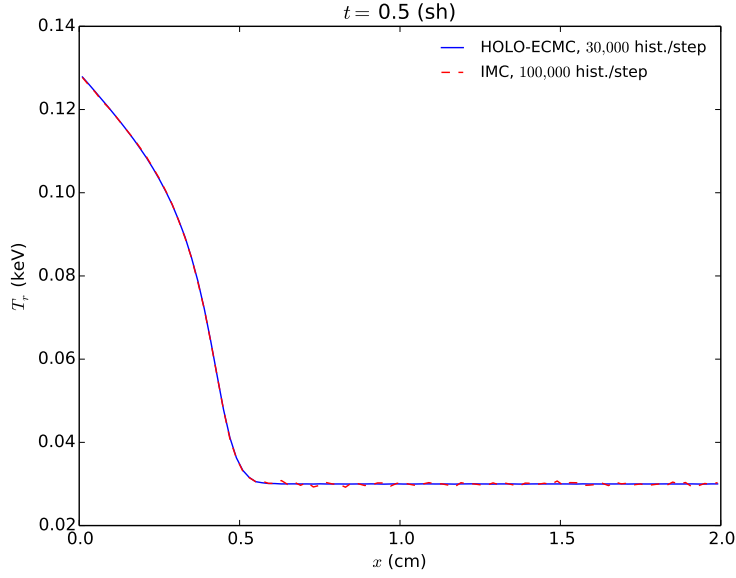


Figure 5.3: Comparison of radiation temperatures for the pre-heated Marshak wave problem for 100 x cells at $t = 0.5$ sh.

cross sections with $\sigma_a = 1000 \text{ cm}^{-1}$, $\sigma_s = 10 \text{ cm}^{-1}$, $\rho c_v = 6.8784 \times 10^{-3} \text{ jk keV}^{-1} \text{ cm}^{-3}$. The initial temperature is 0.01 keV and the domain width is 0.1 cm. The simulation end time is 5 sh, and the step-size increases 5% per time step from $\Delta t = 0.001$ sh to a maximum $\Delta t = 0.01$. In all simulations, 4 μ cells and 3 batches of 4,000 histories were used for the single HO solve, for each time step. We compare HOLO results with a LDFE discretization and a step discretization of the LO equations. The step discretization, with a flat representation over each cell, is known to be inaccurate in the EDL for S_N equations. The step discretization is implemented with the step closure discussed in Sec. 3.6.2 for all cells.

The accuracy in the equilibrium diffusion limit is compared for the two spatial discretizations, for different mesh sizes, in Fig. 5.4. Visually, the LDFE spatial discretization has converged spatially, where both 20 and 200 cells produce the same location of the wave front. However, the step discretization artificially propagates the

energy forward, even for the 200 cells case; the inaccuracy is greater than what would be expected from truncation error. The step discretization will only be accurate if the mesh cells are on the order of a mean free path, which is very large for this problem. Although not plotted, the material temperature overlays the radiation temperature for the LDFE solution, in equilibrium with the radiation, as expected.

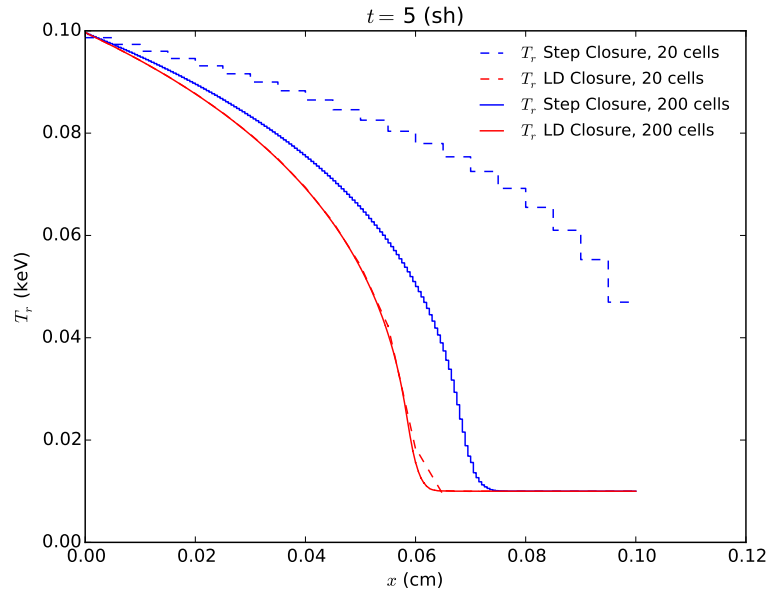


Figure 5.4: Comparison of T_r for a problem in the equilibrium diffusion limit, with step and LDFE discretizations of the LO equations.

5.8 Accuracy of HO Spatial Closure

To investigate the utility of the face closures we compare to the LD spatial closure for two test problems. We are interested in the accuracy of the solution and consistency between the HO and LO solutions, particularly for coarser meshes, based on the metrics in Sec. 5.1. For error computations, the reference solution is based on a fine spatial mesh and L_2 norms are computed with quadrature over the fine mesh.

Cell-averaged quantities are found by spatially averaging the fine mesh solution over each coarse spatial cell. Twenty independent simulations were performed for each metric.

5.8.1 Smooth Problem

For this problem, the radiation and material energies are initially in equilibrium at 0.01 keV. An isotropic incident intensity of 0.05 keV is applied at $x = 0$; the incident intensity on the right boundary is 0.05 keV. The material properties are $\rho = 1 \text{ g cm}^{-3}$, $c_v = 0.2 \text{ jks/keV-g}$, and $\sigma_a = 10 \text{ cm}^{-1}$. The simulation end time is 0.5 sh. The time step size increases by 10% each time step until the maximum step size of 0.01 sh is reached, beginning from $\Delta t = 0.001 \text{ sh}$. This problem is intended to have less steep gradients in the intensity by having constant cross sections, a smaller boundary source, and diffusive problem parameters. The problem has a smaller optical thickness than other problems tested so that the face-based solutions can be efficiently estimated, but the small c_v value makes the solution relatively diffusive. This problem did not require the lumped relation to produce positive solutions. However, when projecting from a refined mesh back to the coarse mesh, it was necessary to rotate the solution to be positive for certain cells and time steps.

All simulations of this problem used 585,900 histories divided over 9 ECMC batches; beginning from 30,000 histories and 10μ cells, 30% of cells were adaptively refined every third batch, and the number of histories was increased to keep the average number of histories per cell constant. We have performed two outer HOLO iterations over each time step for all cases; it was found that additional iterations did not increase consistency, because of the magnitude of statistical noise. Relative convergence of HOLO iterations was below 10^{-3} for two iterations for all cases. Fig. 5.5 compares cell-averaged radiation temperatures for various spatial closures

at coarse mesh sizes and a fine-mesh solution. The HO spatial closures curve is for the scaled-slope closure given by Eq. (3.36). There was visually no difference in the results between the scaled-averaged, scaled-slope, or LD closure. A step closure in all cells was inaccurate for this problem.

Table 5.9 gives the different error metrics for different spatial closures and numbers of cells. The reference solution for all calculations was the average of 10 simulations with $N_c = 500$ spatial cells. In all cases, the HO spatial closure produces higher accuracy in the L_2 norms and greater consistency between the solvers. However, there is not an improvement in accuracy of the cell-averaged intensities. Neglecting noise, the LDFE representation can be third order accurate for the $\|e\|_{a,rel}$ norm and second-order accurate in the L_2 norm [14]. The additional statistical noise and issues discussed in Sec. 5.8.1.1 prevent the MC spatial integration from increasing accuracy spatially over the LDFE discretized LO equations. It is noted that, overall, there is very low statistical noise in each of these solutions due to the ECMC method and relatively high number of histories; at lower history counts, the gains of the HO spatial closure will degrade and stability becomes an issue.

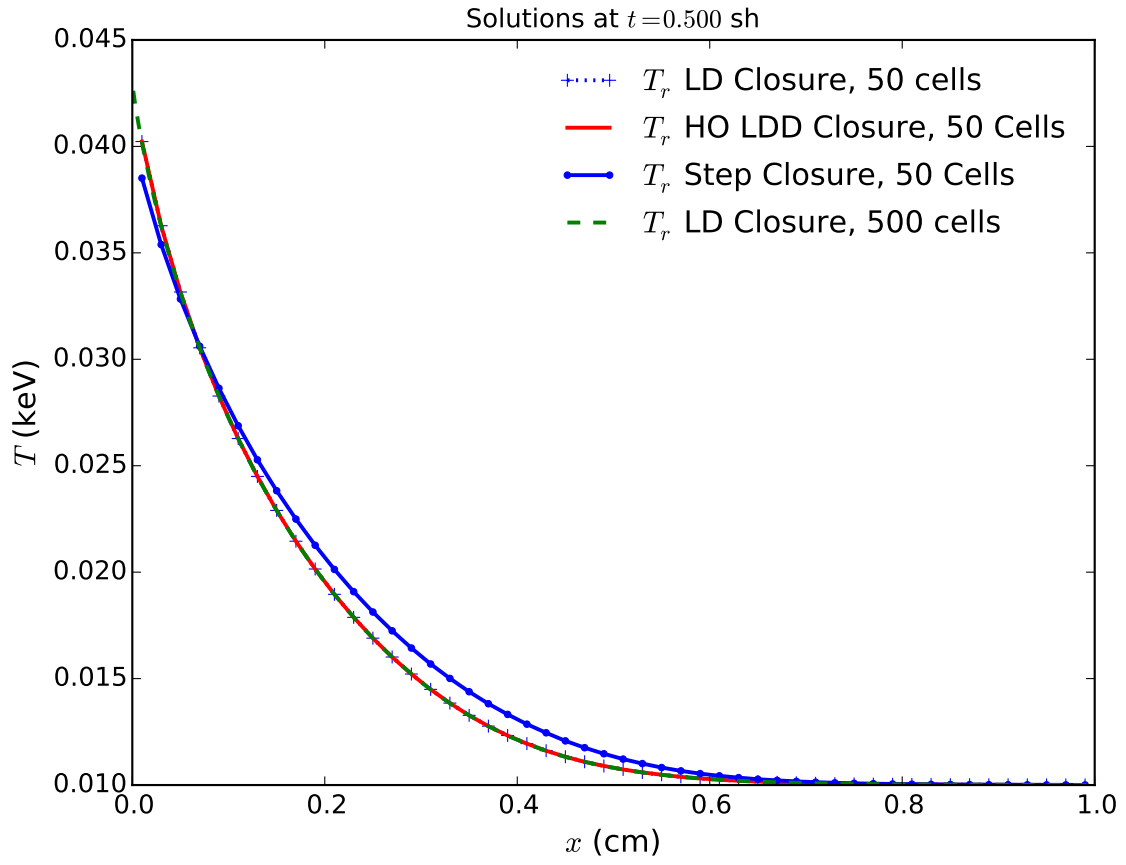


Figure 5.5: Comparison of solutions for smooth problem with different spatial closures.

Table 5.9: Comparison of error metrics, reported as percentages, averaged over 20 simulations of smooth problem. The absolute standard deviation for each value is reported in parenthesis. Reference solution uses 500 cells.

Spatial Closure	$\ e\ _2$		$\ e\ _{a,rel}$		$\ \phi^{HO} - \phi^{LO}\ _{2,rel}$	
$N_c = 20$ cells						
LDFE	6.60%	(0.17%)	2.80%	(5.7e-03%)	2.90%	(8.1e-03%)
HO: Scaled Slope	6.10%	(2.9e-03%)	3.50%	(5.8e-03%)	0.021%	(8.6e-03%)
HO: Scaled Average	6.10%	(2.7e-03%)	3.50%	(5.0e-03%)	0.023%	(1.1e-02%)
$N_c = 50$ cells						
LDFE	1.60%	(7.9e-04%)	0.59%	(3.8e-03%)	0.76%	(4.8e-03%)
HO: Scaled Slope	1.40%	(1.5e-03%)	0.67%	(3.2e-03%)	0.012%	(4.0e-03%)
HO: Scaled Average	1.40%	(1.5e-3%)	0.67%	(3.1e-03%)	0.013%	(3.9e-03%)
$N_c = 100$ cells						
LDFE	0.53%	(2.1e-03%)	0.15%	(2.5e-03%)	0.30%	(9.7e-03%)
HO: Scaled Slope	0.45%	(1.5e-03%)	0.16%	(4.6e-03%)	0.012%	(4.8e-03%)
HO: Scaled Average	0.45%	(1.4e-03%)	0.16%	(4.7e-03%)	0.012%	(3.6e-03%)

5.8.1.1 Issues with the Spatial Closure for HO Solver

There were several observed issues with the ECMC method that cause the LO solution to not exactly preserve the zeroth and first moments of the HO solution, even for a linear transport problem. It is noted that the LO solution remains strictly conservative, and that it is not necessary for the HO solution to be conservative to produce accurate closures. With ECMC, global and particularly local energy balance are generally not preserved by the LDFE representation of the intensity. The HO balance equation is not satisfied exactly and the closure relation is no longer exact for the zeroth moment of the LO equation. However, ECMC will preserve balance

to the order of the iterative error and statistical noise. For standard MC, there are source biasing techniques (e.g., systematic sampling) that exactly preserve the local zeroth moment of the source and thus satisfy local balance [16, 18]). Even with standard MC, for the HOLO method with the LDFE trial space as formulated, we have to reconstruct the bilinear moment of x and μ when computing consistency terms, so the LO equation will not preserve the first moment of the HO solution¹. One final inconsistency is caused by the analog treatment of absorption for particles below the weight cutoff (e.g., see Sec. 4.4). This results in a discrepancy between $\sigma_a c \phi_i^{HO}$ and the actual amount of energy removed from a cell during MC transport, due to statistical noise in the path-length estimators for ϕ_i^{HO} . Thus, the discrete local balance equation over each cell is not exactly preserved by ϕ_i^{HO} .

5.8.2 Two Material Problem

The HO spatial closures were applied to solution of the two material problem detailed in Sec. 5.3. For these results, a small time step size of 0.001 sh was used, with a simulation end time of 2 sh. The scaled-slope closure was found to not stably converge, even for 2 batches of 10^6 histories. The scale-average closure allowed for convergence, with the lumped representation discussed in Sec. 3.6.4, but temperatures were driven below the floor (and at times negative) leading to an inaccurate solution. Fig. 5.6 depicts cell-averaged results at the end of the simulation.

The inaccuracies result from the outflow being driving negative in cells near the wave front with steep gradients. The cause is an inconsistency between the lumped LO moment equations and the fixups for the HO solution in negative cells. In cells with a negative intensity, the HO solution was forced positive by scaling the first

¹It was verified that with standard MC, systematic sampling, no analog sampling, and a closure that is only a function of the zeroth moment, the LO solution exactly reproduces the HO moments, for a linear problem.

moments, and the face solution is strictly positive. However, the relation between these moments does not ensure a positive outflow in the LO equation because the HO and LO first moment equations do not agree.

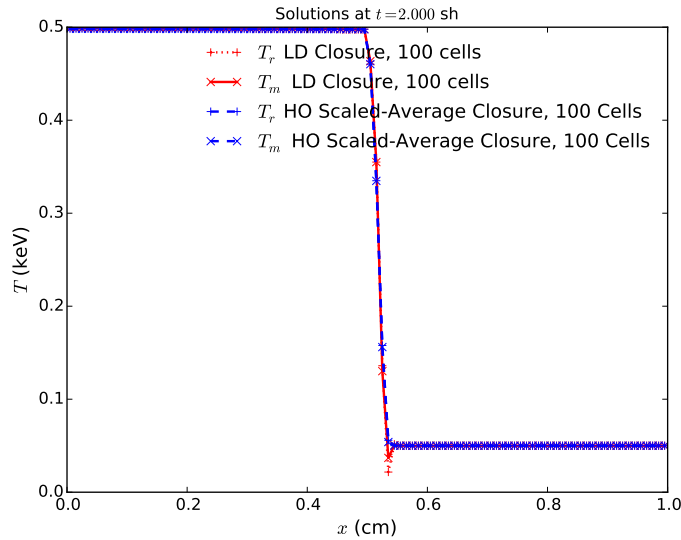


Figure 5.6: Inaccuracies for HO spatial closure applied to solution of the two material problem.

5.9 Preservation of the Discrete Maximum Principle

To numerically demonstrate that our method preserves the discrete MP, as discussed in Sec. 1.3.1, we have simulated problems similar to those in [21]. We produce a problem with tightly coupled equations, by decreasing c_v and increasing σ_a , which results in MP violations for IMC at various fixed time step sizes. The spatial and temporal discretization determine the occurrence of MP violations for IMC. In particular, if time steps are too large or spatial mesh cells are too small, IMC will demonstrate MP violations [21]. Here, we have kept the spatial mesh size fixed and increased the time step size to produce MP violations. The material specifications

are $\sigma_a = \sigma_{a,0} T^{-3} \text{ cm}^{-1}$, $\sigma_{a,0} = 4 \text{ cm}^{-1} \text{ keV}^3$, $\sigma_s = 0 \text{ cm}^{-1}$, $\rho c_v = 0.0081181 \text{ jks keV}^{-1} \text{ cm}^{-3}$. The domain width is 2.0 cm with $N_c = 150$ uniform spatial mesh cells. The radiation and material energies are initially in equilibrium at 0.01 keV, before an isotropic boundary source of 1 keV is applied at the left boundary at $t = 0$. The simulation end time is $t = 0.1 \text{ sh}$.

The material and radiation temperature are plotted for an IMC simulation with $\Delta t = 0.025 \text{ sh}$ in Figure 5.7. Figure 5.8 depicts the material temperature for various time step sizes and the fixed mesh size of 150 cells. All IMC simulations used 100,000 histories per time step. As demonstrated in Fig. 5.7, the material temperature exceeds the specified boundary temperature and is artificially hotter than the radiation temperature. This artificial “temperature spike” also leads to a slower propagation of the wave [21]. As shown in Fig. 5.8, as larger time-step sizes are taken the nonphysical results worsen with the material temperature exceeding the radiation boundary temperature. It is noted that although the final solution for $\Delta t = 0.0001 \text{ sh}$ obeys the MP, during the first few time steps the temperature spikes are present.

The simulations are repeated with the same specifications for the HOLO method. All HOLO simulations used a fixed mesh of 8μ cells by 150 x cells, 3 batches per time step, and 6,000 histories per batch. A single HO solve is performed per time step, and the LO relative convergence tolerance is 10^{-6} . The lumping closure is used for the radiation terms in all spatial cells and any negativities in the HO solution are scaled to the floor value as discussed in Sec. 4.2.3. For these simulations, it was necessary to use the damped Newton’s method discussed in Sec. 3.3 to converge the solutions [36]. A fixed damping parameter with a factor of 0.5 was found to stably converge for all time-step sizes that were simulated.

As seen in Fig. 5.9, the HOLO solution does not violate the maximum principle; the temperature is bounded from above by the radiation boundary condition.

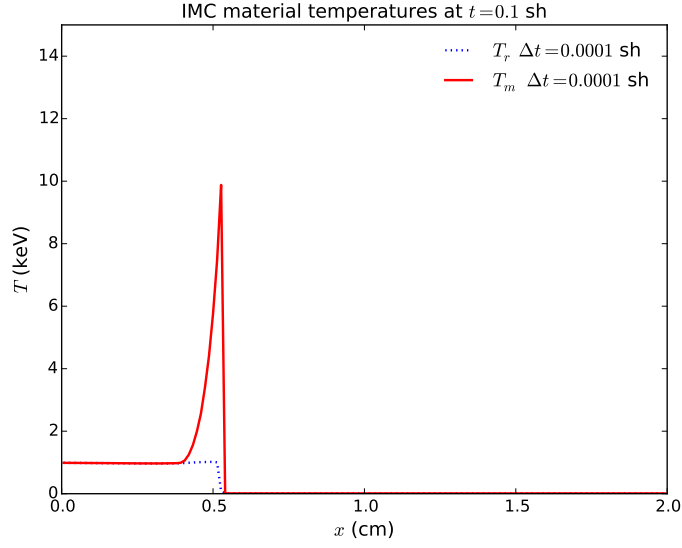


Figure 5.7: T_r and T_m for maximum principle violation problem with IMC and $\Delta t = 0.001$ sh.

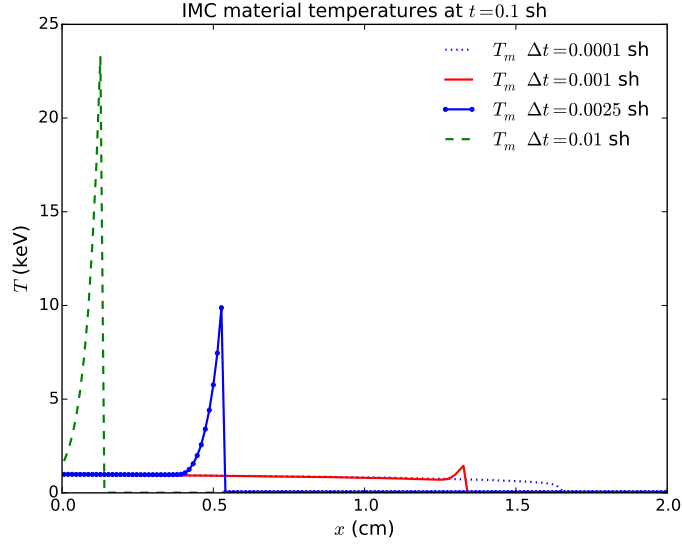


Figure 5.8: T_m for maximum principle violation problem with IMC for various time step sizes. The IMC solution does not preserve the discrete maximum principle.

Table 5.10 demonstrates the LO Newton iteration counts for the HOLO method. For reference, a solution with $\Delta t = 10^{-5}$ sh is given, which required no damping to converge. The damped iterations require more iterations to converge. However, it is necessary to converge the nonlinear iterations to produce physically meaningful solutions to this problem. The advantage of the HOLO method is that there is no additional cost for the HO solution when the damped method is used.

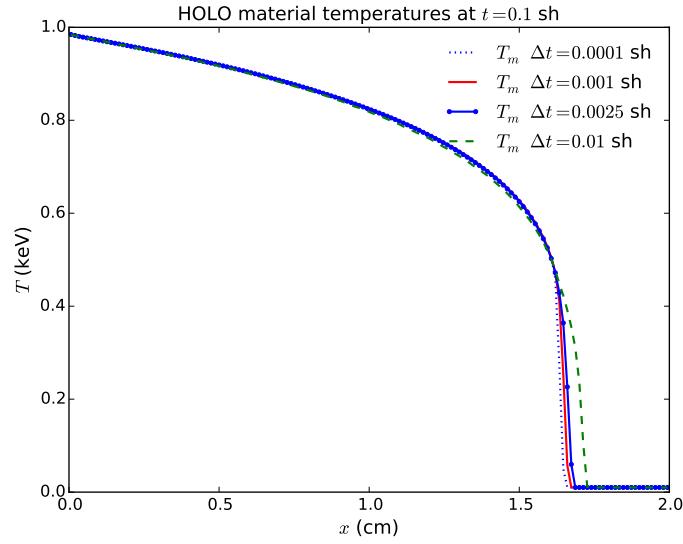


Figure 5.9: T_m for maximum principle violation problem with HOLO method for various time step sizes. The HOLO solution preserves the discrete maximum principle.

Table 5.10: Comparison of LO Newton iterations for HOLO solution to MP problem and different time step sizes. For $\Delta t = 10^{-5}$ sh, no damping was used; for all other cases a damping factor of 0.5 was used.

Δt (sh)	Newton Iters. / LO Solve
10^{-5}	3.5
10^{-4}	21.0
10^{-3}	28.5
2.5×10^{-3}	29.7
10^{-2}	46.3

6. ACCELERATED ITERATIVE SOLUTION TO THE LO EQUATIONS

The fully-discrete, S_2 -like LO equations cannot be directly inverted easily in higher spatial dimensions. To demonstrate a possible path forward in higher dimensions, we have investigated the use of a standard source iteration scheme [11] to invert the scattering terms in the linearized LO equations during each Newton iteration. As material properties become more diffusive (e.g., c_v is small and σ_a is large), the effective scattering cross sections becomes large. This results in a spectral radius of source iterations that approaches unity [14]. These regimes are typical in TRT simulations, so an acceleration method for iterative solutions is critical. We have accelerated the source iterations with a nearly-consistent diffusion synthetic acceleration (DSA) method known as WLA [41, 42]. We have also recast the DSA method as a preconditioner to an iterative Krylov solution [43] of the LO equations. Generally, Krylov methods mitigate acceleration losses due to inconsistencies in the acceleration method. In higher dimensions, the use of a Krylov method is necessary for effective acceleration for nearly-consistent acceleration methods in problems with mixed optical thicknesses [43], e.g., typical radiative transfer problems. Also, applying the preconditioned-Krylov approach allows for the use of spatially lumped DSA equations as a preconditioner, with the LO equations using an LD or HO spatial closure.

The remainder of this chapter is structured as follows: The source iteration solution to the LO equations is detailed. Then, the equations for the WLA DSA method are derived and the acceleration algorithm is given. The DSA method is then recast as a preconditioner to a GMRES solution of the scattering iteration equations. Finally, convergence results are compared for several test problems.

6.1 Source Iteration Solution to the Linearized LO Equations

The time-discrete LO equations, after linearization, can be solved with a source iteration method [11, 43, 44]. In the source iteration process the scattering source is lagged, which uncouples unknowns between the two half ranges. This produces a lower-triangular system where the spatial unknowns can be solved for sequentially along the two directions of flow via a standard sweeping procedure [11, 14]. Beginning at the left boundary, the positive unknowns can be determined for each cell from $i = 1, \dots, N_c$; because the inflow to the i -th cell is defined from the previous cell or boundary condition, a local system of equations can be solved for the $\langle \phi \rangle_{L,i}^+$ and $\langle \phi \rangle_{R,i}^+$ unknowns. The negative direction unknowns are determined similarly, starting from the right boundary and proceeding towards the left. The newly computed half-range intensities can then be used to estimate the scattering source for the next iteration. This process is repeated until convergence.

The source iteration process can be written in operator notation as

$$\mathbf{M}\underline{\psi}^{l+1} = \frac{1}{2}\mathbf{S}\underline{\psi}^l + \underline{Q}, \quad (6.1)$$

where \mathbf{M} is the LO streaming and removal operator (i.e., the left-hand side of Eqs. (3.18)–(3.21) without the scattering terms included), $\underline{\psi}$ is a vector of the half-range FE moment unknowns, and the vector \underline{Q} contains the fixed source terms resulting from the linearized emission source and previous time step moments, for each equation. For the i -th element and the L equation, for both half-ranges, the source terms are

$$(\underline{Q})_{i,L}^{\pm} = \frac{h_i \langle \phi \rangle_{L,i}^{\pm,n}}{c\Delta t} + \frac{1}{2} h_i f_i \sigma_{a,i} a c \langle (T^n)^4 \rangle_{L,i}, \quad (6.2)$$

the scattering operator terms are

$$(\mathbf{S}\underline{\psi}^l)_{i,L}^{\pm} = h_i (\sigma_{a,i}(1 - f_i) + \sigma_{s,i}) (\langle \phi^l \rangle_{i,L}^{+,n+1} + \langle \phi^l \rangle_{i,L}^{-,n+1}), \quad (6.3)$$

and the streaming and removal terms, for the LD spatial closure, are

$$\begin{aligned} (\mathbf{M}\underline{\psi}^{l+1})_{i,L}^{\pm} = & -2\mu_{i-1/2}^{n+1,+} (2\langle \phi^{l+1} \rangle_{R,i-1}^{n+1,+} - \langle \phi^{l+1} \rangle_{L,i-1}^{n+1,+}) + \{\mu\}_{L,i}^{n+1,+} \langle \phi^{l+1} \rangle_{L,i}^{n+1,+} \\ & + \{\mu\}_{R,i}^{n+1,+} \langle \phi^{l+1} \rangle_{R,i}^{n+1,+} + \left(\sigma_{t,i}^{n+1} + \frac{1}{c\Delta t} \right) h_i \langle \phi^{l+1} \rangle_{L,i}^{n+1,+} \end{aligned} \quad (6.4)$$

where all consistency terms are known from the HO solver. Equivalent expressions are defined for the R moment equations and boundary conditions, forming a fully defined set of equations. The process of sweeping is denoted as \mathbf{M}^{-1} .

The scattering inversion must be performed within each Newton iteration. Thus, for the m -th *Newton step*, the source iteration process is defined as

1. Evaluate effective scattering and absorption cross sections with the temperatures from the current Newton step, i.e., $\{T_i^m : i = 1, 2, \dots, N_c\}$.
2. Compute new scattering source $\frac{1}{2}\mathbf{S}\underline{\psi}^l$.
3. Perform sweeps to calculate $\underline{\psi}^{l+1} = \mathbf{M}^{-1}\mathbf{S}\underline{\psi}^l + \mathbf{M}^{-1}\underline{Q}$
4. If $\|\underline{\psi}^{l+1} - \underline{\psi}^l\|_2 < \text{tolerance } \|\underline{\psi}^{l+1}\|_2$, move to next Newton step. Else, repeat steps 2–4.

6.2 Linear Diffusion Synthetic Acceleration

A form of DSA referred to as the WLA method is used to accelerate the source iterations [41, 42]. Between each sweep, an error equation for the scattering iterations is solved with an approximate angular discretization of the transport equation. The

estimated error is used to correct the zeroth moment of the intensity unknowns. In operator notation, the DSA equations for a single iteration are

$$\mathbf{M}\underline{\psi}^{l+1/2} = \frac{1}{2}\mathbf{S}\underline{\psi}^l + \underline{Q} \quad (6.5)$$

$$\mathbf{D}\delta\phi^{l+1/2} = \mathbf{S}(\underline{\psi}^{l+1/2} - \underline{\psi}^l) \quad (6.6)$$

$$\underline{\psi}^{l+1} = \underline{\psi}^{l+1/2} + \frac{1}{2}\delta\phi^{l+1/2}, \quad (6.7)$$

where $\delta\phi$ represents the error in the mean intensity unknowns. The operator \mathbf{D} represents a diffusion-like approximation to the transport equation. The DSA equations contain a standard finite-difference diffusion discretization that can be more efficiently inverted than the S_2 -like equations that are being accelerated (particularly in higher spatial dimensions), but will accurately resolve the slowly-converging, diffusive error modes.

It is important for the spatial discretization of Eq. (6.6) to be closely related to the discretization of the LO equations for the acceleration to be effective and stable [45]. The WLA method first solves a spatially-continuous discretization of the diffusion equation for the error at faces $\{x_{i+1/2} : i = 0, 1, \dots, N_c\}$. The error on the faces is then mapped onto the volumetric moment errors via a LD discretization of the P_1 equations [41]. The LD mapping resolves issues that would occur in optically-thick cells, and the continuous diffusion equation is accurate in the EDL where acceleration is important [45].

The continuous diffusion equation and mapping equations for the WLA method are derived in Appendix C. To allow for the use of lumped or standard LD in the DSA equations, we introduce the factor θ , with $\theta = 1/3$ for standard LD, and $\theta = 1$ for lumped LD. With suppression of the time indices, the diffusion equation for the

face at $x_{i+1/2}$ is

$$\begin{aligned} & \left(\frac{\sigma_{a,i+1} h_{i+1}}{4} (1 - \theta) - \frac{D_{i+1}}{h_{i+1}} \right) \delta \phi_{i+3/2} \\ & + \left(\frac{D_{i+1}}{h_{i+1}} + \frac{D_i}{h_i} + \left(\frac{1 + \theta}{2} \right) \left[\frac{\sigma_{a,i+1} h_{i+1}}{2} + \frac{\sigma_{a,i} h_i}{2} \right] \right) \delta \phi_{i+1/2} \\ & + \left(\frac{\sigma_{a,i} h_i}{4} (1 - \theta) - \frac{D_i}{h_i} \right) \delta \phi_{i-1/2} = \frac{h_{i+1}}{2} \langle q \rangle_{L,i+1} + \frac{h_i}{2} \langle q \rangle_{R,i} . \end{aligned} \quad (6.8)$$

The source in Eq. (6.8) is the residual for a given scattering iteration [43, 11]

$$\langle q \rangle_{L/R,i} = \sigma_{s,i} (\langle \phi^{l+1/2} \rangle_{L/R,i} - \langle \phi^l \rangle_{L/R,i}) . \quad (6.9)$$

It is noted that there is no need to define the source differently for the lumped or standard LD DSA equations, because the source is in terms of moments, which are provided by the LO unknowns.

The LO iterate exactly satisfies the inflow boundary conditions, therefore a vacuum boundary condition is applied to the diffusion error equations. Application of Eq. (C.10) gives the left boundary condition:

$$\left(\frac{1}{2} + \sigma_{a,1} h_1 \frac{1 + \theta}{4} - \frac{D_1}{h_1} \right) \delta \phi_{1/2} + \left(\sigma_{a,1} h_1 \frac{1 - \theta}{4} - \frac{D_1}{h_1} \right) \delta \phi_{3/2} = \frac{h_1}{2} \langle q \rangle_{L,1} \quad (6.10)$$

The boundary condition for the right-most face is

$$\left(\frac{1}{2} + \sigma_{a,I} h_I \frac{1 + \theta}{4} - \frac{D_I}{h_I} \right) \delta \phi_{I+1/2} + \left(\sigma_{a,I} h_I \frac{1 - \theta}{4} - \frac{D_I}{h_I} \right) \delta \phi_{I-1/2} = \frac{h_I}{2} \langle q \rangle_{R,I} \quad (6.11)$$

where I is the index of the right-most cell.

The system of equations formed from Eqs. (6.10), (6.11), and (6.8) is symmetric and has a matrix bandwidth of 3, compared to the bandwidth of 7 of the LO equa-

tions. The system is solved directly with a banded matrix solver. Then, Eq. (C.23)–(C.26) are solved in each cell to map the face errors onto an LD representation over the interior. It is noted that unlike fully consistent DSA equations, the WLA-DSA algorithm does not preserve particle balance to round off. This is because the mapping procedure uses an approximate inflow to each cell, which is inconsistent with the partial outflows from adjacent cells. Thus, overall, our algorithm will only conserve energy to the order of scattering iteration convergence.

Because we are interested in the time-dependent solution, we need to update the solution for the half-range intensities, rather than just the zeroth moment. We do not accelerate the first moment of the angular intensity, as the solution for ΔJ is inaccurate due to the approximations introduced. The LD edge values for the error must be mapped onto the corresponding spatial moments. The updated half-range moments for each cell, as derived in the appendix, using the lumping notation is

$$\langle \psi \rangle_L^{\pm, l+1} = \langle \psi \rangle_L^{\pm, l+1/2} + \frac{1}{2} \left[\frac{1+\theta}{4} \delta \phi_L^{l+1/2} + \frac{1-\theta}{4} \delta \phi_R^{l+1/2} \right] \quad (6.12)$$

$$\langle \psi \rangle_R^{\pm, l+1} = \langle \psi \rangle_L^{\pm, l+1/2} + \frac{1}{2} \left[\frac{1-\theta}{4} \delta \phi_L^{l+1/2} + \frac{1+\theta}{4} \delta \phi_R^{l+1/2} \right]. \quad (6.13)$$

6.2.1 The WLA-DSA Accelerated Source Iteration Algorithm

We define the process of solving the diffusion like equations and mapping the error unknowns back onto the moment equations as the operator \mathbf{D}^{-1} . The source iteration with linear DSA procedure, for the m -th Newton iteration, is

1. Evaluate effective scattering and absorption cross sections with the temperatures from the current Newton step, i.e., $\{T_i^m : i = 1, 2, \dots, N_c\}$.
2. Compute new scattering source $\underline{\mathbf{S}}\psi^l$.

3. Perform sweeps to calculate $\underline{\psi}^{l+1/2} = \mathbf{M}^{-1}\mathbf{S}\underline{\psi}^l + \mathbf{M}^{-1}\underline{Q}$
4. Perform DSA iteration to solve $\delta\phi^{l+1/2} = \mathbf{D}^{-1}\mathbf{S}(\underline{\psi}^{l+1/2} - \underline{\psi}^l)$
 - Solve continuous DSA equations, i.e., Eqs. (6.8), (6.11), and (6.8), for $\{\delta\phi_{i+1/2}^{l+1/2} : i = 0, 1, \dots, N_c\}$.
 - Map the continuous error onto the moment errors, via Eq. (C.23)–(C.26).
5. Add correction to the moment unknowns via Eq. (6.12) and (6.13) to produce $\underline{\psi}^{l+1} = \underline{\psi}^{l+1/2} + \frac{1}{2}\delta\phi^{l+1/2}$
6. If $\|\underline{\psi}^{l+1} - \underline{\psi}^l\|_2 < \text{tolerance } \|\underline{\psi}^{l+1}\|_2$, then exit. Else, repeat steps 2–6.

6.3 GMRES Solution to the LO Equations

The source iteration procedure can be recast as an iterative solution to a matrix equation. Using operator notation, we manipulate the moment equations to form a matrix equation:

$$(\mathbf{I} - \mathbf{M}^{-1}\mathbf{S}) \underline{\psi} = \mathbf{M}^{-1}\underline{Q}, \quad (6.14)$$

where \mathbf{I} is an identity matrix. The GMRES method is used to approximate the solution to the above linear system. The GMRES method is an iterative Krylov solution method for asymmetric, sparse matrix equations. Approximate solution to the above equation is formed by producing the l -th Krylov vector $\underline{\psi}^l$, where $\underline{\psi}^l$ minimizes the norm of the residual for Eq. (6.14) and is a member of the l -th orthonormalized Krylov subspace [46]. To form the Krylov subspace in each iteration, the matrix operator, i.e., the left-hand side of Eq. (6.14), is applied to the previous Krylov vector. Rather than building the full matrix system, we apply the operation of \mathbf{S} and \mathbf{M}^{-1} as detailed in Sec. (6.1) to apply $(\mathbf{I} - \mathbf{M}^{-1}\mathbf{S})$ to the generated Krylov vectors.

The GMRES method will generally converge faster than the source iteration procedure [43]. However, as the system becomes scattering dominated, convergence will degrade. To improve the convergence rate, we precondition the GMRES system with a solution of the WLA-DSA equations. The goal of preconditioning is to efficiently apply an operator to the equation that will approximate the inverse of the matrix operator. Left preconditioning [46] was applied to the above system. In matrix form, we write the preconditioned GMRES equations as

$$(\mathbf{I} + \mathbf{D}^{-1}\mathbf{S}) (\mathbf{I} - \mathbf{M}^{-1}\mathbf{S}) \underline{\psi} = (\mathbf{I} + \mathbf{D}^{-1}\mathbf{S}) \mathbf{M}^{-1}\underline{Q}. \quad (6.15)$$

The operation of $(\mathbf{I} + \mathbf{D}^{-1}\mathbf{S})^{-1}$ is equivalent to the DSA procedure where the scattering residual is simply $\mathbf{S}\psi^l$ and the correction is directly added to the passed in Krylov vector.

The open-source library **mgmres** was modified to implement the matrix-free version of the GMRES procedure. The infrastructure from the source iteration with DSA procedure is reused to provide the operation of $(\mathbf{I} + \mathbf{D}^{-1}\mathbf{S}) (\mathbf{I} - \mathbf{M}^{-1}\mathbf{S})$ applied to the Krylov vectors returned from the GMRES solver. The preconditioned-GMRES algorithm is

1. Evaluate effective scattering and absorption cross sections with the temperatures from the current Newton step, i.e., $\{T_i^m : i = 1, 2, \dots, N_c\}$.
2. Initialize Krylov vector as $\underline{\psi}^0 = 0$.
3. Form source vector \underline{b} with sweep: $\underline{b} = \mathbf{M}^{-1}\underline{Q}$.
4. Apply left-preconditioner operator to \underline{b} , so $\underline{b} \leftarrow (\mathbf{I} + \mathbf{D}^{-1}\mathbf{S}) \mathbf{M}^{-1}\underline{Q}$.
5. Apply sweep and subtraction to Krylov vector: $\underline{\psi}^{l+1/2} = (\mathbf{I} - \mathbf{M}^{-1}) \underline{\psi}^l$.

6. Perform DSA iteration to determine $\underline{\psi}^{l+1/2} \leftarrow (\mathbf{I} + \mathbf{D}^{-1}\mathbf{S}) \underline{\psi}^{l+1/2}$
7. Apply GMRES step to \underline{b} and $\underline{\psi}^{l+1/2}$ to generate next Krylov vector $\underline{\psi}^{l+1}$.
8. If the norm of the residual for $\underline{\psi}^{l+1}$ is below tolerance, then exit. Else, repeat steps 5–7.

The convergence tolerance is relative to the initial residual of the first iteration with non-zero $\underline{\psi}$. To perform GMRES without preconditioning, steps 3 and 6 are removed.

6.4 Computational Results

We have tested the iterative solution methods for three test problems and compare the average number of scattering iterations to converge. For each simulation, three batches of 10,000 particles are ran for the single HO solve per time step, and 200 spatial cells were used. The average number of source iterations per Newton step is recorded, as well as the total number of Newton iterations per time step (there are two LO solves per time step). The initial guess for the effective scattering source is set to zero at the beginning of each LO solve. All scattering iterations have a relative convergence of 10^{-10} . For all DSA simulations, we have used the lumped spatial representation for the DSA equations.

The first test problem is the two material problem in Sec 5.3. The time step is increased linearly by 15% each time step from $\Delta t = 0.001$ sh to reach a maximum time step size of 0.01 sh. The large time step sizes increases the magnitude of the effective scattering cross section. Table 6.1 gives iteration counts for each method: unaccelerated source iteration (SI), source iteration with DSA (SI-DSA), unaccelerated GMRES (GMRES), and GMRES with DSA preconditioning (GMRES-DSA). As demonstrated, DSA improves the convergence of the source iteration method. The preconditioned GMRES was more efficient than standard GMRES.

The second test problem is a modification of the two material problem. The problem specifications are the same as before except for modifications to the cross sections for $x > 0.5$ cm; in the right half of the domain, the parameters are $\sigma_a = 20,000 \text{ cm}^{-1}$, $\sigma_s = 500 \text{ cm}^{-1}$. This problem is highly diffusive and nonlinear. The Newton method required damping with a damping factor of 0.6 to stably converge. Table 6.2 gives the iteration counts. Overall, the damping increases the number of Newton steps, as expected. For this problem, acceleration is much more critical, reducing the number of scattering iterations by a factor of 100.

For the final test problem, we test the equilibrium diffusion limit problem from Sec. 5.7. The problem was tested with standard LD and lumping-equivalent LD spatial closures, with the DSA using the lumped representation in both cases. Table 6.3 compares scattering iterations for the EDL problem. There was minimal degradation observed for the diffusion limit problem due to the difference in spatial discretizations. This is likely because both lumped LD and LD representations produce accurate solutions in the EDL.

Table 6.1: Scattering source iterations for the two material problem. Simulation end time is 1 sh.

Method	Sweeps/Newton Iter.	Newton Iters./Time Step
SI	247.0	19.4
SI-DSA	10.1	19.3
GMRES	14.1	19.4
GMRES-DSA	8.7	19.3

Table 6.2: Scattering source iterations for the modified, diffusive two material problem. Simulation end time is 2 sh.

Method	Sweeps/Newton Step	Newton Iters./Time Step
SI	1037	25.2
SI-DSA	10.9	25.1
GMRES	12.6	25.1
GMRES-DSA	7.0	25.2

Table 6.3: Scattering source iterations for the equilibrium diffusion limit problem. Simulation end time is 3 sh.

LD LO Equations		
Method	Sweeps/Newton Step	Newton Steps/LO Solve
SI	357.4	8.4
SI-DSA	21.9	8.4
GMRES	37.5	8.4
GMRES-DSA	14.3	8.4
Lumped LO Equations		
SI	359.8	8.2
SI-DSA	14.6	8.2
GMRES	38.3	8.2
GMRES-DSA	10.8	8.2

7. RESOLVING ISSUES WITH NEGATIVE INTENSITIES FOR ECMC

The linear-discontinuous (LD) spatial closure with upwinding is not strictly positive. In particular, for optically thick cells with a steep intensity gradient, the linear representation of the intensity can become negative at the edge of the cells. A common example in 1D is for the Marshak Wave problem where negative intensities in the representation occurs at the foot of the radiation wave front. These negativities are not physical and typically propagate to adjacent cells through the streaming term. In thick regions of TRT problems, reasonably fine spatial cells can still be on the order of millions of mean free paths; negativities with an LD representation are unavoidable in practice for such cells, and mesh refinement is of minimal use. The LDFE representation of the intensity for the HO solver is prone to additional negativities near $\mu = 0$ where the intensity often cannot be accurately represented by a linear projection in angle. These negativities near $\mu = 0$ can occur for modest optical thicknesses and in multiple adjacent cells, caused in part by the previous intensity source term which has a strong gradient in μ .

In the remainder of this chapter, we present different fixup methods applied to the HO solver. Methods are then compared for statistical efficiency and accuracy for test problems. Ideally the fixup should be applied in a manner that the solutions in such cells are as consistent as possible between the HO and LO equations. However, even if the HO fixup was applied consistently to the LO next nonlinear LO solve, this would be based on a lagged HO problem so there is no guarantee of positivity for the new LO solution. Additionally, the LO solver must preserve energy conservation, whereas the HO solver is primarily used for angular shape parameters and is not conservative. Thus, because of the difference in solution methods of the two system,

independent fixups have been developed.

7.1 Calculating a Positive LDFE Representation

For the HO solver, in cells near the radiation wavefront, the LDFE trial space results in negative values in $\tilde{I}^{n+1}(x, \mu)$, similar to the LO solver. In general, in such cells where the trial space cannot accurately represent the solution, error stagnation will rapidly occur. At the end of any particular batch, a LDFE projection of the intensity $\tilde{I}(x, \mu)$ has been determined. This projection is based on a statistical estimate of the moments of the intensity, based on the truncated representation of sources. Although the statistically estimated moments are physically accurate, when these moments are projected onto a linear space the representation becomes negative, over some portion of certain elements' domains. Because the residual formulation in ECMC allows for negative weight particles to occur, there is not a strict requirement to fixup the cells. However, in cells where $\tilde{I}^{n+1}(x, \mu)$ crosses zero, the angular consistency terms are not guaranteed to lie in the appropriate half-space, potentially introducing instabilities.

The first moments can easily be modified, rotating the linear representation for the intensity about the average, to produce a positive representation \tilde{I}_{pos} at the end of a batch. We produce a positive representation \tilde{I}_{pos} over a cell by scaling the first moment in x and μ uniformly. The process of modifying the first moments to produce a positive solution is under defined, so there is not a unique way to enforce positivity. This choice is not an emphasis of this research, so we have applied the simple approach of scaling the slopes such that the ratio I_x/I_μ for each modified cell is unchanged. After an ECMC batch, we detect cells where the linear representation produces a value below the floor. The modified representation for the ij -th cell in

such cells is

$$\tilde{I}_{\text{pos}} = I_a + C \left[\frac{2}{h_x} I_x (x - x_i) + \frac{2}{h_\mu} I_\mu (\mu - \mu_j) \right], \quad (x, \mu) \in \mathcal{D}_{ij}, \quad (7.1)$$

noting that the average has not been modified. The constant C is calculated as

$$C = \frac{I_a - I_{\min}}{|I_x| + |I_\mu|} \quad (7.2)$$

for values where $I_a > I_{\min}$, where I_{\min} is the isotropic intensity corresponding to equilibrium with the floor temperature. When I_a is below the floor, it is set to the floor value and I_x and I_μ set to zero. It is been noted that in application the difference between I_a and I_{\min} can be on the order of numerical roundoff for double precision variables.

7.2 Artificial Source Method for Negativities in the HO Intensity

The moments of the modified positive solution \tilde{I}_{pos} will not necessarily satisfy the residual equation as accurately as the original solution, which leads to rapid error stagnation. Additionally, the next MC batch based on the residual source from \tilde{I}_{pos} can produce negative cell averages in down stream cells. Thus, we have devised a method to modify the transport equation such that \tilde{I}_{pos} will locally satisfy the residual equation more accurately. We do this in such a manner that the modified source will lead to the solution converging towards a solution with the same zeroth moment, but with a first moment in x and μ that are modified. This does not guarantee exponential convergence of the solution, because convergence is still limited by the overall accuracy of the trial space and statistics within a batch. However, now the error will not stagnate as rapidly and the solution will converge towards the positive representation \tilde{I}_{pos} .

To mitigate stagnation and improve efficiency, we can add an artificial source $\tilde{\delta}^{m+1}(x, \mu)$ to the HO transport equation. This source is estimated iteratively as

$$\tilde{\delta}(x, \mu)^{(m+1)} = \mathbf{L}(\tilde{I}^{n+1,(m)} - \tilde{I}_{\text{pos}}^{n+1,(m)}),$$

where $\tilde{I}_{\text{pos}}^{n+1,(m)}$ is the modified positive solution, for all cells that required modification. The source $\tilde{\delta}$ is added to all later batches. If necessary, we can add an additional source in later batches where negative values occur once more. The residual for the modified transport problem will have the same residual magnitude as the original \tilde{I} , which will have lower magnitude than the modified solution which does not have the MC estimated first moments (this is only true for the first application of the modified source). Care must be taken to modify the source on the interior and exterior of the cell, particularly when the solutions in adjacent cells has been modified. The source $\tilde{\delta}$ lies in the same functional space as the residual and can thus use the existing code infrastructure to compute the source. This will also make this approach straight forward to extend to higher dimensions and adaptively refined meshes.

To provide insight into the choice of this source, consider the modified transport problem that will be solved with ECMC, where the fixup has been applied at batch m :

$$\mathbf{L}I^{n+1} = q + \mathbf{L}(\tilde{I}^{n+1,(m)} - \tilde{I}_{\text{pos}}^{n+1,(m)}) \quad (7.3)$$

Application of \mathbf{L}^{-1} to both sides of the equation produces

$$I^{n+1} = \mathbf{L}^{-1}q + (\tilde{I}^{n+1,(m)} - \tilde{I}_{\text{pos}}^{n+1,(m)}). \quad (7.4)$$

Because \tilde{I} and \tilde{I}_{pos} have the same zeroth moment, we have not modified the zeroth moment of the solution overall, in the limit of an infinite number of histories. Monte

Carlo transport is used to estimate L^{-1} , thus we are estimating the solution to a transport problem that has a modified first moment in the LDFE projection but preserves the zeroth moment of the original solution. The estimate of the modification to the first moments of the solution has statistical noise, and thus may under- or over-predict the necessary change in the solution. We make the conservative choice of preserving δ across batches, and adding an additional source only when negative values occur again.

7.3 Computational Results

We will apply several different fixup approaches based on the above discussion. The first method, labeled as “S₂ fixup” is the simplified fixup used to generate some of the results in Chapter 5: we detect if the consistency terms lie in the appropriate half space at the end of the HO solve, an indication that the intensity was negative within that cell. If the terms are non-physical, then they are replaced with the corresponding S₂-equivalent value. At the end of each time step the solution is rotated positive for the next time step. The second method, labeled as “Rotate Every Batch” rotates the solution above the floor value as needed at the end of every batch, as described in Sec. 7.1. The method “Rotate Last Batch” only applies the fixup at the end of the final batch, allowing negative intensities in earlier batches. The final approach is labeled “Artificial Source” and is described in the previous section. The artificial source is not saved between time steps.

7.3.1 *Analytic Fixed Source Problem*

We first test the fixup methods for an analytic fixed-source, pure-absorber transport problem. It is difficult to generate an analytic answer to non-trivial TRT problems, so we apply the fixups to a fixed-source problem with similar characteristics to the two material problem in Sec. 5.3 that produces negative solutions for $\tilde{I}(x, \mu)$.

The general isotropic source is proportional to σ_a , so the 1D transport equation to be solved is

$$\mu \frac{\partial I(x, \mu)}{\partial x} + \sigma_a I(x, \mu) = \frac{q_0 \sigma_a(x)}{2}. \quad (7.5)$$

The form of the source simulates a floor equilibrium distribution and ensures that $\phi^-(x)$ is a constant throughout the domain with appropriate boundary conditions.

For this problem, the domain width is 1.0 cm and $\sigma_s = 0$ throughout. The absorption cross section is defined as $\sigma_a = 0.2 \text{ cm}^{-1}$ for $0 \leq x < 0.5 \text{ cm}$ and $\sigma_a = 1000 \text{ cm}^{-1}$ for $0.5 < x \leq 1.0 \text{ cm}$. The analytic solution for the mean intensity, as derived in App. B.2, is

$$\phi(x) = I_{inc} E_2[\tau(x)] + \frac{q_0}{2} (2 - E_2[\tau(x)]), \quad (7.6)$$

where $I_{inc} = 1000 \text{ cm}^{-2} \text{ str}^{-1}$ is the incident intensity at the left boundary and $q_0 = 0.5 \text{ cm}^{-2} \text{ s}^{-1}$; The equilibrium solution which is used as the floor in the applied fixups is $I_{min} = 0.5 \text{ cm}^{-2} \text{ s}^{-1} \text{ str}^{-1}$.

The problem was simulated with the HOLO algorithm with four batches of 100,000 histories, with no HO fixup. For the LO solver, the lumped LD spatial closure is used in all cells. For the single HO solve, the solution is initialized to $\tilde{I}(x, \mu) = q_0/2$. A plot of the HO representation for the intensity¹ is given in Fig. 7.1a from the end of the HO solve. Figure 7.1b depicts the solution for all cells in which $\tilde{I}(x, \mu)$ is below I_{min} , for some portion of that cell's domain, using a smaller scale for visual clarity. As expected, near $\mu = 0$ and near the interface of the thick material the LDFE projection is driven negative and cannot accurately represent the solution.

The various fixup methods were tested on this problem for different numbers of

¹The triangular structure and different shades of color in the plots are only artifacts of the plotting software, and do not indicate any gradient.

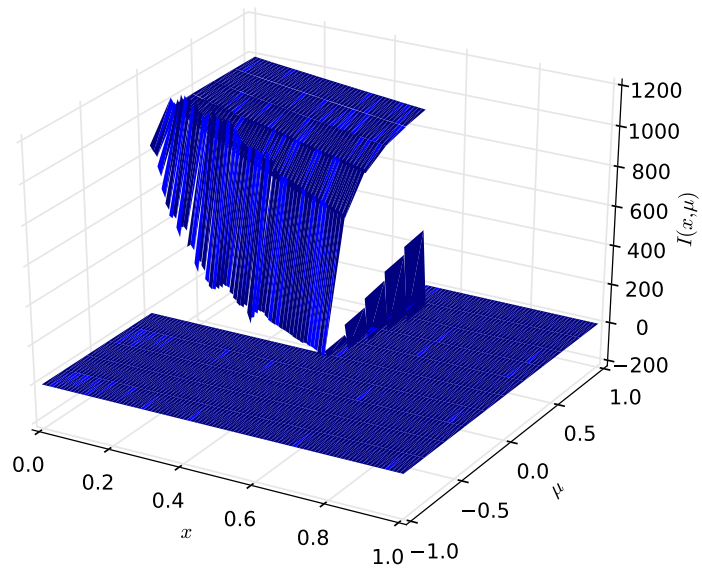
Table 7.1: Comparison of accuracy in cell-averaged $\phi(x)$ value for fixed source problem and various number of histories per batch.

Fixup Method	$\ e_{LO}\ _{a,rel}$		$\ e_{HO}\ _{a,rel}$		FOM
4 batches, $N_b = 10^4$ histories per batch					
Artificial Source	1.354%	(0.07%)	1.657%	(0.10%)	0.43
S ₂ Fixup	1.135%	(0.04%)	1.335%	(0.05%)	0.68
Rotate every Batch	0.883%	(0.04%)	1.036%	(0.05%)	1.09
Rotate Last Batch	1.100%	(0.04%)	1.335%	(0.05%)	0.72
4 batches, $N_b = 10^5$ histories per batch					
Artificial Source	0.261%	(0.01%)	0.304%	(0.01%)	1.34
S ₂ Fixup	0.268%	(0.01%)	0.302%	(0.01%)	1.29
Rotate every Batch	0.232%	(0.01%)	0.265%	(0.01%)	1.76
Rotate Last Batch	0.267%	(0.01%)	0.302%	(0.01%)	1.30
4 batches, $N_b = 10^6$ histories per batch					
Artificial Source	0.081%	(0.002%)	0.097%	(0.002%)	1.47
S ₂ fixup	0.083%	(0.002%)	0.094%	(0.003%)	1.38
Rotate every Batch	0.072%	(0.002%)	0.082%	(0.003%)	1.84
Rotate Last Batch	0.083%	(0.002%)	0.094%	(0.003%)	1.39

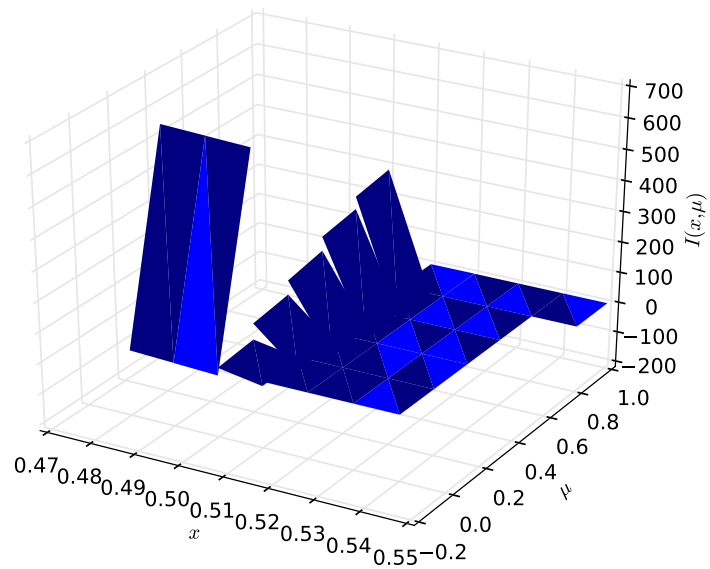
simulated histories. The L_2 norm of the error in cell-averaged mean intensities $\|e\|_{a,rel}$ was computed using Eq. (5.8) for both the HO and LO solutions, averaged over 100 simulations. Table 7.1 compares the errors and FOM values. The absolute sample standard deviation follows each value in parenthesis as appropriate. Generally, the artificial source fixup did not improve accuracy or statistics for this problem, and the other fixups show similar performance. In some cases the artificial source led to additional negative values in down-stream space-angle cells in later batches. It is noted that for this problem that although some negative intensities occur, for the S₂ fixup angular consistency terms were non-physical in only a few cases.

7.3.2 Radiative Transfer Problems

We now test each of the fixups to the Marshak wave problem and two material problem from Secs. 5.2 and 5.3. For both problems, Δt is linearly increased from



(a) Full plot of $\tilde{I}(x, \mu)$.



(b) $\tilde{I}(x, \mu)$ for cells where $\tilde{I}(x, \mu)$ crosses I_{\min} .

Figure 7.1: LDFE projection of angular intensity $\tilde{I}(x, \mu)$ for the fixed-source problem.

0.001 sh to a maximum step size of $\Delta t_{\max} = 0.01$ sh, the lumped representation is used for the LO solver in all cells, and the single HO solve has three uniform batches of histories per time step.

For the two material problem, the simulation end time is 2 sh. Table 7.2 compares sample statistics for cell-averaged solutions from the final time step for the two material problem and different numbers of histories per time step. The statistics were generated with 20 independent simulations, for each case. For this problem, there is a slight improvement in statistics with the artificial source approach. A plot of the radiation temperature for the final LO solution is given in Fig. 7.2 for each of the fixups and a reference solution. Each plotted solution is for a single simulation with 120,000 histories per time step. Visually there is agreement between all of the fixup methods.

Table 7.2: Comparison of sample statistics for different HO fixup methods applied to the two material problem. Simulation end time is $t = 2$ sh.

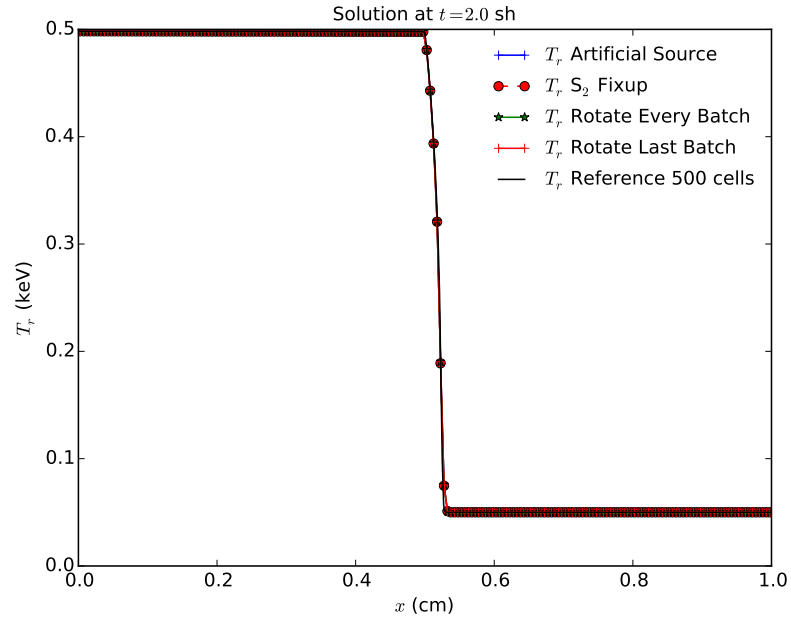
Fixup Method	$\ s\ _{a,rel}$	FOM
30,000 histories per time step		
Artificial Source	0.020%	1.65
S ₂ fixup	0.022%	1.37
Rotate Last Batch	0.021%	1.45
Rotate Every Batch	0.025%	1.00
120,000 histories per time step		
Artificial Source	0.0049%	6.77
S ₂ fixup	0.0055%	5.29
Rotate Last Batch	0.0061%	4.33
Rotate Every Batch	0.0066%	3.67

The process is repeated for the Marshak wave problem with a simulation end time of $t = 5$ sh. Table 7.3 compares sample statistics, and Fig. 7.3 compares LO

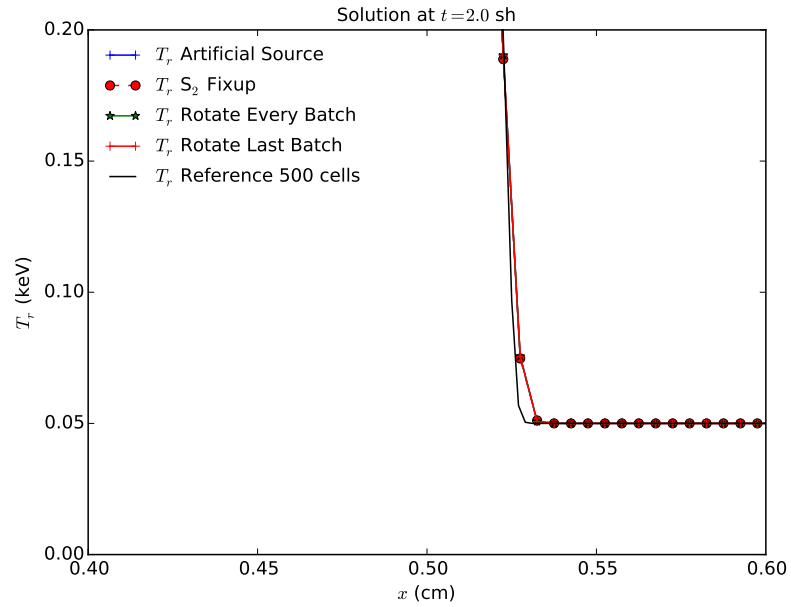
Method	FOM	$\ s\ _{a,rel}$
18,000 histories per time step		
Artificial Source	0.238%	0.89
S ₂ fixup	0.232%	0.93
Rotate Last Batch	0.248%	0.81
Rotate Every Batch	0.224%	1.00
100,000 histories per time step		
Artificial Source	0.050%	3.62
S ₂ fixup	0.047%	4.04
Rotate Last Batch	0.052%	3.31
Rotate Every Batch	0.049%	3.70

Table 7.3: Comparison of sample statistics for different HO fixup methods and the Marshak wave problem. Simulation end time is $t = 5$ sh.

radiation temperatures for the case of 100,000 histories per time step. For this problem, the artificial source method is less statistically efficient. Visually there is a slight dispersion in one cell for the artificial source method. This is caused by the artificial source method introducing extra slope into the solution. The zeroth moment of the intensity can be affected for a finite number of histories. In this case, the extra volumetric source is being sampled and leading to artificial energy propagation down stream. Generally, although locally the stagnation of the residual is being reduced by the added source, there is potential for down stream cells to be affected by under-sampling, decreasing the overall efficiency and accuracy.



(a) Full plot of $T_r(x)$.



(b) Plot of T_r near wave-front.

Figure 7.2: Comparison of cell-averaged radiation temperatures for two material problem and various fixup methods.

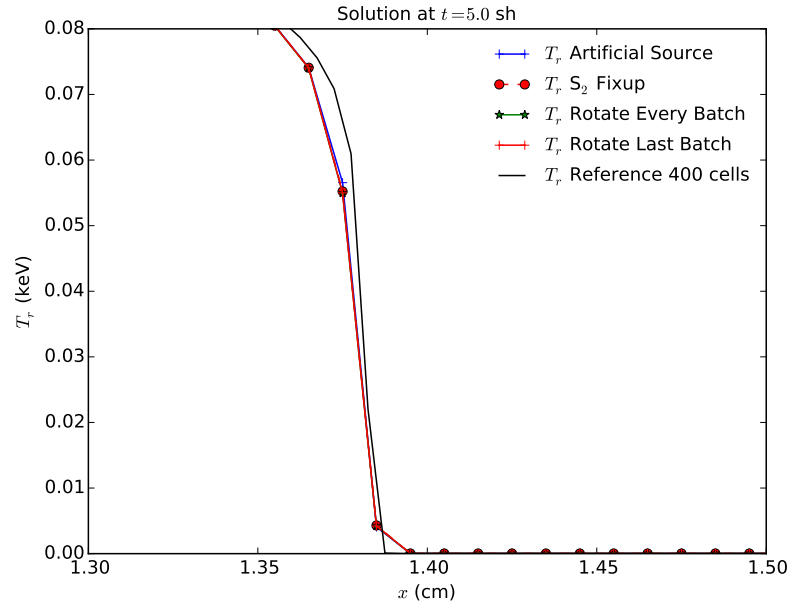
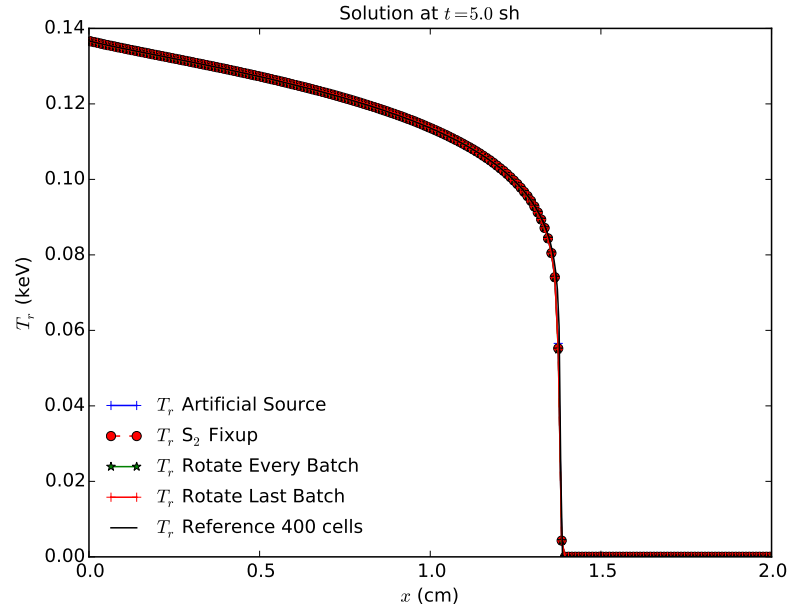


Figure 7.3: Comparison of cell-averaged radiation temperatures for Marshak wave problem and various fixup methods.

8. RESIDUAL MONTE CARLO TREATMENT OF THE TIME VARIABLE

In this chapter, we have modified the time-discrete HOLO method to include higher-accuracy MC treatment of the time variable for the radiation unknowns in the TRT equations. A potential application where this accuracy is important is stellar atmosphere calculations. The ECMC algorithm is modified to include the time variable, allowing for residual MC integration of the time variable. The LO equations are closed in time consistently using a parametric closure derived from the HO equations. The goal is to improve efficiency compared to IMC, while improving the accuracy compared to the time-discrete HOLO algorithm. It is noted that no adaptive refinement in time is performed, so maintaining exponential convergence may not be possible. However, we still expect the residual MC formulation of the ECMC method to show improvement in efficiency over standard MC.

In the remainder of this chapter, modifications to the HOLO algorithm to include higher time accuracy are detailed. First, the inclusion of the time variable into the ECMC trial space is given, along with modifications to the HO algorithm. The process of sampling, tracking, and tallying particle histories in time can be found in literature[18, 7, 12, 37], but sufficient details are provided in this chapter. Then, a new temporal closure for the LO equations is given. Finally, results for the new algorithm are compared to IMC and the time-discrete HOLO method for accuracy and statistical efficiency.

8.1 Modifications to the HO Solver

Inclusion of the time variable t in the trial space used by ECMC allows for no discretization of the transport operator \mathbf{L} . The transport operator, applied to the

continuous intensity I , becomes

$$\mathbf{L}I(x, \mu, t) = \frac{1}{c} \frac{\partial I(x, \mu, t)}{\partial t} + \mu \frac{\partial I(x, \mu, t)}{\partial x} + \sigma_t I(x, \mu, t) \quad (8.1)$$

The emission source is still treated with a BE discretization, which is similar to the approximation made in IMC. Overall, the accuracy in the time variable will be limited by the BE discretized temperature terms, particularly in optically thick regions. However, accuracy in thin regions can be significantly improved.

With this definition of \mathbf{L} and the temperature discretization, the ECMC algorithm specified in Sec. 4.2 is applied, without further modification. However, the residual source and trial-space representation now include t . Each batch is still estimating the error in the current projection estimate $\tilde{I}(x, \mu, t)$, but sampling and tallying of the time variable are included in the MC inversion of the \mathbf{L} operator.

8.1.1 Step Doubly-Discontinuous Trial Space in Time

It is necessary to define a new trial space that includes the time variable to explicitly evaluate the residual. The time variable trial space has a similar representation to the LDD spatial representation in Sec. 3.6.3, but the solution is a constant value over the interior of the time step. This step, doubly-discontinuous (SDD) trial space is defined as

$$\tilde{I}(x, \mu, t) = \begin{cases} \tilde{I}^n(x, \mu) & t = t^n \\ \bar{I}(x, \mu) & t \in (t^n, t^{n+1}) \\ \tilde{I}^{n+1}(x, \mu) & t = t^{n+1} \end{cases} \quad (8.2)$$

where we have used \bar{I} to denote the time-averaged LDFE *projection* in x and μ of the intensity over the interior of the time step; the beginning and end of time step projections are denoted \tilde{I}^n and \tilde{I}^{n+1} , respectively. An illustration of t for the SDD trial space, over the n -th time step, is depicted in Fig. 8.1. There is a projection

error incurred by using the LDFE projection to represent the intensity between time steps. However, with sufficient noise reduction and mesh resolution, this should be an acceptable error compared to potentially large statistical noise of standard MC.

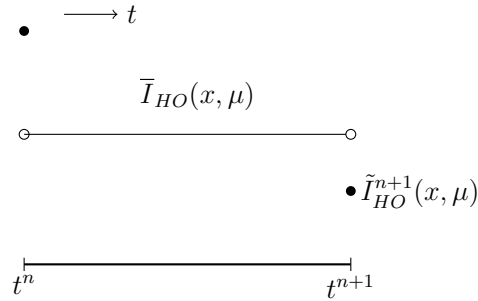


Figure 8.1: Step doubly-discontinuous representation of t for the HO solution.

The SDD trial space provides a projection for all the desired unknowns to exactly reproduce the time-integrated moment equations, i.e., a projection of the time-averaged, end of time step, and previous time step intensities; temporally, these are the only unknowns that appear in equations that have been integrated over a time step to produce a balance statement. Another benefit of this trial space is it allows for infrastructure for computing the residual from the time-discrete case to be used directly. This trial space has one major drawback: only particle histories that reach t^{n+1} contribute to the estimation of $\tilde{\epsilon}^{n+1}$, within a batch. This can be undesirable in optically thick problems. Additionally, the step representation over the interior of the time step may be inaccurate, leading to a reduction in statistical efficiency of the ECMC method.

8.1.2 Residual Source Definition and Sampling

The residual is defined as $r = q - \mathbf{L}\tilde{I}(x, \mu, t)$, where

$$q = \frac{1}{2} (\sigma_a ac(T_{LO}^{n+1})^4(x) + \sigma_s \bar{\phi}_{LO}) \quad (8.3)$$

is constant in time and provided by the LO solver. We have assumed a constant reconstruction for the scattering source in time. Evaluation of the residual with Eq. (8.2) for I produces a uniform source in time, as well as a δ -function source at the beginning and end of the time step. We write the residual source in terms of three components:

$$r(x, \mu, t) = \bar{r}(x, \mu) + r^n(x, \mu)\delta^+(t - t^n) + r^{n+1}(x, \mu)\delta^-(t - t^{n+1}), \quad t \in [t^n, t^{n+1}] \quad (8.4)$$

We will look at each component individually. The first residual term is a constant in time with representation

$$\bar{r}(x, \mu) = q - \mu \frac{\partial \bar{I}(x, \mu)}{\partial x} - \sigma_t \bar{I}(x, \mu) \quad (8.5)$$

Evaluation of the above function produces both face and interior volumetric components (as in the time discrete case), respectively labeled \bar{r}_{face} and \bar{r}_{int} . To sample x and μ from the face and volume distributions, the same rejection procedure is used as for the time-discrete case. The time variable is then sampled uniformly over the time step, i.e., $t = t^n + \eta\Delta t$, where η is a uniform random variable with support $(0, 1)$.

The second source has definition

$$r^n(x, \mu) = -\frac{1}{c} \frac{\partial \bar{I}(x, \mu)}{\partial t} \Big|_{t=t^n} = -\frac{1}{c} \left(\bar{I}(x, \mu) - \tilde{I}^n(x, \mu) \right) \quad (8.6)$$

This source is a LDFF space and angle volumetric source. The rejection sampling procedure is used to sample x and μ . All particles sampled from this source begin tracking with $t = t^n$.

The final source term is

$$r^{n+1}(x, \mu) = -\frac{1}{c} \frac{\partial \bar{I}(x, \mu)}{\partial t} \Big|_{t=t^{n+1}} = -\frac{1}{c} \left(\tilde{I}^{n+1}(x, \mu) - \bar{I}(x, \mu) \right). \quad (8.7)$$

The source r^{n+1} can be treated using the same analytic treatment as the outflow face source in the LDD trial space, as discussed in Sec. 4.5 and derived in App. B.1. The source at the end of the time step is never sampled, because its contribution to I^{n+1} can be analytically computed. To treat the sources this way, the solution for $\tilde{I}^{n+1}(x, \mu)$ is initialized to the value of $\bar{I}(x, \mu)$ before a batch of particles begins. Then, error particles that reach the end of the time step, referred to as “census” particles, contribute a standard score to the projection $\tilde{I}^{n+1}(x, \mu)$.

With these definitions, it is thus only necessary to sample from two sources. We apply the systematic-sampling algorithm described in Sec. 4.3 to determine the number of histories within each cell. The number of histories sampled from each space-angle element is proportional to the magnitude of the residual within that cell, and a minimum number of histories is sampled from cells with a non-zero residual. Then, composite-rejection sampling is used to sampled from the appropriate source. The algorithm for each sample, from x - μ element ij , is

1. Sample two random numbers $\eta_1, \eta_2 \sim U(0, 1)$

2. If $\eta_1 < \|r_{ij}^n\|_1 / (\|r_{ij}^n\|_1 + \|\bar{r}_{ij}\|_1)$:
 - (a) Sample (x, μ) from r_{ij}^n volumetric source using rejection sampling
 - (b) Set $t = t^n$
3. Else, sample from \bar{r}_{ij} source:
 - (a) Sample t uniformly over (t^n, t^{n+1}) .
 - (b) If $\eta_2 < \|\bar{r}_{ij,\text{face}}\|_1 / \|\bar{r}_{ij}\|_1$:
 - Sample (x, μ) from $\bar{r}_{ij,\text{face}}$ face source using rejection
 - (c) Else:
 - Sample (x, μ) from $\bar{r}_{ij,\text{int}}$ volumetric source using rejection

where all L_1 norms are over x - μ domain of element ij . All L_1 integrals can be analytically evaluated using the same numerics as in the time-discrete case because each residual component is either a volumetric or face component.

8.1.3 Importance Sampling on Interior of Time Step

As an attempt to reduce variance in the estimate of $\tilde{\epsilon}^{n+1}(x, \mu)$, importance sampling can be applied to sampling of t for $\bar{r}(x, \mu)$. For particles sampled from $\bar{r}(x, \mu)$, we modify the conditional PDF for sampling a particle start time. The goal is to ensure that some histories reach the end of the time step. In order to do this, we sample from a modified PDF such that a fraction p_{surv} of particles sampled from $\bar{r}(x, \mu)$ are born with $t \in (t^{\text{surv}}, t^{n+1})$. We define $t^{\text{surv}} = t^{n+1} - M / (c\sigma_t)$, where M is the desired number of MFP of travel the particle will undergo from the end of the time step (e.g., 2 or 3). The weights of particles sampled from this distribution must be modified to prevent biasing of the solution. The importance sampling only affects step 3a of the algorithm in the previous section.

The new PDF to be sampled from is

$$f^*(t) = \begin{cases} \frac{1 - p_{surv}}{t^{surv} - t^n} & 0 < t < t^{surv} \\ \frac{p_{surv}}{t^{n+1} - t^{surv}} & t^{surv} \leq t < t^{n+1} \\ 0 & \text{elsewhere} \end{cases} \quad (8.8)$$

The actual PDF is $f(t) = 1/\Delta t$, for $t \in (t^n, t^{n+1})$. Thus, using the standard procedure for importance sampling[16], the starting time t_{start} is sampled from $f^*(t)$, and then particle weights are multiplied by the factor $f(t_{\text{start}})/f^*(t_{\text{start}})$. This procedure is not perfect in that if a particle is moving from an optically thin to an optically thick region, it is not guaranteed to reach census. Additionally, the large variance in the starting weights of particles could increase the variance.

8.1.4 Tracking and Tallying in Time

Because our LO equations will be integrated over the time step, we only need to perform MC tracking for $t \in [t^n, t^{n+1}]$. The initial time for the particle is sampled as described in the previous section. In inverting the \mathbf{L} operator, particles are tracked until they reach the end of the time step. Path lengths are sampled or the weight is exponentially attenuated as before (e.g., Sec. 4.4). As a particle travels from position x_o to x_f , with direction μ , the time is updated as

$$t^f = t^0 + \frac{|x_f - x_o|}{c\mu} \quad (8.9)$$

where c is the speed of light. For analog path-length sampling, if $t^f > t^{n+1}$ then t^f is adjusted to t^{n+1} , and the path length is adjusted accordingly. For continuous weight deposition, particles are only tracked until they reach t^{n+1} . A proof that this process of tracking particles is a MC solution to an integral equation that is exactly inverse

to the \mathbf{L} operator is detailed in literature [37, 16].

Tallies must be adjusted to account for the averaging over the time step, and to compute the intensity at the end of time step. To produce the time-averaged representation $\bar{I}(x, \mu)$, requires estimators for the average, x , and μ moments of the error, e.g.,

$$\bar{\epsilon}_{x,ij} = \frac{1}{\Delta t} \frac{6}{h_j h_i} \int_{t^n}^{t^{n+1}} dt \int_{x_{i-1/2}}^{x_{i+1/2}} dx \int_{\mu_{j-1/2}}^{\mu_{j+1/2}} d\mu \left(\frac{x - x_j}{h_i} \right) \epsilon(x, \mu, t) \quad (8.10)$$

with a similar definition for the average and μ moments. The estimators are defined as

$$\hat{\epsilon}_{x,ij} = \frac{1}{N_{hist}} \frac{6}{\Delta t h_i} \sum_{n=1}^{N_{hist}} \frac{s_n}{h_i h_j} w_j (x_c - x_i), \quad (8.11)$$

where the magnitude of the weights produce the L_1 integral over all phase space, i.e.,

$$\sum_{n=1}^N w_n = \|r(x, \mu, t)\|_1 \equiv \int_{t^n}^{t^{n+1}} dt \int_0^X dx \int_{-1}^1 d\mu |r(x, \mu, t)|. \quad (8.12)$$

Here, x_c is the center of the n -th path length, X is the width of the domain, and s_n is the path length for the n -th path length in the x - μ cell. As in the time-discrete case, in the simulation we normalize weights to unity and multiply tally results by the L_1 norm of the residual, and tallies are modified to account for continuous weight deposition.

Moments of $I^{n+1}(x, \mu)$ must be estimated to produce a projection of the intensity at the end of the time step. For example, the x moment for the ij -th cell of the error at the end of time step is

$$\epsilon_{x,ij}^{n+1} = \frac{6}{h_i h_j} \iint_{\mathcal{D}_{ij}} \left(\frac{x - x_i}{h_i} \right) \epsilon(x, \mu, t^{n+1}) dx d\mu \quad (8.13)$$

The estimators for these moments are a generalization of the census tallies used in IMC [18, 12]. These tallies estimate moments based on the point-wise spatial distribution of particles at a particular time. They are based on the definition of the intensity as $I(x, \mu, t) = ch\nu N(x, \mu, t)$ given in Eq. (1.1), similar to collision estimators [16, 17]. The census estimator for the x moment is

$$\hat{\epsilon}_{x,ij}^{n+1} = \frac{1}{N_{hist}} \frac{6}{h_j h_i^2} \sum_{n=1}^{N_{hist}} c w_j (x_n - x_i), \quad (8.14)$$

where x_n is the location of the n -th particle that has reached the end of the time step. Similar tallies are defined for the other space-angle moments. These tallies can be exceptionally noisy because only particles that reach the end of the time step contribute.

8.2 Closing the LO Equations in Time

The closure of the LO equations must be modified to account for inconsistencies in the time-discretization of the two solvers. Previous work has enforced consistency in time by adding a local artificial source to the time-discretized LO equations in each cell [3]. This source was approximated based on the difference between the exact HO integral of the time derivative and the approximate representation in the LO equations. The advantage of this form is that the LO solver exclusively deals in time-averaged unknowns for the radiation terms in the equations. We will alternatively use a parametric closure in the time variable, similar to the spatial closures discussed in Sec. 3.6.

After applying a parametric closure, the time-integrated LO equations can be written exclusively in terms of time-averaged unknowns. Once the time-averaged unknowns have been calculated, the time closures can be used to convert the time-

averaged unknowns to end-of-time-step values, for the next time step.

8.2.1 Derivation of Time-Averaged Moment Equations

The time-continuous radiation equations are integrated in space and angle the same as in the time-discrete case. The equation resulting from application of the L and $+$ moment operators is

$$\begin{aligned} & \frac{1}{c} \frac{\partial}{\partial t} h_i \langle I(x, \mu, t) \rangle_L^+ - 2 (\mu I(x_{i-1/2}, \mu, t))^+ + \langle \mu I(x, \mu, t) \rangle_{L,i}^+ + \langle \mu I(x, \mu, t) \rangle_{R,i}^+ \\ & + \sigma_{t,i} h_i \langle \phi(x, t) \rangle_{L,i}^+ - \frac{\sigma_{s,i} h_i}{2} (\langle \phi^+(x, t) \rangle_{L,i} + \langle \phi^-(x, t) \rangle_{L,i}) = \frac{h_i}{2} \langle \sigma_a a c T^4(x) \rangle_{L,i} \quad (8.15) \end{aligned}$$

This equation is then integrated over the time step, and the emission source is approximated with a BE discretization. The manipulations in Sec. 3.1.4 are performed on the streaming term to form angular consistency terms, but the weighting fluxes are now time-averaged values. Thus, the angular consistency terms are evaluated with $\bar{I}(x, \mu)$. The final moment equation is

$$\begin{aligned} & \frac{\langle \phi \rangle_{L,i}^{+,n+1} - \langle \phi \rangle_{L,i}^{+,n}}{c \Delta t} - 2 \bar{\mu}_{i-1/2}^+ \bar{\phi}_{i-1/2}^+ + \overline{\{\mu\}}_{L,i}^+ \langle \bar{\phi} \rangle_{L,i}^+ + \overline{\{\mu\}}_{R,i}^+ \langle \bar{\phi} \rangle_{R,i}^+ + \sigma_{t,i}^{n+1} h_i \langle \bar{\phi} \rangle_{L,i}^{n+1,+} \\ & - \frac{\sigma_{s,i} h_i}{2} (\langle \bar{\phi} \rangle_{L,i}^+ + \langle \bar{\phi} \rangle_{L,i}^-) = \frac{h_i}{2} \langle \sigma_a^{n+1} a c T^{n+1,4} \rangle_{L,i}, \quad (8.16) \end{aligned}$$

where over-barred quantities are averaged over the time step. The L and $+$ consistency term is

$$\overline{\{\mu\}}_{L,i}^+ \equiv \frac{\frac{2}{h_i \Delta t} \int_{t^n}^{t^{n+1}} \int_0^1 \int_{x_{i-1/2}}^{x_{i+1/2}} \mu b_{L,i}(x) I(x, \mu, t) dx d\mu dt}{\frac{2}{h_i \Delta t} \int_{t^n}^{t^{n+1}} \int_0^1 \int_{x_{i-1/2}}^{x_{i+1/2}} b_{L,i}(x) I(x, \mu, t) dx d\mu dt}. \quad (8.17)$$

For the material energy equations, the BE approximation is used for the temperature terms, but the radiation energy deposition is a time-averaged valued. As before, it is necessary to introduce the LDFE representation for $T(x)$ and $T^4(x)$. The new temperature equation is

$$\begin{aligned} \frac{\rho_i c_{v,i}}{\Delta t} \left[\left(\frac{2}{3} T_{L,i} + \frac{1}{3} T_{R,i} \right)^{n+1} - \left(\frac{2}{3} T_{L,i} + \frac{1}{3} T_{R,i} \right)^n \right] + \sigma_{a,i}^{n+1} (\langle \bar{\phi} \rangle_{L,i}^+ + \langle \bar{\phi} \rangle_{L,i}^-) \\ = \sigma_{a,i}^{n+1} a c \left(\frac{2}{3} T_{L,i}^4 + \frac{1}{3} T_{R,i}^4 \right)^{n+1}, \quad (8.18) \end{aligned}$$

where cross sections remain implicit. Analogous equations can be derived for $\mu < 0$ and the R moment.

The only approximation introduced up to this point is the BE and LDFE spatial representation for temperature terms. As before, we will use a LDFE closure to eliminate the face terms from the radiation moment equations. The angular consistency terms are evaluated with the previous time-averaged HO solution (based on the linearity of the integral operators), e.g.,

$$\overline{\{\mu\}}_{L,i}^+ \simeq \frac{\frac{2}{h_i} \int_0^1 \int_{x_{i-1/2}}^{x_{i+1/2}} \mu b_{L,i}(x) \bar{I}_{HO}(x, \mu) dx d\mu}{\frac{2}{h_i} \int_0^1 \int_{x_{i-1/2}}^{x_{i+1/2}} b_{L,i}(x) \bar{I}_{HO}(x, \mu) dx d\mu}. \quad (8.19)$$

8.2.2 Parametric Time Closure

The end of time-step radiation unknowns, e.g., $\langle \phi \rangle_{L,i}^{n+1}$, must be eliminated from the system. A different closure relations is required for the time variable than for the spatial variable because the HO solver does not estimate the first moment in the

time variable. The following closure is a modified diamond relation:

$$I^{n+1} = 2\gamma^n \bar{I} - I^n \quad (8.20)$$

where γ^n is the closure factor and \bar{I} is the time-averaged intensity. A modified BE discretization can also be used:

$$I^{n+1} = \gamma^n \bar{I} \quad (8.21)$$

The chosen closure relation must be used to eliminate the unknowns at t^{n+1} from each of the LO moment equations, with the values from the previous time step taken as a known quantity. Thus, it is necessary to have a closure relation for each moment and half range, producing four closure parameters per spatial cell. The closure relations for the L moment and the modified diamond relation are

$$\langle \phi \rangle_{L,i}^{\pm,n+1} = 2\gamma_{L,i}^{n,\pm} \langle \bar{\phi} \rangle_{L,i}^{\pm} - \langle \phi \rangle_{L,i}^{\pm,n} \quad (8.22)$$

with equivalent definitions for the R moment. Substitution of the above equation into Eq. (8.16), with the LDFE spatial closure, produces

$$\begin{aligned} \frac{2h_i}{c\Delta t} [\gamma_{L,i}^{n,+} \langle \phi \rangle_L^{+,n+1} - \langle \phi \rangle_L^{+,n}] - 2\bar{\mu}_{i-1/2}^+ [2\langle \phi \rangle_{R,i-1}^+ - \langle \phi \rangle_{L,i-1}^+] \\ + \overline{\{\mu\}}_{L,i}^+ \langle \bar{\phi} \rangle_{L,i}^+ + \overline{\{\mu\}}_{R,i}^+ \langle \bar{\phi} \rangle_{R,i}^+ + \sigma_{t,i}^{n+1} h_i \langle \bar{\phi} \rangle_{L,i}^+ - \frac{\sigma_{s,i} h_i}{2} (\langle \bar{\phi} \rangle_{L,i}^+ + \langle \bar{\phi} \rangle_{L,i}^-) \\ = \frac{h_i}{2} \langle \sigma_a^{n+1} acT^{n+1,4} \rangle_{L,i}, \quad (8.23) \end{aligned}$$

The other moment equations are analogously defined. The value of $\gamma_{L,i}^{n,+}$, $\gamma_{R,i}^{n,+}$, $\gamma_{L,i}^{n,-}$, and $\gamma_{R,i}^{n,-}$ can be computed by substituting the trial-space representation of $I^{HO}(x, \mu, t)$ into Eq. (8.22) and its analogs.

8.3 Computational Results

The HOLO method with high-order time closure was tested for several representative problems. Throughout this section, for the HOLO method, results that use the backward Euler discretization are indicated with HOLO-BE, and results with the MC-based time closure are indicated with HOLO-TC, where applicable. For simplicity, all HOLO results have used the lumped-relation in the LO radiation moment equations to preserve positivity. We will compare sample statistics and accuracy against IMC simulations.

8.3.1 Near-Void Problem

For the first problem, the material properties are uniform throughout a 2.0 cm wide domain with $\rho c_v = 0.01374 \text{ Jks cm}^{-3} \text{ keV}^{-1}$, $\sigma_a = 10^{-6} \text{ cm}^{-1}$, and $\sigma_s = 0 \text{ cm}^{-1}$. The material and radiation are initially in equilibrium at a temperature of 0.01 keV. An isotropic incident intensity with $T_r = 0.150 \text{ keV}$ is applied at $x = 0$ for $t > 0$; the incident intensity on the right boundary is 0.01 keV. The simulation end time is 0.003 sh.

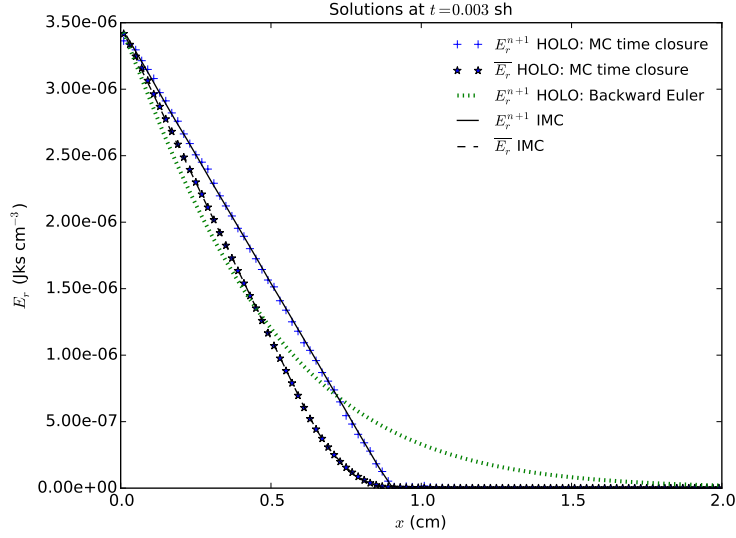


Figure 8.2: Comparison of radiation energy densities of IMC and HOLO method for the HO time closure and a BE discretization.

A comparison of the cell-averaged radiation energy densities E_r for IMC and the HOLO method with the diamond-like HO time closure are depicted in Fig. 8.2, both for the time-averaged solutions and end-of time step values, from the final time step. The end of time step value for the HOLO method with a BE discretization is also depicted. For the HOLO results, three ECMC batches were performed with a total of 3×10^6 histories per time step and the IMC results were generated with 12×10^6 histories per time step; all IMC results in this section used $\Delta t = 0.001$ sh. The minimum number of histories for any sampled space-angle cell, N_{\min} in Eq. (4.18), is 20 for all HOLO simulations. The spatial meshes had 100 spatial cells and both HOLO results used 20 μ cells. The MC treatment of the time variable and the closure of the LO equations allow the LO results to correctly reconstruct the wave-front location of IMC, whereas the BE discretization artificially propagates energy. Although not plotted, the results were visually equivalent for either the diamond-

like or implicit-like closures in this problem. This is because the problem is nearly linear due to the small cross sections, so the HO moments are reproduced accurately, independent of the chosen closure equation.

A comparison of the same results depicted as radiation temperatures is given in Fig. 8.3. By plotting proportional to the fourth-root of the radiation energy density, the noise at low magnitudes past the wave-front are more apparent in the 3 batches and $\Delta t = 0.001$ case. This noise is small relative to the scale of E_r , but it demonstrates a deficiency of the trial space. The step representation over the time step leads to particles sampled near the wave-front with a time near t^n that travel into the equilibrium region. This is not a bias but rather an under-sampling of the phase space; if sufficient histories were performed there would be negative particles that canceled out this error. The ECMC iterations can lead to negative averages in the HO solution out front of the wave front. In such cells, the average was set to the floor value and slopes to zero. This effect is significantly reduced when a smaller time step is taken, although the projection error is increased.

For the case of a single batch, there is less noise past the wavefront because the choice of $I^n(x, \mu)$ as an initial guess for $I^{n+1}(x, \mu)$ prevents most particles from traveling past what the physical transport should allow. The discrepancy between the IMC and the single batch HOLO solution near the foot of the wave is a result of the spatial discrepancy between the LDFE HO projection and the lumped LD LO equations; this dispersion is not present in the HO solution. This discrepancy can also lead to some negativities in the LD edge values of $\phi^{n+1}(x)$, which are set to the floor value for the next time step.

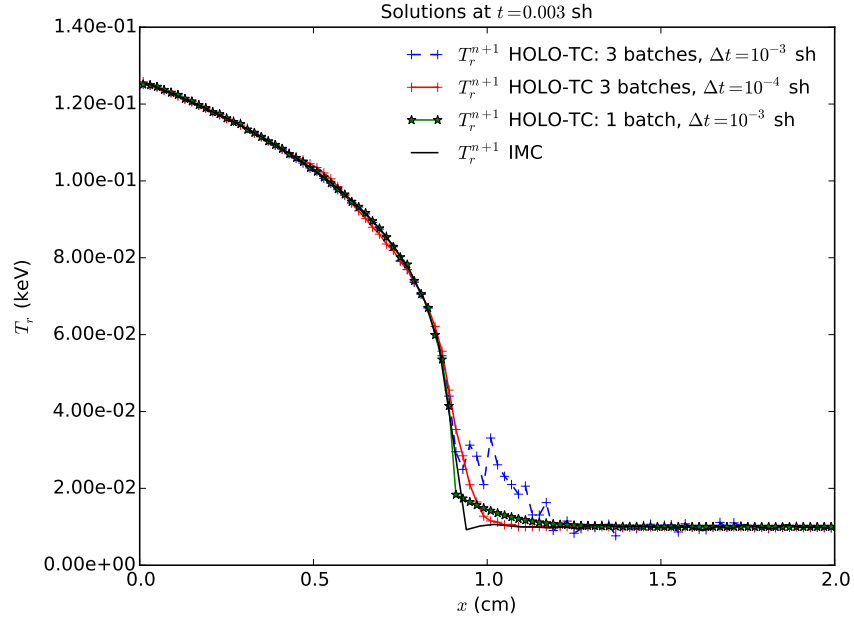


Figure 8.3: Comparison of radiation temperatures of IMC and the HOLO method for different time step sizes and numbers of batches, for the near-void problem.

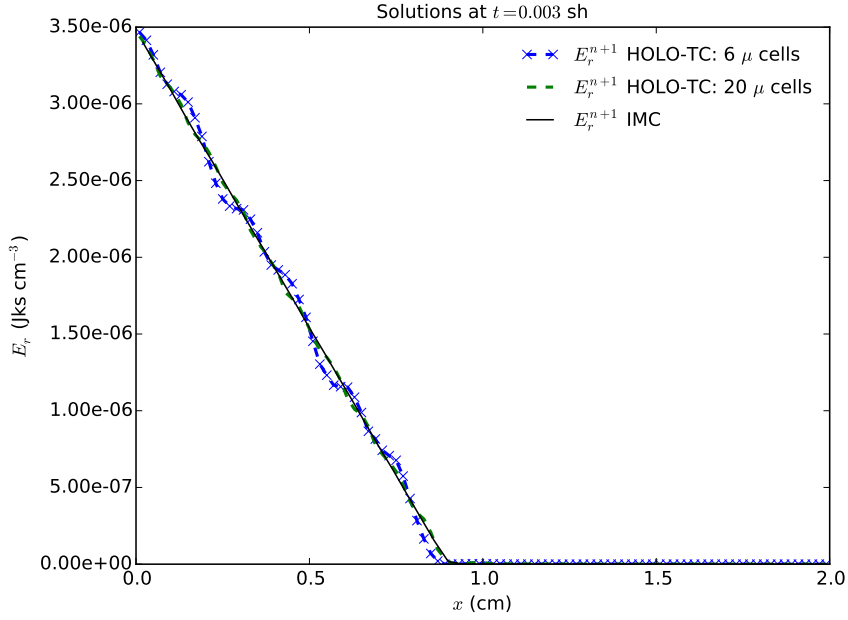


Figure 8.4: Comparison of radiation energy densities for the HOLO method with different numbers of μ cells, for the near-void problem; $\Delta t = 0.001$ sh.

Figure. 8.4 compares radiation energy densities for various numbers of μ cells. At coarser mesh sizes, the imprinting of the mesh is visible in the location of the wave-front. This is a result of the projection onto the space-angle mesh between time steps. As the mesh is refined, the solution converges towards the IMC solution. Smaller time step sizes can increase the mesh imprinting because the projection onto the trial space happens more often. However, it is important to note that this problem is a limiting case; the mesh imprinting will be reduced as σ_a is increased and absorption-emission events smooth the angular intensity across each time step.

8.3.2 Optically Thin Problem

We modify the previous problem by increasing the absorption cross section to 0.2 cm^{-1} ; all other problem parameters are the same. Radiation temperatures at the end of the last time step are compared for IMC, HOLO-TC, and HOLO-BE in

Fig. 8.5. The HOLO-TC and HOLO-BE results were generated with 30μ cells, and all spatial meshes used 100 cells. All results used 3×10^6 histories per time step. At smaller time step sizes, the effects of mesh imprinting are visually apparent in the HOLO-TC results, leading to more dispersion near the wave-front. There is good agreement between the HOLO-TC results and IMC, except some dispersion near the wavefront. As in the previous problem, the HOLO-BE results are very inaccurate at capturing the wavefront location. IMC demonstrates substantial statistical noise in the equilibrium region.

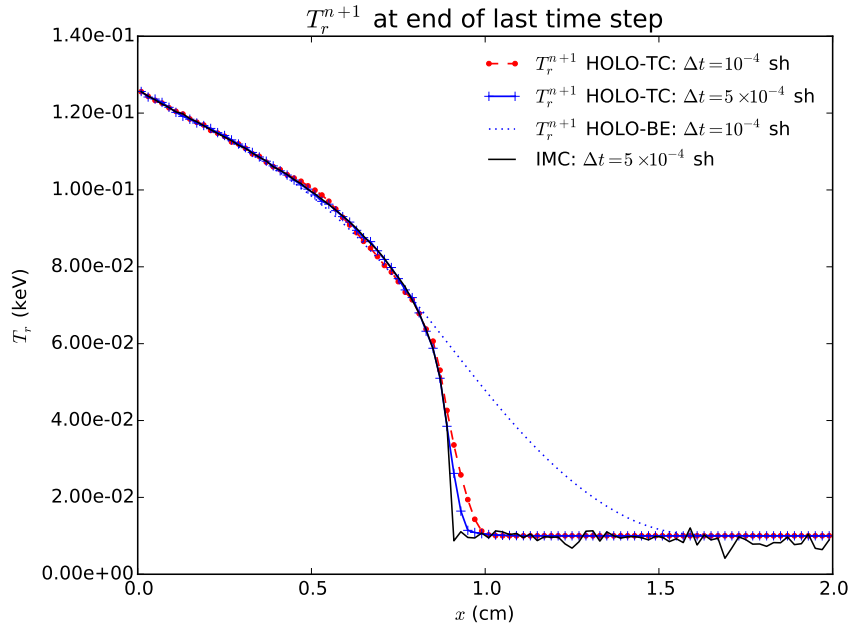


Figure 8.5: Comparison of radiation temperatures of IMC and the HOLO method for different time step sizes and numbers of batches, for optically thin problem.

The accuracy of the HOLO-TC and IMC method were compared against a reference IMC solution. Because the material is loosely coupled in this problem we expect IMC to be accurate with sufficient particle histories. The reference solution is the

average of 20 IMC simulations of 20×10^6 histories, each with $\Delta t = 10^{-4}$ sh. The estimated value of $\|s\|_{a,rel}$ for the reference solution is 0.025%. The discrete norm of the error in cell-averaged mean intensities $\|e\|_{a,rel}$ is computed using Eq. (5.8) for ϕ^{n+1} from the last time step, averaged over 20 simulations. Sample statistics for cell-averaged ϕ^{n+1} were also computed using the FOM from Eq. (5.3).

Table. 8.1 compares computed values of $\|e\|_{a,rel}$ and FOM for the census radiation energy densities, for the case of $\Delta t = 0.0005$ sh. HOLO results were generated for the case of 1 and 2 batches, with the same total number of histories per time step, where the number of batches is indicated in parenthesis. The standard deviation of each estimate of $\|e\|_{a,rel}$ follows each value in parenthesis. At low particle counts, the HOLO-TC method demonstrates substantial noise. A plot of the inaccuracies for the case of 30,000 histories and a single batch is given in Fig. 8.6. As demonstrated, statistical noise in the estimate of \tilde{I}^{n+1} introduce instabilities into the LO result. This is due to the trial space representation of the census particles at the end of the time step being poorly estimated. For the 2 batch case, there is less error in the estimate of $\tilde{I}^{n+1}(x, \mu)$ because only the deviation from the first batch estimate of $\bar{I}(x, \mu)$ is estimated with MC. At higher history counts there is an increase in efficiency, however the IMC method is more accurate overall due to the projection error between time steps. For reference, statistics were measured for the HOLO-BE method with two batches of 150,000 histories per time step, producing $\|e\|_{a,rel} = 10.5\%$ and FOM = 3100, demonstrating substantial inaccuracy but improved efficiency.

Table 8.2 compares results for $\Delta t = 0.0001$ sh. The results were generated for two different mesh sizes, but $\|e_{a,rel}\|$ is computed using the same 100 spatial cell reference solution in both cases. All FOM values are relative to *IMC* with 100 x cells and 30,000 histories. At the coarser mesh size, the HOLO-TC method has a factor of 95 higher FOM, indicating much-improved statistical efficiency. However,

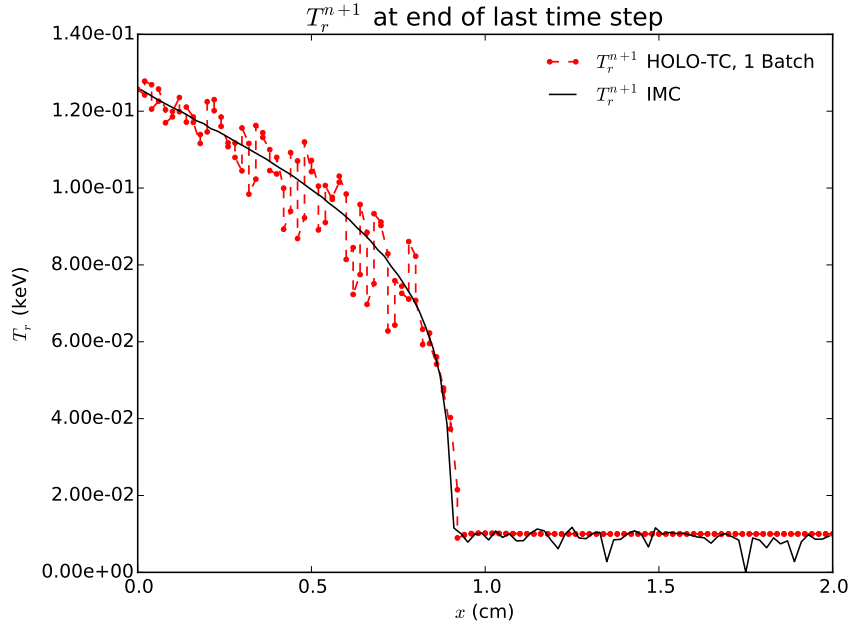


Figure 8.6: Comparison of T_r^{n+1} for 30,000 histories per time step. The HOLO-TC result has insufficient histories to accurately estimate end of time step unknowns.

the projection error limits accuracy to around 1.5%. At the finer mesh size, the HOLO-TC method remains more efficient (as long as the batch size is sufficient) and produces higher accuracy than the IMC results. For reference, statistics were measured for the HOLO-BE method with two batches of 150,000 histories per time step. The HOLO-BE results produced $\|e\|_{a,rel} = 3.7\%$ and $FOM = 4700$ for the coarse mesh, and $\|e\|_{a,rel} = 3.6$ and $FOM = 9600$ for the fine mesh. The accuracy of the HOLO-BE method is limited by the time integration accuracy.

Table 8.1: Comparison of accuracy and FOM for the end of time step radiation energy densities, of the last time step, for the optically thin problem and $\Delta t = 5 \times 10^{-4}$ sh. Simulation end time is $t = 0.003$ sh.

hists./step	$\ e\ _{a,rel}$			FOM		
	IMC	HOLO-TC (1)	HOLO-TC (2)	IMC	HOLO-TC(1)	HOLO-TC(2)
30,000	3.0% (0.08%)	17.3% (0.5%)	4.99% (0.2%)	1.00	0.03	0.31
300,000	1.0% (0.02%)	1.1% (0.02%)	1.13% (0.02%)	0.93	1.38	1.65
1,000,000	0.5% (0.01%)	0.92% (0.01%)	0.96% (0.01%)	1.10	3.42	2.0

Table 8.2: Comparison of accuracy and FOM for the end of time step radiation energy densities, of the last time step, for the optically thin problem and $\Delta t = 1 \times 10^{-4}$ sh. The reference results are all for 100 x cells. Simulation end time is $t = 0.003$ sh.

hists./step	$\ e\ _{a,rel}$		FOM	
	IMC	HOLO-TC (1)	IMC	HOLO-TC(1)
Results for 100 x cells; HOLO-TC has 30 μ cells				
30,000	2.98% (0.09%)	1.49% (0.02%)	1.00	42.0
300,000	0.96% (0.02%)	1.45% ($< 0.01\%$)	0.98	94.5
1,000,000	0.49% (0.01%)	1.45% ($< 0.01\%$)	1.11	94.9
Results for 200 x cells; HOLO-TC has 60 μ cells				
30,000	2.93% (0.1%)	14.00% (0.4%)	0.49	0.05
300,000	0.99% (0.03%)	0.37% ($< 0.01\%$)	0.45	6.98
1,000,000	0.49% (0.01%)	0.18% ($< 0.01\%$)	0.50	40.04

8.3.3 Marshak Wave Problem

It is important to demonstrate that the time closures are stable in a mix of optically thick and optically thin regions, and that the ECMC method is still efficient in such problems. Simulations were performed for the Marshak wave problem defined in Sec. 5.2. The time step size is linearly increased from 0.001 sh to a maximum step of 0.01 sh over the first 10 time steps; the last time step is adjusted to reach the desired simulation end time. It was found for this problem that it was necessary to use more than one batch for the HOLO-TC algorithm to stably converge, for the same reasons inaccuracies were demonstrated in the previous section.

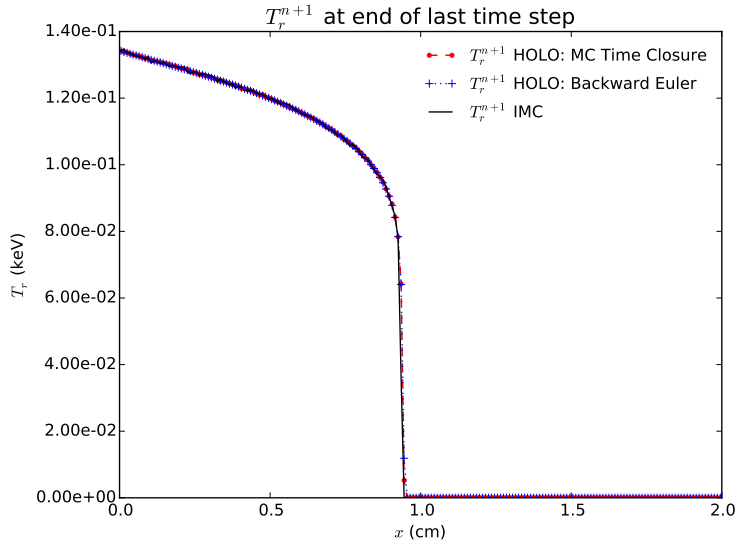


Figure 8.7: Comparison of HOLO-TC, HOLO-BE, and IMC methods for the Marshak Wave problem, with 10^6 histories per time step.

Figure 8.7 compares the accuracy of IMC, HOLO-TC, and HOLO-BE. These results were generated using the implicit-like time closure. The solutions are plotted at $t = 3$ sh, with 10^6 histories per time step for all simulations. As demonstrated, there

is good agreement among the results. It is noted that this problem can be accurately modeled with the Backward Euler time discretization, but the MC time closure appears to be stable even in the mix of optically thick and thin regions. Table 8.3 compares sample statistics for IMC, the HOLO-TC method with the implicit-like and diamond-like closures, and the HOLO-BE method. As demonstrated, at the lower history count (300,000), the HOLO-TC algorithm demonstrates a greater variance than IMC, but is more efficient at the higher batch size. The HOLO-BE method is significantly more efficient for comparable accuracy in this problem with a very optically thick region.

Table 8.3: Comparison of sample statistics for the end of time step radiation energy densities, of the last time step, for the Marshak wave problem and maximum time step of 0.01 sh. Simulation end time is $t = 3.0$ sh.

	$\ s\ _{a,rel}$			FOM		
hists./step	IMC	HOLO-TC (2)	HOLO-BE (2)	IMC	HOLO-TC (2)	HOLO-BE (2)
HOLO-TC using Implicit-Like Closure						
300,000	2.25%	3.42%	0.30%	1.00	0.43	2050
1,000,000	1.27%	0.31%	0.17%	0.94	15.95	1806
HOLO-TC using Diamond-Like Closure						
300,000	–	3.53%	–	–	0.41	–
1,000,000	–	0.37%	–	–	10.94	–

8.3.3.1 Importance Sampling on Interior of the Time Step

The importance sampling algorithm detailed in Sec. 8.1.3 was investigated for the Marshak wave problem. In particular, various values of p_{surv} with a fixed value of 2 MFP of survival distance were investigated. Sample statistics were measured

for the HOLO-TC algorithm and the case of two batches of 100,000 histories per time step, with a max time step size of 0.01 sh. The importance sampling algorithm was found to generally increase the variance for this problem. This is likely caused by the fact that when no importance sampling is used, in the very thick cells essentially no particles reach the census. In such cells, because the ECMC algorithm is estimating the difference between the first batch's estimate of $\bar{I}(x, \mu)$ and $\tilde{I}^{n+1}(x, \mu)$, it just accepts $\bar{I}(x, \mu)$ as $I^{n+1}(x, \mu)$. The initialization of the solution to the first batches estimate of $\bar{I}(x, \mu)$ is sufficient to produce visually accurate results because the problem is evolving slowly, although this a biased result due to under-sampling of the phase space. When importance sampling is used, then more particles reach the census, increasing variance overall. If too many particles are sampled near the end of the time step, then the variance of the time-averaged solution increases, decreasing accuracy over all.

Table 8.4: Comparison of sample statistics using importance sampling on the interior of the time step, for the Marshak Wave problem. Simulation end time is $t = 1.0$ sh and max Δt is 0.01 sh.

p_{surv}	FOM
No Bias	1
0.05	0.001
0.1	0.005
0.25	0.179
0.5	0.003

9. CONCLUSIONS AND FUTURE WORK

9.1 Conclusions

We have implemented and tested a new HOLO algorithm for 1D, grey TRT problems. The HO solver utilizes ECMC, and the LO system is based on half-range angular moments and LDFE spatial moments. Overall, the LO solver can accurately and efficiently resolve the solution in diffusive regions, while the HO transport solver provides the accuracy of a full transport treatment where necessary. Our HOLO method produces accurate solutions for Marshak wave test problems that are in agreement with IMC. Unlike IMC, our method requires no effective scattering events to be included in the MC simulation, which limits the run time of particle tracking, while adding the cost of a LO Newton solver. The LDFE spatial representation mitigates issues with teleportation error, producing results with spatial accuracy that is better than IMC with source tilting at coarser meshes. The LDFE discretization of the LO system and material temperature was also shown to preserve the equilibrium diffusion limit. The efficiency of the LO system allows for nonlinearities in the system to be resolved with Newton iterations. The fully nonlinear system with an implicit discretization prevents maximum principle violations. Even though damping of the Newton iterations was required for convergence to prevent violations, an advantage of the HOLO method is that there is no additional cost for the HO solution when the damped method is used. Typically, the HO solver will be the most expensive portion of the algorithm. We have also implemented iterative solution methods to the LO equations using the GMRES and standard source iteration approaches. A nearly-consistent DSA method was able to significantly reduce the number of required scattering iterations for the source iteration approach.

The ECMC algorithm was shown to be more statistically efficient than standard MC as a HO solver for TRT problems. The residual formulation with an initial guess based on the previous radiation intensity results in efficient reduction of statistical error. Overall, the ECMC algorithm is more effective than standard MC in the HOLO context where it is necessary to accurately estimate the angular intensity globally to produce consistency terms in each spatial cell. The systematic source sampling algorithm distributes particles to regions of the problem where the solution varies greatly over the time step. For problems where the LDFE space-angle trial space can reasonably approximate the solution, mesh refinement allows for exponential convergence and improved FOM values. In problems with optically thick regions and strong solution gradients, the residual formulation of ECMC can still improve efficiency throughout the domain. Once a maximum refinement level has been achieved and the error has stagnated, the final batch of particle histories can be extended to increase statistical accuracy in the final estimate of the error, but at the standard MC convergence rate. Fixups for the HO solver based on rotating negative solutions to produce a positive solution were investigated. With a positive representation of the intensity, the LO solutions were found to be stable and accurate for the problems tested. The addition of an artificial source was found to be inaccurate, due to the effects it had on the solution in down stream cells. Generally, local modifications to the residual are ineffective due to the effect on other regions of the problem. However, at least for the problems tested, even with rapid stagnation the residual formulation of ECMC leads to high statistical efficiency.

The linear doubly-discontinuous (LDD) trial space was introduced to estimate the HO solution at faces, allowing for a parametric spatial closure of the LO equations. For problems where the LD trial space can reasonably resolve the solution, a HO spatial closure was able to increase discrete consistency between the HO and LO

solutions and improve accuracy in the L_2 norm. The accuracy for cell-averaged mean intensities was not improved due to the additional statistical noise in the face tallies and inaccuracies in the HO moment equations for the ECMC solver because of the residual formulation. In problems where the solution is not resolved by the LD representation, the inconsistencies in the first moment for the HO solver and the lumped LD LO equations make the spatial closure ineffective and unstable. In higher dimensions, preserving the spatial accuracy of the HO solution method may demonstrate a greater accuracy than 1D where the LD spatial closure is third-order accuracy in the averages. However, the closure is fundamentally limited in accuracy in diffusive problems because of the requirement of a linear closure for $T(x)$ and $T^4(x)$.

We have also demonstrated the ability to extend the HOLO algorithm to continuous treatment of the time variable for radiation terms. The SDD trial space in the time variable allows for the transport operator to be inverted continuously in the ECMC algorithm. This improves accuracy for the radiation energy density in optically thin region compared to a full BE discretization. The parametric LO closure preserves the accuracy of the HO treatment in the LO moments, with comparable accuracy for a diamond-like and implicit-like closure. A particular benefit of the time closure is that \bar{I}^{HO} is most different from $I^{HO,n+1}$ in problems that are optically thin. In such problems, the problem is relatively linear, so the closure can. However, in optically thick problems, inaccuracies in the SDD for estimating I_{HO}^{n+1} leads to an increase in the required number of histories for convergence. In thick problems, the diamond-like closure can introduce instabilities because of the initial solve in a time step using CN and statistical noise.

9.2 Future Work

For the HO solver, extension to higher dimensions is a great task. The main hurdle to overcome is infrastructure. In particular, the greatest difficulty is a FE, functional representation in all phase space variables and the ability to track on such a FE mesh; for 2D grey problems this is a four-dimensional FE space. This required technology is fundamentally different than the approach in most S_N methods. Recently, locally-adaptive angular quadratures, based on quadrilateral finite-elements in angle, have been developed [47]. The underlying basis functions of the quadrature sets could be used for the angular trial space, but the quadratures are far from being the mature technology needed for our method.

Another difficult issue for our algorithm is when the solution cannot be accurately represented by the trial space, e.g., in optically thick cells where the solution is driven negative. The ability to represent the solution accurately in rapidly varying regions of the problem will be key for generalization of this method to higher dimensions. In higher dimensions, there will likely be more regions that are difficult to resolve due to strong spatial gradients resulting from shadowing effects in mixed optically thick and thin regions. The artificial source approach was not generally affective, but presents one possible approach to mitigate stagnation. However, a more desirable method is one that ensures the closure in the LO system is consistent with the HO representation for the solution in such regions. The HO spatial closure was ineffective in difficult problems primarily because of inconsistencies in the first moment between the HO and LO equations.

It is necessary to introduce a fixup method that corrects the first moment equation in the HO solution and LO solution consistently, but will not affect energy conservation of the LO equations. A fundamental problem with the lumping rela-

tion for the LO solution is that the linear reconstruction of the emission source does reproduce the first moment determined by the LO moment equations. Additionally, the first moments of the intensity and outflows as estimated with ECMC are not consistent with the corresponding lumped LO moment equations. This inconsistency produces instabilities when the HO spatial closure was introduced. A strictly positive trial space representation is likely necessary, although this may be difficult to extend to higher dimensions and introduces additional computational complexity. A straight-forward approach would be to apply slope limiters to the temperature and LD representation of the intensity in the HO and LO equations, although this may lead to artificial diffusivity of the solution on coarser meshes and convergence issues.

To extend to higher dimensions, our LDFE representation may require the use of a higher-degree spatial representation for the LO system to achieve the diffusion limit. Further asymptotic analysis on the method will be applied before implementation. It may be necessary to use a different LO system (e.g., the non-linear diffusion acceleration approach in [1]), if the S_2 -like equations become too inefficient or difficult to implement in higher dimensions. Although accelerated iterative solution technique with DSA was demonstrated. Alternatively, a variable Eddington Tensor approach may provide more stability in rapidly variable regions of the problem while still allowing for a consistent, LDFE solution that is efficiently solvable. Additionally, future studies should investigate the stability of the S_2 -like LO closures more rigorously using a linear Fourier stability analysis.

The HO treatment of the time variable could be improved by replacing the SSD trial space with an LDFE representation in the time variable. The linear representation should produce less statistical noise in the end of time step intensity because all particle tracks contribute to the slope for each element, rather than just those that reach the end of the time step. However, this trial space would produce a pro-

jection error for the end of time step intensity based on a linear extrapolation. The linear representation in time would also produce a more accurate reconstruction of the scattering source temporally.

However, a linear representation in t requires the sampling algorithm to be significantly modified because the L_1 integrals for computing the residual magnitude are now significantly complicated by the tri-linear function. In particular, the integrals over the interior of the phase-space element when the residual crosses zero can no longer be analytically evaluated. It may be necessary to incorporate importance sampling or potentially Markov Chain MC to sample this function [16]. One potential path forward is to use an importance sampling method for determining the number of particle histories in each x - μ - t element, where the sampling function $f^*(x, \mu, t)$ is a PDF for the residual resulting from a step representation of the solution. The magnitude of the step representation of the residual can be exactly integrated with quadrature to form the PDF. In such an approach, the magnitude of the true residual source is being approximated with MC through particle weights, e.g., $w(x, \mu, t) = r(x, \mu, t)/f^*(x, \mu, t)$ (this is similar to the method referred to as self-normalizing importance sampling). Because ECMC is not conservative anyways, the statistical error in the magnitude of the residual should be acceptable for most problems. The goal of such an approach is that the step residual will be sufficiently close to the true residual, with sufficient mesh resolution, to be more statistically efficient than a simpler approach, e.g., sampling from a uniform function over all phase-space. Quadrature approximation to the L_1 norms of the residual may be more efficient in some problems. It remains to be seen if this sampling method makes the LD treatment more statistically efficient than the SDD trial space. However, testing the sampling methodology would be useful for extensions to higher dimensions which will require a similar treatment.

REFERENCES

- [1] Jeffrey Willert and H. Park. Residual Monte Carlo high-order solver for moment-based accelerated thermal radiative transfer equations. *Journal of Computational Physics*, 276:405–421, 2014.
- [2] S.R. Bolding, M. Cleveland, and J.E. Morel. A high-order low-order algorithm with exponentially-convergent Monte Carlo for thermal radiative transfer. *Nuclear Science & Engineering: M&C 2015 Special Issue*, Jan. 2017.
- [3] Allan B. Wollaber, H. Park, R.B. Lowrie, R.M. Rauenzahn, and M.E. Cleveland. Radiation hydrodynamics with a high-order, low-order method. In *ANS Topical Meeting, International Topical Meeting on Mathematics and Computation*, Nashville Tennessee, 2015.
- [4] J. Willert, C.T. Kelly, D.A. Knoll, and H. Park. A hybrid approach to the neutron transport k-eigenvalue problem using NDA-based algorithms. M&C. Sun Valley, ID, 2013.
- [5] H. Park, J.D. Densmore, A.B. Wollaber, D.A. Knoll, and R.M. Ramenzahn. Monte Carlo solution methods in a moment-based scale-bridging algorithm for thermal radiative transfer problems. M&C. Sun Valley, ID, 2013.
- [6] S.R. Bolding and J.E. Morel. A high-order low-order algorithm with exponentially-convergent Monte Carlo for k -eigenvalue problems. ANS Winter Meeting. Anaheim, CA, 2014.
- [7] J. A. Fleck, Jr. and J. D. Cummings, Jr. An implicit Monte Carlo scheme for calculating time and frequency dependent nonlinear radiation transport. *J. Comput. Phys.*, 8(3):313–342, December 1971.

- [8] Dimitri Mihalas and Barbara Weibel-Mihalas. *Foundations of radiation hydrodynamics*. Courier Corporation, 1999.
- [9] James M Stone and Michael L Norman. ZEUS-2D: A radiation magnetohydrodynamics code for astrophysical flows in two space dimensions. I-The hydrodynamic algorithms and tests. *The Astrophysical Journal Supplement Series*, 80:753–790, 1992.
- [10] Samet Y Kadioglu, Dana A Knoll, Robert B Lowrie, and Rick M Rauenzahn. A second order self-consistent IMEX method for radiation hydrodynamics. *Journal of Computational Physics*, 229(22):8313–8332, 2010.
- [11] Elmer Eugene Lewis and Warren F Miller. *Computational methods of neutron transport*. John Wiley and Sons, Inc., New York, NY, 1984.
- [12] Allan B Wollaber. *Advanced Monte Carlo methods for thermal radiation transport*. PhD thesis, The University of Michigan, 2008.
- [13] E.F. Toro. *Riemann Solvers and Numerical Methods for Fluid Dynamics: A Practical Introduction*. Springer, 1999.
- [14] J.E. Morel, T.A. Wareing, and K. Smith. Linear-discontinuous spatial differencing scheme for S_n radiative transfer calculations. *Journal of Computational Physics*, 128:445–462, 1996.
- [15] E.W. Larsen, G.C. Pomraning, and V.C. Badham. Asymptotic analysis of radiative transfer problems. *Journal of Quantitative Spectroscopy and Radiative Transfer*, 29(4):285–310, 1983.
- [16] J.K. Shultis and W.L. Dunn. *Exploring Monte Carlo Methods*. Academic Press, Burlington, MA 01803, 2012.

- [17] X-3 Monte Carlo Team. MCNP - a general n-particle transport code, version 6: Volume I, overview and theory. LA-UR-03-1987, 2005.
- [18] Allan B Wollaber. Four decades of implicit Monte Carlo. *Journal of Computational and Theoretical Transport*, 45(1-2):1–70, 2016.
- [19] N.A. Gentile. Implicit Monte Carlo diffusion: An acceleration method for Monte Carlo time-dependent radiative transfer simulations. *Journal of Computational Physics*, 172(2):543–571, 2001.
- [20] Jeffery D Densmore, Kelly G Thompson, and Todd J Urbatsch. A hybrid transport-diffusion Monte Carlo method for frequency-dependent radiative-transfer simulations. *Journal of Computational Physics*, 231(20):6924–6934, 2012.
- [21] Allan B Wollaber, Edward W Larsen, and Jeffery D Densmore. A discrete maximum principle for the implicit Monte Carlo equations. *Nuclear Science and Engineering*, 173(3):259–275, 2013.
- [22] Edward W. Larsen, Akansha Kumar, and Jim E. Morel. Properties of the implicitly time-differenced equations of thermal radiation transport. *J. Comput. Phys.*, 238:82–96, April 2013.
- [23] N. A. Gentile and Ben C. Yee. Iterative implicit Monte Carlo. *Journal of Computational and Theoretical Transport*, 45(1):71–98, 2015.
- [24] Michael Scott McKinley, Eugene D Brooks III, and Abraham Szoke. Comparison of implicit and symbolic implicit Monte Carlo line transport with frequency weight vector extension. *Journal of Computational Physics*, 189(1):330–349, 2003.

- [25] Jeffery D. Densmore. Asymptotic analysis of the spatial discretization of radiation absorption and re-emission in implicit Monte Carlo. *Journal of Computational Physics*, 230(4):1116–1133, 2011.
- [26] Ryan T Wollaeger, Allan B Wollaber, Todd J Urbatsch, and Jeffery D Densmore. Implicit Monte Carlo with a linear discontinuous finite element material solution and piecewise non-constant opacity. *Journal of Computational and Theoretical Transport*, 45(2):71–98, 2016.
- [27] E.R. Wolters. *Hybrid Monte Carlo - Deterministic Neutron Transport Methods Using Nonlinear Functionals*. PhD thesis, Michigan, 2011.
- [28] J.R. Peterson. Exponentially convergent Monte Carlo for the 1-D transport equation. Master’s thesis, Texas A&M, 2014.
- [29] Eugene D. Brooks III, Michael Scott McKinley, Frank Daffin, and Abraham Szke. Symbolic implicit Monte Carlo radiation transport in the difference formulation: a piecewise constant discretization. *Journal of Computational Physics*, 205(2):737–754, 2005.
- [30] Eugene D. Brooks III, Abraham Szke, and Jayson D.L. Peterson. Piecewise linear discretization of symbolic implicit Monte Carlo radiation transport in the difference formulation. *Journal of Computational Physics*, 220(1):471–497, 2006.
- [31] Subrahmanyam Chandrasekhar. *Radiative Transfer*. Courier Corporation, 2013.
- [32] Paul Nelson Edward W. Larsen. Finite-difference approximations and super-convergence for the discrete-ordinate equations in slab geometry. *SIAM Journal on Numerical Analysis*, 19(2):334–348, 1982.
- [33] Thomas JR Hughes. *The finite element method: linear static and dynamic finite element analysis*. Courier Corporation, 2012.

- [34] Jim Morel. Neutron transport theory. Class Lecture Notes. Unpublished, 2014.
- [35] Jim Michael Ferguson. *Asymptotic accuracy of the equilibrium diffusion approximation and semi-analytic solutions of radiating shocks*. PhD thesis, Texas A&M University, 2014.
- [36] CT Kelley. Iterative methods for linear and nonlinear equations. *SIAM*, 65002, 1995.
- [37] Clell J Solomon. *Discrete-ordinates cost optimization of weight-dependent variance reduction techniques for Monte Carlo neutral particle transport*. PhD thesis, Kansas State University, 2010.
- [38] Rong Kong and Jerome Spanier. A new proof of geometric convergence for general transport problems based on sequential correlated sampling methods. *Journal of Computational Physics*, 227:9762–9777, 2008.
- [39] Jeffrey A Favorite, Ashley D Thomas, and Thomas E Booth. On the accuracy of a common Monte Carlo surface flux grazing approximation. *Nuclear Science and Engineering*, 168(2):115–127, 2011.
- [40] T.J. Urbatsch and T.M. Evans. Milagro version 2: An implicit Monte Carlo code for thermal radiative transfer: Capabilities, development, and usage. Los Alamos National Laboratory Report LA-14195-MS, 2006.
- [41] T.A. Wareing, E.W. Larsen, and M.L. Adams. Asymptotic diffusion accelerated discontinuous finite element schemes for the S_n equations in slab and X-Y geometries. In *International Topical Meeting on Advances in Mathematics, Computations, Reactor Physics*, volume 3, Pittsburgh, PA, 1991.
- [42] T.A. Wareing. *Asymptotic diffusion accelerated discontinuous finite element methods for transport problems*. PhD thesis, Michigan, 1991.

- [43] Edward W. Larsen and Jim E. Morel. Advances in discrete-ordinates methodology. *Nuclear Computational Science. Springer Netherlands*, pages 1–84, 2010.
- [44] Ryan McClarren. Numerical methods in reactor analysis. Class Lecture Notes, 2015.
- [45] Marvin Adams and William Martin. Diffusion synthetic acceleration of discontinuous finite element transport iterations. *Nuclear Science and Engineering*, 111(2):145–167, 1992.
- [46] Yousef Saad. *Iterative methods for sparse linear systems*. Siam, 2003.
- [47] C.Y. Lau and M.L. Adams. Discrete ordinates quadratures based on linear and quadratic discontinuous finite elements over spherical quadrilaterals. *Nuclear Science & Engineering: M&C 2015 Special Issue*, Jan. 2017.
- [48] Milton Abramowitz and Irene A Stegun. *Handbook of mathematical functions: with formulas, graphs, and mathematical tables*, volume 55. Courier Corporation, 1964.
- [49] Weston M. Stacey. *Nuclear Reactor Physics*. Wiley, 2007.

APPENDIX A

DERIVATIONS AND RELATIONS FOR THE LO SYSTEM

A.1 Useful Moment Relations for LO Equations

It is useful for derivation and solution of the LO equations to define several relations between various spatial moments. The following relations are derived for $\phi(x)$, but they can be applied to the moments of general functions. The cell-averaged $\phi(x)$ can be eliminated in terms of the L and R moments using the definition $b_{L,i}(x) + b_{R,i}(x) = 1$ as follows:

$$\phi_i = \frac{1}{h_i} \int_{x_{i-1/2}}^{x_{i+1/2}} \phi(x) dx \quad (\text{A.1})$$

$$= \frac{1}{h_i} \left(\int_{x_{i-1/2}}^{x_{i+1/2}} b_{L,i}(x) \phi(x) dx + \int_{x_{i-1/2}}^{x_{i+1/2}} b_{R,i}(x) \phi(x) dx \right) \quad (\text{A.2})$$

$$= \frac{1}{2} (\langle \phi \rangle_{L,i} + \langle \phi \rangle_{R,i}). \quad (\text{A.3})$$

A similar relation between the first moment and the L and R moments is

$$\phi_{x,i} = \frac{3}{2} (\langle \phi \rangle_{R,i} - \langle \phi \rangle_{L,i}). \quad (\text{A.4})$$

The above relations can be inverted to derived a relation for the L and R moments in terms of the slope and average moments. These moment expressions are defined purely in terms of integrals, and are independent of the chosen spatial representation.

Once a linear relation on the interior has been assumed, there are useful spatial closures that can be derived. The standard linear interpolatory expansion, for the

positive half-range, is restated here:

$$\phi^+(x) = \phi_{L,i}^+ b_{L,i}(x) + \phi_{R,i}^+ b_{R,i}(x), \quad x_{i-1/2} < x \leq x_{i+1/2}. \quad (\text{A.5})$$

This representation is substituted into the FE basis moment definitions given by Eq. (3.3) and Eq. (3.4) and the integrals evaluated. The resulting expressions produce a relation between the edge values and the outflow from a cell, i.e.,

$$\phi_{i,R}^+ = 2\langle\phi\rangle_{R,i}^+ - \langle\phi\rangle_{L,i}^+ \quad (\text{A.6})$$

and

$$\phi_{i,L}^+ = 2\langle\phi\rangle_{L,i}^+ - \langle\phi\rangle_{R,i}^+. \quad (\text{A.7})$$

As in the standard LDFE discretization with upwinding (for $\mu > 0$) we make the approximations $\phi_{i+1/2}^+ = \phi_{i,R}^+$ and $\phi_{i-1/2}^+ = \phi_{i-1,R}^+$. Substitution of the above expressions into the LO equations produce equations exclusively in terms of moment unknowns. The solution to these equations produces a linear representation over each cell that is equivalent to those of a standard LDFE Galerkin discretization [33].

To eliminate the LO unknowns in a manner that produces the same moments as a lumped LDFE Galerkin discretization, the following expression can be used for the outflow from a cell

$$\phi_{i+1/2}^+ = \phi_i^+ + \frac{\phi_{x,i}^+}{3}, \quad (\text{A.8})$$

which in terms of the FE moments is equivalent to $\phi_{i+1/2}^+ = \langle\phi\rangle_{R,i}^+$. Inserting this expression into the radiation moment equations, with the same definition for the linear representation over the interior of $\phi_{i+1/2}^+(x) = \phi_{L,i} b_{L,i}(x) + \phi_{R,i} b_{R,i}(x)$, will produce an equivalent set of unknowns as a linear discontinuous method with matrix

lumping for the radiation terms. The temperature equation and emission source must be independently lumped with an analogous definition of the edge values to Eq. (A.8). This relation preserves the average within a cell but does not correctly reproduce the first moment.

A.2 Hybrid Picard-Newton Method for the LO Equations

This section briefly derives the equations for the Picard-Newton method solution to the nonlinear LO equations, with the LDFF representation of the temperatures, based on the approach in [14]. The Picard iterations are necessary because material properties are lagged within each Newton Steps, neglecting that portion of the Jacobian. Because we have only considered problems with constant densities and heat capacities, the linearization described below is in terms of temperature T rather than material internal energy, for simplicity. However, the linearization can be formed in terms of internal energy to apply this method to a general equation of state.

To formulate the linear equations for each Newton step, the Planckian source is linearized in the material and radiation equations (Eq. (2.2) & Eq. (2.1)). Application of the first order Taylor expansion in time to the implicit emission source $\sigma_a ac(T^{n+1})^4$, about some temperature T^* at some time $t^* \in [t^n, t^{n+1}]$, yields

$$\sigma_a^{n+1} ac T^{4,n+1} \simeq \sigma_a^* ac [T^{*4} + (T^{n+1} - T^*) 4T^{*3}], \quad (\text{A.9})$$

where $\sigma_a^* \equiv \sigma_a(T^*)$. Substitution of this expression into Eq. (2.2) yields

$$\rho c_v \left(\frac{T^{n+1} - T^n}{\Delta t} \right) = \sigma_a^* \phi^{n+1} - \sigma_a^* ac [T^{*4} + (T^{n+1} - T^*) 4T^{*3}]. \quad (\text{A.10})$$

Algebraic manipulation of this equation yields an expression for $T^{n+1} - T^*$:

$$(T^{n+1} - T^*) = \frac{\frac{\sigma_a^* \Delta t}{\rho c_v} [\phi^{n+1} - acT^{*4}] + (T^n - T^*)}{1 + \sigma_a^* ac \Delta t \frac{4T^{*3}}{\rho c_v}}.$$

This expression is substituted back into Eq. (A.9) to form an explicit approximation for the emission source at t^{n+1} as

$$\sigma_a ac T^{4,n+1} \simeq \sigma_a^* (1 - f^*) \phi^{n+1} + f^* \sigma_a^* ac T^{4,n} + \rho c_v \frac{1 - f^*}{\Delta t} (T^n - T^*) \quad (\text{A.11})$$

where $f^* = [1 + \sigma_a^* c \Delta t 4a T^{*3} / (\rho c_v)]^{-1}$ is often referred to as the Fleck factor [7].

Next, the above equation is spatially discretized. Application of the L spatial moment yields

$$\begin{aligned} \langle \sigma_a^* ac T^{4,n+1} \rangle_{L,i} &= \sigma_{ai}^* (1 - f_i^*) \langle \phi^{n+1} \rangle_{L,i} + f_i^* \sigma_{ai}^* ac \left(\frac{2}{3} T_{L,i}^{4,n} + \frac{1}{3} T_{R,i}^{4,n} \right) \\ &\quad \rho_i c_{vi} \frac{1 - f_i^*}{\Delta t} \left[\frac{2}{3} (T_{L,i}^n - T_{L,i}^*) + \frac{1}{3} (T_{R,i}^n - T_{R,i}^*) \right], \quad (\text{A.12}) \end{aligned}$$

where $T^{4,n}$ and T^n have been assumed LD and f^* is assumed constant over a cell, i.e., $f_i^* \equiv f(T_i^*)$. The error introduced by a constant f^* approaches zero as the non-linearity is converged because T^* approaches T^{n+1} . Based on an estimate for T^* , Eq. (A.12) is an expression for the Planckian emission source in the radiation moment equations with an additional effective scattering source. A similar expression can be derived for $\langle \sigma_{a,i} ac T^4 \rangle_R$ and the right moment equations. The expressions for the emission source is substituted into the discrete radiation moment equations, (Eq. (3.18)–(3.21)) to produce a linear system of equations for the new radiation intensity moments (upon closure of the moment equations).

Once the linear equations have been solved for new radiation moments, new temperature unknowns can be estimated. To conserve energy, the same linearization and discretizations used to solve the radiation equation must be used in the material energy equation. Substitution of Eq. (A.12) into the material energy L moment equation, i.e., Eq. (3.22), ultimately yields

$$\begin{aligned} \frac{2}{3}T_{L,i}^{n+1} + \frac{1}{3}T_{R,i}^{n+1} = \frac{f_i^* \sigma_{ai}^* \Delta t}{\rho c_v} \left[\langle \phi^{n+1} \rangle_{L,i} - ac \left(\frac{2}{3}T_{L,i}^{4,n} + \frac{1}{3}T_{R,i}^{4,n} \right) \right] + \\ (1 - f_i^*) \left(\frac{2}{3}T_{L,i}^* + \frac{1}{3}T_{R,i}^* \right) + f \left(\frac{2}{3}T_{L,i}^n + \frac{1}{3}T_{R,i}^n \right) \quad (\text{A.13}) \end{aligned}$$

A similar expression is produced for the R moment equation. This produces a local matrix equation to solve for new $T_{L,i}$ and $T_{R,i}$ unknowns.

Based on these equations, iterations on the value of the T^* and FE unknowns for ϕ^{n+1} and T^{n+1} can be performed to converge the nonlinearities of the system. The algorithm for solving the LO equations, with iteration index m , is defined as

1. Initialize $T^{*,m}$ unknowns using T^n or the last estimate of T^{n+1} from previous LO solve.
2. Build the LO system based on the effective scattering $(1 - f^{*,l})$ and emission terms evaluated using $T^{*,m}$.
3. Solve the linearized LO system to produce a new estimate $\phi^{n+1,m+1}$.
4. Estimate a new $T^{n+1,m+1}$ with energy update equation, e.g., Eq. (A.13).
5. $T^{*,m+1} \leftarrow T^{n+1,m}$ and $\phi^{n+1,m} \leftarrow \phi^{n+1,m+1}$.
6. Repeat 2-5 until $(T^{n+1,m})^4$ and $\phi^{n+1,m}$ are converged.

Convergence is based on the relative L_2 spatial norm of the change in $\phi^{n+1,m}$ and the emission source $\sigma_{ac}(T^{n+1,m})^4$.

A.2.1 Damped Newton Iterations

The algorithm in the previous section can be modified to improve the stability of convergence by including a fixed damping factor ξ . In this work, the Newton's method is formulated to directly estimate the final solution each step, rather than in terms of the change in the solution between steps. Thus, an intermediate solve based on the algorithm in the previous section is performed, followed by a damped update of the unknowns. The damped Newton's method algorithm is as follows:

1. Choose a damping factor $\xi \in (0, 1)$.
2. Initialize $T^{*,m}$ unknowns using T^n or the last estimate of T^{n+1} from previous LO solve.
3. Build the LO system based on the effective scattering $(1 - f^{*,m})$ and emission terms evaluated using $T^{*,m}$.
4. Solve the linearized LO system to produce an estimate $\phi^{n+1,m+1/2}$.
5. Evaluate a new estimate of $T^{n+1,m+1/2}$ with energy update equations, e.g., Eq. (A.13).
6. Compute new temperatures and intensities as

$$\begin{aligned}\phi^{n+1,m+1} &= \phi^{n+1,m} + \xi (\phi^{n+1,m+1/2} - \phi^{n+1,m}) \\ T^{n+1,m+1} &= T^{n+1,m} + \xi (T^{n+1,m+1/2} - T^{n+1,m}).\end{aligned}$$

7. $T^{*,m+1} \leftarrow T^{n+1,m}$ and $\phi^{n+1,m} \leftarrow \phi^{n+1,m+1}$.

8. Repeat 2-5 until $(T^{n+1,m})^4$ and $\phi^{n+1,m}$ are converged.

APPENDIX B

DERIVATIONS FOR HIGH-ORDER SOLVER

B.1 Analytic Error Contribution for LDD Trial Space

In this section, the treatment of the outflow discontinuity residual source and error tallying is detailed. Define the additional error contribution from the face sources at $x_{i+1/2}$ as $\delta\epsilon^{(m)}$. We have chosen to tally the contribution from these sources with MC everywhere except for at $x_{i+1/2}$. Thus, we need to solve for $\delta\epsilon^{(m)}$ at each face $x_{i+1/2}$ and add that contribution to the tallies $\epsilon(x_{i+1/2}, \mu)$, which include the contribution from all other sources. The transport equation satisfied by $\delta\epsilon^{(m)}$, for positive μ and effective total cross section $\hat{\sigma}_t$, is

$$\mu \frac{\partial \delta\epsilon^{(m)}}{\partial x} + \hat{\sigma}_t \delta\epsilon^{(m)} = r_{\text{face}}(x_{i+1/2}^-) \delta^-(x - x_{i+1/2}) + r_{\text{face}}(x_{i+1/2}^+) \delta^+(x - x_{i+1/2}) \quad (\text{B.1})$$

This equation is integrated from $x_{i+1/2} - \alpha$ to $x_{i+1/2}$ to produce

$$\begin{aligned} \mu \delta\epsilon^{(m)}(x_{i+1/2}, \mu) - \mu \delta\epsilon^{(m)}(x_{i+1/2} - \alpha, \mu) + \int_{x_{i+1/2} - \alpha}^0 \hat{\sigma}_t \delta\epsilon^{(m)} dx \\ = r_{\text{face}}(x_{i+1/2}^-) + \int_{x_{i+1/2} - \alpha}^0 r_{\text{face}}(x_{i+1/2}^+) \delta^+(x - x_{i+1/2}) dx. \end{aligned} \quad (\text{B.2})$$

The integral on the right side of the equation is zero because $\delta^+(x - x_{i+1/2})$ is zero for $(-\infty, x_{i+1/2}]$. The limit of the above equation is taken as $\alpha \rightarrow 0$, i.e.,

$$\lim_{\alpha \rightarrow 0} \left(\mu \delta \epsilon^{(m)}(x_{i+1/2}, \mu) - \mu \delta \epsilon^{(m)}(x_{i+1/2} - \alpha, \mu) + \int_{x_{i+1/2} - \alpha}^0 \hat{\sigma}_t \delta \epsilon^{(m)} dx \right) = \lim_{\alpha \rightarrow 0} r_{\text{face}}(x_{i+1/2}^-) \quad (\text{B.3})$$

The integral goes to zero because $\delta \epsilon^{(m)}$ is smooth on the interior of the cell, and $\mu \delta \epsilon^{(m)}(x_{i+1/2} - \alpha, \mu)$ goes to zero because there is no source upstream of $x_{i+1/2}^-$. Thus, the final solution is

$$\delta \epsilon^{(m)}(x_{i+1/2}, \mu) = \frac{r_{\text{face}}(x_{i+1/2}^-)}{\mu} = \tilde{I}^{(m)}(x_{i+1/2}^-, \mu) - \tilde{I}^{(m)}(x_{i+1/2}, \mu). \quad (\text{B.4})$$

The update equation for $I(x_{i+1/2}, \mu)$ is thus

$$\tilde{I}^{(m+1)}(x_{i+1/2}, \mu) = \tilde{I}^{(m)}(x_{i+1/2}, \mu) + \epsilon^{(m)}(x_{i+1/2}, \mu) + \delta \epsilon^{(m)}(x_{i+1/2}, \mu) \quad (\text{B.5})$$

$$= \tilde{I}^{(m)}(x_{i+1/2}^-, \mu) + \epsilon^{(m)}(x_{i+1/2}, \mu). \quad (\text{B.6})$$

B.2 Analytic Answer for Fixed Source Problem

In this section we model a fixed-source, pure-absorber neutral particle transport calculation with a known analytic answer and spatial moments of the mean intensity that can be evaluated semi-analytically. For a general isotropic source $q(x)$, the 1D transport equation to be solved is

$$\mu \frac{\partial I}{\partial x} + \sigma_a I(x, \mu) = \frac{q(x)}{2} \quad (\text{B.7})$$

A problem is designed to imitate the two-material problem in Sec. 5.3 for the purpose of testing the fix-up for the HO solver in Chapter 7. Thus, the domain has two different constant cross sections and a small isotropic source throughout the domain.

The boundary conditions are $I(0, \mu) = I_{inc}$ for $\mu > 0$ and $I(X, \mu) = \frac{q(X)}{2\sigma_a}$ for $\mu < 0$, where $x = X$ is the right boundary. For positive directions, this first order differential equation is solved using an integration factor $\exp(\tau(x)/\mu)$ where $\tau(x) = \int_0^x \sigma_a(x') dx'$. The solution of Eq. (B.7) for the positive half-range intensity is

$$I(x, \mu) = I_{inc} e^{-\tau(x)/\mu} + \int_0^x \frac{q(x')}{2\mu} \exp\left(\frac{\tau(x') - \tau(x)}{\mu}\right) dx', \quad \mu > 0. \quad (\text{B.8})$$

Integration of this result over the positive half range of μ gives

$$\phi^+(x) = I_{inc} E_2[\tau(x)] + \frac{1}{2} \int_0^x q(x') E_1[\tau(x) - \tau(x')] dx', \quad (\text{B.9})$$

where the linearity of $\tau(x)$ has been used to simplify the argument of the E_1 function.

The internal volumetric source is now defined as $q(x) = q_0 \sigma_a(x)$, where q_0 is a constant. This definition simulates a floor equilibrium distribution and ensures that $\phi^-(x)$ is a constant throughout the domain. This source definition is substituted into Eq. (B.9) with the following general relation [48]

$$E_1(y) = -\frac{d E_2(y)}{dy} \quad (\text{B.10})$$

to yield a perfect derivative inside the integral. The resulting solution is

$$\phi^+(x) = I_{inc} E_2[\tau(x)] + \frac{q_0}{2} (1 - E_2[\tau(x)]). \quad (\text{B.11})$$

The solution for the negative half range is

$$\phi^-(x) = \frac{q(x)}{2\sigma_a} = \frac{q_0}{2} \quad (\text{B.12})$$

Combination of the above two equations gives the solution for the mean intensity:

$$\phi(x) = I_{inc} E_2 [\tau(x)] + \frac{q_0}{2} (2 - E_2 [\tau(x)]) . \quad (\text{B.13})$$

This expression can be integrated over any spatial cell, via high-precision quadrature, to accurately approximate moments of the mean intensity.

APPENDIX C

DERIVATION OF THE WLA-DSA EQUATIONS

In this section, we derive the discretized diffusion equation and LD mapping equations that are used in the WLA-DSA equations. To simplify notation, we derive the equations from a generic transport equation (rather than the error equations) with isotropic scattering and source q_0 , i.e.,

$$\mu \frac{\partial I}{\partial x} + \sigma_t I = \frac{\sigma_s}{2} (\phi(x) + q_0). \quad (\text{C.1})$$

C.1 Forming a Continuous Diffusion Equation

First, a continuous spatial discretization of a diffusion equation is derived. The mean intensity ϕ will ultimately be assumed continuous at faces to produce a standard three-point finite-difference diffusion discretization. The zeroth and first μ moment of Eq. (C.1) produce the P_1 equations [11, 42], i.e.,

$$\frac{\partial J}{\partial x} + \sigma_a \phi = q_0 \quad (\text{C.2})$$

$$\sigma_t J + \frac{1}{3} \frac{\partial \phi}{\partial x} = 0. \quad (\text{C.3})$$

The spatial finite element moments (defined by Eq. (3.3) and (3.4)) are taken of the above equations. The mean intensity is assumed linear on the interior of the cell, i.e., $\phi(x) = \phi_L b_L(x) + \phi_R b_R(x)$, for $x \in (x_{i-1/2}, x_{i+1/2})$. Taking the left moment, evaluating integrals, and rearranging yields

$$J_i - J_{i-1/2} + \frac{\sigma_{a,i} h_i}{2} \left(\frac{2}{3} \phi_{L,i} + \frac{1}{3} \phi_{R,i} \right) = \frac{h_i}{2} \langle q \rangle_{L,i}, \quad (\text{C.4})$$

where J_i is the average of the flux J over the cell. The moments of q are not simplified to be compatible with the error equations which are in terms of moments. For the R moment

$$J_{i+1/2} - J_i + \frac{\sigma_{a,i} h_i}{2} \left(\frac{1}{3} \phi_{L,i} + \frac{2}{3} \phi_{R,i} \right) = \frac{h_i}{2} \langle q \rangle_{R,i} . \quad (\text{C.5})$$

The equation for the L moment is evaluated for cell $i+1$ and added to the R moment equation evaluated at i . The flux J is assumed continuous at $i+1/2$ to eliminate the face fluxes from the equations. The sum of the two equations becomes

$$J_{i+1} - J_i + \frac{\sigma_{a,i+1} h_{i+1}}{2} \left(\frac{2}{3} \phi_{L,i+1} + \frac{1}{3} \phi_{R,i+1} \right) + \frac{\sigma_{a,i} h_i}{2} \left(\frac{1}{3} \phi_{L,i} + \frac{2}{3} \phi_{R,i} \right) = \frac{h}{2} (\langle q \rangle_{L,i+1} + \langle q \rangle_{R,i}) . \quad (\text{C.6})$$

The mean intensity is approximated as continuous at each face, i.e., $\phi_{L,i+1} = \phi_{R,i} \equiv \phi_{i+1/2}$. Adding the L and R moments of Eq. (C.3) together, with the continuous approximation for $\phi_{i+1/2}$, produces a discrete Fick's law equation [49]

$$J_i = -D_i \frac{\phi_{i+1/2} - \phi_{i-1/2}}{h_i}, \quad (\text{C.7})$$

where $D_i = 1/(3\sigma_{t,i})$. Substitution of Eq. (C.7) into Eq. (C.6) and rearranging yields the following discrete diffusion equation:

$$\begin{aligned} \left(\frac{\sigma_{a,i+1} h_{i+1}}{6} - \frac{D_{i+1}}{h_{i+1}} \right) \phi_{i+3/2} + \left(\frac{D_{i+1}}{h_{i+1}} + \frac{D_i}{h_i} + \frac{\sigma_{a,i+1} h_{i+1}}{3} + \frac{\sigma_{a,i} h_i}{3} \right) \phi_{i+1/2} \\ + \left(\frac{\sigma_{a,i} h_i}{6} - \frac{D_i}{h_i} \right) \phi_{i-1/2} = \frac{h_{i+1}}{2} \langle q \rangle_{L,i+1} + \frac{h_i}{2} \langle q \rangle_{R,i} . \end{aligned} \quad (\text{C.8})$$

To allow for the use of lumped or standard LD in these equations, we introduce the factor θ , with $\theta = 1/3$ for standard LD, and $\theta = 1$ for lumped LD. The diffusion

equation becomes

$$\begin{aligned} & \left(\frac{\sigma_{a,i+1}h_{i+1}}{4} (1 - \theta) - \frac{D_{i+1}}{h_{i+1}} \right) \phi_{i+3/2} + \left(\frac{D_{i+1}}{h_{i+1}} + \frac{D_i}{h_i} + \left(\frac{1 + \theta}{2} \right) \left[\frac{\sigma_{a,i+1}h_{i+1}}{2} + \frac{\sigma_{a,i}h_i}{2} \right] \right) \phi_{i+1/2} \\ & + \left(\frac{\sigma_{a,i}h_i}{4} (1 - \theta) - \frac{D_i}{h_i} \right) \phi_{i-1/2} = \frac{h_{i+1}}{2} \langle q \rangle_{L,i+1} + \frac{h_i}{2} \langle q \rangle_{R,i} . \quad (\text{C.9}) \end{aligned}$$

Summation over all cells forms a system of equations for ϕ at each face.

C.1.1 Diffusion Boundary Conditions

The upwinding in the LO system exactly satisfies the inflow boundary conditions, therefore a vacuum boundary condition is applied to the diffusion error equations. The equation for the left moment at the first cell is given by

$$J_1 - J_{1/2} + \frac{\sigma_{a,i}h_i}{2} \left(\frac{1 + \theta}{2} \phi_{L,i} + \frac{1 - \theta}{2} \phi_{R,i} \right) = \frac{h_i}{2} \langle q \rangle_{L,i} , \quad (\text{C.10})$$

The Marshak boundary condition for the vacuum inflow at face $x_{1/2}$ is given as

$$J_{1/2}^+ = 0 = \frac{\phi_{1/2}}{4} + \frac{J_{1/2}}{2}, \quad (\text{C.11})$$

which can be solved for $J_{1/2}$. Substitution of the above equation and Eq. (C.7) into Eq. (C.10) gives

$$\left(\frac{1}{2} + \sigma_{a,1}h_1 \frac{1 + \theta}{4} - \frac{D_1}{h_1} \right) \phi_{1/2} + \left(\sigma_{a,1}h_1 \frac{1 - \theta}{4} - \frac{D_1}{h_1} \right) \phi_{3/2} = \frac{h_1}{2} \langle q \rangle_{L,1} \quad (\text{C.12})$$

A similar expression can be derived for the right-most cell.

C.2 Mapping Solution onto LD Unknowns

Solution of the continuous diffusion equation will provide an approximation to ϕ on faces, denoted as $\phi_{i+1/2}^C$. We now need to map the face solution onto the LD

representation of ϕ . To do this, first we take the L and R finite element moments of the P_1 equations. A LDFE dependence is assumed on the interior of the cell for J and ϕ . Taking moments of Eq. (C.2) and simplifying yields

$$J_{i+1/2} - \frac{J_{L,i} + J_{R,i}}{2} + \frac{\sigma_{a,i} h_i}{2} \left(\frac{1}{3} \phi_{L,i} + \frac{2}{3} \phi_{R,i} \right) = \frac{h_i}{2} \langle q \rangle_{R,i} \quad (\text{C.13})$$

$$\frac{J_{L,i} + J_{R,i}}{2} - J_{i-1/2} + \frac{\sigma_{a,i} h_i}{2} \left(\frac{2}{3} \phi_{L,i} + \frac{1}{3} \phi_{R,i} \right) = \frac{h_i}{2} \langle q \rangle_{L,i} \quad (\text{C.14})$$

The moment equations for Eq. (C.3) are

$$\frac{1}{3} \left(\phi_{i+1/2} - \frac{\phi_{i,L} + \phi_{i,R}}{2} \right) + \frac{\sigma_{t,i} h_i}{2} \left(\frac{1}{3} J_{L,i} + \frac{2}{3} J_{R,i} \right) = 0 \quad (\text{C.15})$$

$$\frac{1}{3} \left(\frac{\phi_{i,L} + \phi_{i,R}}{2} - \phi_{i-1/2} \right) + \frac{\sigma_{t,i} h_i}{2} \left(\frac{2}{3} J_{L,i} + \frac{1}{3} J_{R,i} \right) = 0 \quad (\text{C.16})$$

The face terms $J_{i\pm 1/2}$ and $\phi_{i\pm 1/2}$ need to be eliminated from the system. First, the scalar intensity is assumed to be the value provided by the continuous diffusion solution at each face, i.e., $\phi_{i\pm 1/2} = \phi_{i\pm 1/2}^C$. Then, the fluxes are decomposed into half-range values to decouple the equations between cells. At $x_{i+1/2}$, the flux is composed as $J_{i+1/2} = J_{i+1/2}^+ + J_{i+1/2}^-$, noting that in this notation the half-range fluxes are $J_{i+1/2}^\pm = \pm \int_0^{\pm 1} \mu I(x_{i+1/2}, \mu) d\mu$ ¹. We approximate the incoming fluxes, e.g., $J_{i+1/2}^-$, based on $\phi_{i+1/2}^C$ and a P_1 approximation. The P_1 approximation provides the following relation [42]

$$\phi = 2(J^+ - J^-). \quad (\text{C.17})$$

At $x_{i+1/2}$, the above expression is solved for the incoming current $J_{i+1/2}^-$. The total

¹Typically, the half-range fluxes are defined with integrals weighted with $|\mu|$, but this notation would not be consistent with our definition of the half-range consistency terms.

current becomes

$$J_{i+1/2} = J_{i+1/2}^+ - J_{i+1/2}^- = 2J_{i+1/2}^+ - \frac{\phi_{i+1/2}^C}{2}, \quad (\text{C.18})$$

In the positive direction, at the right face, the values of ϕ and J are based on the LD representation within the cell at that face, i.e., $\phi_{R,i}$ and $J_{R,i}$. The standard P_1 approximation for the half-range fluxes is used[49], i.e.,

$$J^\pm = \frac{\gamma\phi}{2} \pm \frac{J}{2}, \quad (\text{C.19})$$

where γ accounts for the difference between the LO parameters and the true P_1 approximation. Thus, for the right face and positive half-range,

$$J_{i+1/2}^+ = \frac{\gamma}{2}\phi_{i,R} + \frac{J_{i,R}}{2} \quad (\text{C.20})$$

A similar expression can be derived for $x_{i-1/2}$. The total fluxes at each face are thus

$$J_{i+1/2} = \gamma\phi_{i,R} + J_{i,R} - \frac{\phi_{i+1/2}^C}{2} \quad (\text{C.21})$$

$$J_{i-1/2} = \frac{\phi_{i-1/2}^C}{2} - \gamma\phi_{i,L} + J_{i,L} \quad (\text{C.22})$$

Substitution of these results back into the LD balance equations and introduction of the lumping notation yields the final equations

$$\left(\gamma\phi_{i,R} + J_{i,R} - \frac{\phi_{i+1/2}^C}{2} \right) - \frac{J_{L,i} + J_{R,i}}{2} + \frac{\sigma_{a,i}h_i}{2} \left(\frac{(1-\theta)}{2}\phi_{L,i} + \frac{(1+\theta)}{2}\phi_{R,i} \right) = \frac{h_i}{2}\langle q \rangle_{R,i} \quad (\text{C.23})$$

$$\frac{J_{L,i} + J_{R,i}}{2} - \left(\frac{\phi_{i-1/2}^C}{2} - \gamma \phi_{i,L} + J_{i,L} \right) + \frac{\sigma_{a,i} h_i}{2} \left(\frac{(1+\theta)}{2} \phi_{L,i} + \frac{(1-\theta)}{2} \phi_{R,i} \right) = \frac{h_i}{2} \langle q \rangle_{L,i} \quad (\text{C.24})$$

$$\frac{1}{3} \left(\phi_{i+1/2}^C - \frac{\phi_{i,L} + \phi_{i,R}}{2} \right) + \frac{\sigma_{t,i} h_i}{2} \left(\frac{(1-\theta)}{2} J_{L,i} + \frac{(1+\theta)}{2} J_{R,i} \right) = 0 \quad (\text{C.25})$$

$$\frac{1}{3} \left(\frac{\phi_{i,L} + \phi_{i,R}}{2} - \phi_{i-1/2}^C \right) + \frac{\sigma_{t,i} h_i}{2} \left(\frac{(1+\theta)}{2} J_{L,i} + \frac{(1-\theta)}{2} J_{R,i} \right) = 0. \quad (\text{C.26})$$

The above equations are completely local to each cell and fully defined, including cells on the boundary. For simplicity, we just take $\gamma = 1/2$ for all results. The system can be solved for the desired unknowns $\phi_{i,L}$, $\phi_{i,R}$, $J_{i,L}$, and $J_{i,R}$, which represent the mapping of $\phi_{i+1/2}^C$ onto the LD representation for $\phi^\pm(x)$.